Institut de Physique de l'Université de Neuchâtel (Suisse)

ARPES Investigations on in situ PLD grown $YBa_2Cu_3O_{7-\delta}$

Thèse

présentée à la Faculté des Sciences

de l'Université de Neuchâtel

pour l'obtention du grade de Docteur en Sciences par

Yasmine Sassa

soutenue le 22 Février 2011

en présence des co-directeurs de thèse

Dr. Luc Patthey, Paul Scherrer Institut

Prof. Joël Mesot, Paul Scherrer Institut, ETHZ and EPFL

Prof. Philipp Aebi, Université de Neuchâtel

et du rapporteur

Prof. Hans Beck, Université de Neuchâtel

Neuchâtel, le 22 Février 2011

Université de Neuchâtel

FACULTE DES SCIENCES
Secrétariat-Décanat de la faculté
Rue Emile-Argand 11
CH-2000 Neuchâtel

IMPRIMATUR POUR LA THESE

ARPES investigations on *in situ* PLD grown $YBa_2Cu_3O_{7-\delta}$

Yasmine SASSA

UNIVERSITE DE NEUCHATEL

FACULTE DES SCIENCES

La Faculté des sciences de l'Université de Neuchâtel,
sur le rapport des membres du jury

MM. P. Aebi (co-directeur de thèse,
Université de Neuchâtel et Université de Fribourg),
J. Mesot (co-directeur de thèse, PSI, ETHZ et EPFL),
L. Patthey (co-directeur de thèse, PSI),
et H. Beck (rapporteur, Université de Neuchâtel)

autorise l'impression de la présente thèse.

Neuchâtel, le 22 mars 2011

Le doyen :
P. Kropf

Téléphone : +41 32 718 21 00 E-mail : secretariat.sciences@unine.ch www.unine.ch/sciences

Keywords: High-temperature superconductors, $YBa_2Cu_3O_{7-\delta}$, ortho-II, pulsed laser deposition, angle-resolved photoelectron spectroscopy

Mots clé: Supraconducteurs à haute temperature critique, $YBa_2Cu_3O_{7-\delta}$, ortho-II, ablation laser pulsé, photoémission résolue en angle

Abstract

Since the discovery of high-temperature superconductivity in layered copper oxides, the $YBa_2Cu_3O_{7-\delta}$ compound has been the subject of many experimental and theoretical studies. Recently, the interest in this material was renewed when quantum oscillation experiments in high magnetic fields of underdoped ortho-II ordered $YBa_2Cu_3O_{6.5}$ revealed that the Fermi surface reconstructs into one or several pockets. One of the most powerful techniques to study the Fermiology and electronic properties of a material, is angle-resolved photoelectron spectroscopy (ARPES). This technique requires a flat and clean crystalline surface usually obtained after cleaving. However, $YBa_2Cu_3O_{7-\delta}$ does not have a natural cleavage plane and due to polarity, the cleaved surface tends to be strongly overdoped even though the bulk is underdoped. As a results, ARPES experiments on $YBa_2Cu_3O_{7-\delta}$ single crystals are considered delicate and details of the electronic properties have remained elusive.

This thesis work presents an ARPES study of $YBa_2Cu_3O_{7-\delta}$ films *in situ* grown by pulsed laser deposition (PLD). Through a careful control of the growth, the films present underdoped surfaces with ordered oxygen vacancies within the CuO chains resulting in a clear ortho-II band folding of the Fermi surface. This study demonstrates the importance of having not only the correct surface carrier concentration, but also a very well ordered clean surface in order to obtain photoemission data on this compound that is representative of the *bulk* electronic properties. Further, the elaboration of the $YBa_2Cu_3O_{7-\delta}$ film growth is described and a careful investigation of the superconducting gap symmetry as well as pseudogap state of the ortho-II surface is presented.

Résumé

Depuis la découverte des oxides de cuivres supraconducteurs à haute temperature critique, le composé $YBa_2Cu_3O_{7-\delta}$ a fait l'objet de nombreuses études aussi bien expérimentales que théoriques. Récemment, ce matériel a été reconsidéré lorsque les oscillations quantiques sous champ magnétique ont révélé, dans le regime sous-dopé de la phase ordonnée ortho-II $YBa_2Cu_3O_{6.5}$, que la surface de Fermi se reconstruit sous une ou plusieurs poches. Une des plus puissante techniques expérimentales pour étudier la Fermiologie ainsi que les propriétés électronique des matériaux est la photoémission résolue en angle (ARPES). Cette méthode nécessite une surface cristalline propre et plate normalement obtenue après clivage. Cependant, le composé $YBa_2Cu_3O_{7-\delta}$ ne possède pas de plan de clivage naturel et dûe à la polarité du matériel, la surface clivée devient surdopé même si le cristal est à l'origine sous-dopé. Par conséquent, les expériences de photoémission résolue en angle sur les mono-cristaux d'$YBa_2Cu_3O_{7-\delta}$ sont considérées difficiles et peu de détails sur leurs propriétés électroniques ont été accessibles.

Ce travail de thèse présente l'étude de couches minces d'$YBa_2Cu_3O_{7-\delta}$ élaborées *in situ* par ablation laser pulsé (PLD) pour des mesures de photoémission résolue en angle. Grâce à un contôle minutieux de la croissance, les films présentent une surface sous-dopé avec au sein des chaînes CuO, un ordre des oxygènes vacants résultant à un clair repliement de bandes à la surface de Fermi liée à l'ortho-II. Cette étude démontre l'importance d'avoir une surface avec la correcte concentration de porteurs mais aussi propre et ordonnée afin que les données de photoémission sur ce composé représentent les propriétés électroniques du cristal. De plus, l'élaboration des films d'$YBa_2Cu_3O_{7-\delta}$ est décrite et une observation méticuleuse de la symmétrie du gap supraconduteur ainsi que du pseudogap de la surface ortho-II y est présentée.

Preface

The content of this thesis is based on research carried out at the Surface/Interface spectroscopy (SIS) beamline of the Swiss Light Source (SLS), Paul Scherrer Institute (PSI). The main subject of this PhD thesis is based on the elaboration of $YBa_2Cu_3O_{7-\delta}$ (YBCO) films using a pulsed laser deposition (PLD) technique and the investigation of their electronic properties by angle-resolved photoelectron spectroscopy (ARPES). The present manuscript displays the results obtained and consists of six chapters. Chapter 1 is an introduction of the topic and explains the motivation of this work. Chapter 2 describes some general characteristics related to high-temperature superconductors (HTSC). Chapter 3 presents a description of the PLD technique and explains the procedure established for the growth of YBCO films. Chapter 4 is devoted to the ARPES technique and a selection of principal ARPES results on HTSC are summarized. Chapter 5 displays the main results of the thesis project and Chapter 6 the conclusions.

Parts of the thesis were also dedicated to investigate the electronic structure of Na_xCoO_2 (x = 0.80-0.85) single crystals. The crystal structure is composed of single Na sheets sandwiched in between CoO_2 layers, where the Co atoms form a *triangular* lattice. By increasing the Na content x, which represents the electron doping level in this system, different phases with exotic physical properties emerge, ranging from superconducting character by intercalation of water molecules to a charged ordered insulator, followed by Curie-Weiss metal. For higher doping ($0.8 < x < 1$) also a incommensurate spin density wave order is found. A considerable ARPES work has been published for $x \leq 0.8$, but very few in the incommensurate spin density wave region $x \geq 0.8$. The ARPES studies performed in this thesis have revealed that depending of the cooling rate, the opening of a gap at the Fermi level is observed. The origin of this gap could possibly be connected to a Na ordering, which influences the electronic properties but more investigations are needed. Although these results are extremely interesting, they were not included in this manuscript.

Finally, during the thesis, I have actively participated/collaborated to other ARPES studied performed on $La_{2-x}Sr_xCuO_4$, $YBa_2Cu_4O_8$ and $Bi_2Sr_2Ca_nCu_{n+1}O_{2n+6+x}$ single crystals. The results obtained on these compounds are partly summarized at the end of chapter 4 and beginning of chapter 5. All the articles resulting from these four years of PhD studies are referred in the publications list.

List of Abbreviations

Copper oxides Materials:
BiSCO: $Bi_2Sr_2Ca_nCu_{n+1}O_{2n+6+x}$
LSCO: $La_{2-x}Sr_xCuO_4$
Na-CCOC: $Ca_{2-x}Na_xCuO_2Cl_2$
NdCeCO: $Nd_{2-x}Ce_xCuO_4$
YBCO: $YBa_2Cu_3O_{7-\delta}$
Y1248: $YBa_2Cu_4O_8$

Experimental Techniques:
AFM: Atomic force microscopy
ARPES: Angle-resolved photoelectron spectroscopy
LEED: Low-energy electron diffraction
PES: Photoelectron spectroscopy
PLD: Pulsed laser deposition
PPMS: Physical properties measurement system
RHEED: Reflection high-energy electron diffraction
XRD: X-Ray diffraction

General:
AB: Antibonding band
AF: Antiferromagnetic
BB: Bonding band
BZ: Brillouin zone
CARVING: Complete Angle Resolved Variation for electron spectroscopy IN villiGen
EDC: Energy distribution curve
FS: Fermi surface
HTSC: High-temperature superconductors
LHB: Lower Hubbard band
MDC: Momentum distribution curve
NB: Non-bonding band
OD: Overdoped
OPT: Optimally doped
PSG: Pseudogap
SC: Superconductor
T_c: Critical temperature
T^*: Pseudogap temperature
UD: Underdoped
UHB: Upper Hubbard band
UHV: Ultra-high vacuum
ZRS: Zhang-Rice singlet
Δ: Energy gap

List of Tables

Contents

1 Introduction

Since more than twenty years, one of the most interesting challenges in solid state physics is to find a suitable theory to describe the mechanism of high-temperature superconductivity. These fascinating compounds exhibit a number of anomalous electronic properties in both superconducting and normal states that cannot be explained by conventional theories. Despite their unconventional behavior, which make the understanding of these systems extremely difficult, high-temperature superconductors are experimentally rather easy to measure. Indeed, these compounds are layered materials with quasi-two-dimensional electronic structure, which simplifies the analysis of the data and make experiments like angle-resolved photoelectron spectroscopy (ARPES) achievable.

ARPES is a powerful technique, which offers the possibility to study the electronic band structure of solids as function of temperature, doping and momentum. To achieve significant results, this technique requires a flat and clean crystalline surface, usually obtained after cleaving of the crystal. However, not all high-temperature superconductors display a natural cleavage plane. For instance, $YBa_2Cu_3O_{7-\delta}$ (YBCO) single crystals, which have been intensively studied by various bulk techniques, do not have a natural cleavage plane making surface-sensitive experiments delicate. As a result, very few significative ARPES investigations have been performed.

To overcome the cleaving procedure, the solution presented in this work is to grow high-quality epitaxial superconducting YBCO thin-films and to transfer them *in situ* to the ARPES set-up. To provide high-quality, *c*-axis oriented films, the pulsed laser deposition (PLD) technique was chosen. The stoichiometric ablation of constituent species from the target makes the PLD technique attractive, particularly for the synthesis of complex multi-component phases like HTSC. By growing films in a two-dimensional layer-by-layer mode, the technique offers the possibility to produce YBCO with control of surface termination (chain or plane), thickness, strain effects, (un-)twinning, and oxygen content.

In this thesis, an ARPES study of *in situ* grown YBCO films is presented. The top-most layer of the film displays an underdoped surface with an additional band

folding, which can be connected to the oxygen vacancies ordered Ortho-II phase.

Structure of this thesis:
In the *second* chapter, some general characteristics of high-temperature superconductivity are summarized. Crystal and electronic structure are described and a presentation of the generic phase diagram is made. Finally, some theoretical aspects are introduced.

The *third* chapter is focused on the PLD technique and consists of three sections. First, the PLD principle and the growth mechanism are explained. Second, the experimental set-up and techniques of films characterizations are described. Third, details on substrate and films preparations determined in this work for growing high-quality epitaxial YBCO thin-films are presented. The scope of this chapter is to show how the superconducting films were elaborated to obtain significative ARPES results.

The *fourth* chapter is an introduction to photoelectron spectroscopy. The chapter starts by describing the photoelectron process then, a presentation of the experimental set-up used in this thesis is made. To close the chapter, a brief overview of the main results obtained by ARPES on high-temperature superconductors is presented.

The *fifth* chapter is devoted to ARPES measurements performed on YBCO. The first section summarizes ARPES results obtained on YBCO single crystals and the second one is dedicated to YBCO thin-films made by PLD and transferred *in situ* to the ARPES set-up. A study of the superconducting and pseudogap phase of the Ortho-II phase is presented.

Finally, the *sixth* chapter summarizes the main results obtained in this work.

2 Strongly Correlated Materials

Strongly correlated systems encloses a wide variety of materials, which are characterized by strong interactions or correlations between electrons. Early in the modern solid state physics, in 1930's, Bloch [1] and Wilson [2] developed the band theory, which explained why some materials exhibit metallic behavior and others insulating properties. However, Bloch and Wilson theory could not clarify a large number of insulating $3d$ transition metal compounds, such as NiO and CoO, which were predicted to be metals [3]. Peierls and Mott explained this inconsistency by including electron-electron interactions [4, 5] and a few years later, Hubbard [6] established a simple model based on the tight-binding approximation. Using two terms in the Hamiltonian, he described particle interactions in a lattice : a kinetic term allowing hopping of particles between the sites of the lattices and a potential term consisting of an on-site interaction. Nowadays, the Hubbard model is frequently used to study strongly correlated systems and these insulators are know as Mott-Hubbard insulators. To strengthen the Hubbard model, Anderson introduced the concept of superexchange [7], which clarifies strong antiferromagnetic coupling between two next-nearest neighbor positive ions through a non-magnetic anion.

During all these years, unexpected new discoveries have been made and one of the challenge in condensed matter physics is to obtain a better understanding of correlated systems but also its manifestation in a large variety of phenomena such as metal insulator transitions, insulator-superconductor transitions, Kondo effects, frustrated materials, heavy Fermion system, high temperature superconductors, mixed valence systems, quantum Hall effect, colossal magneto-resistance, charge ordering, and so on. This thesis is focused on one particular class of material namely high-temperature superconductors (HTSC), or more specifically, cuprates. Since their discovery 20 years ago, these materials have aroused curiosity and fascination in the condensed matter physics community. In addition to the intriguing goal of finding a room-temperature superconductor, this lively research field comprise a number of fundamental and unresolved problems in condensed matter physics, *e.g.* metal insulator transition in low dimensions, breakdown of Fermi liquid theory, origin and behavior of unconventional superconductivity, quantum criticality, electronic inhomogeneities, and quantum antiferromagnetism in low dimensions. In the following subsection a general presentation of HTSC materials and a description of related theories is made.

2.1 Brief historical summary of superconductivity

Superconductivity was first discovered in mercury (Hg) at 4.2 K almost 100 years ago by H. Kamerlingh Onnes [8]. This finding raised curiosity and research towards new superconductors with a higher critical temperature T_c became of great interest. By 1980, many metals as well as intermetallic compounds and alloys had been found to be superconducting. Classical ferromagnets did not exhibit superconductivity except if the material was under high pressure such as iron (Fe) where a $T_c = 2$ K has been reported [9]. The study of superconductivity was a motivation for both experimental and theoretical physics in particular regarding the electronic mechanism for phonon-mediated superconductivity and the symmetry of the superconducting state. Some principal key properties and discoveries for these so-called Type I superconductors can be summarized as follows:

- The observation of vanishing resistivity at a critical temperature T_c [8];
- The diamagnetic behavior observed in 1933 by Meissner and Ochsenfeld [10];
- The London theory, which in 1935 described the Meissner effect as a consequence of the minimization of the electromagnetic free energy carried by a superconducting current;
- The Isotope effect for Hg observed by Maxwell [11] in 1950, which suggested that the electron-phonon coupling might be responsible for superconductivity;
- The Ginzburg-Landau theory in 1950, which extended the London theory and introduced the order parameter [12];
- The Bardeen, Cooper, Schrieffer (BCS) theory in 1957 [13], which gave a definite explanation of Type I superconductivity in terms of Copper pairs [14], i.e. pairs of electrons interacting through the exchange of phonons.

Until about 1980, the highest T_c observed, was in the Nb_3Ge compound with $T_c = 23.4$ K. However, in 1986, Bednorz and Müller [15] made the discovery of an entirely new class of solids with a higher value of $T_c = 35$ K. The new superconducting material was La_2CuO_4 in which some La^{3+} ions can be substituted with Ba^{2+}, Sr^{2+} or Ca^{2+}. This exchange of ions dopes the material and hole-carriers are created. Soon after this discovery, the substitution of the La^{3+} ions by the Y^{3+} gave the first HTSC compound, namely $YBa_2Cu_3O_{7-\delta}$ (YBCO) with a $T_c = 90$ K [16]. Further exploration for new cuprate superconductors with even higher T_c led to the discovery of, e.g. $Bi_2Sr_2Ca_2Cu_3O_{10}$ [17], $Tl_2Ba_2Ca_2Cu_3O_{10}$ [18] and $HgBa_2Ca_2Cu_3O_8$ [18, 19] compounds in subsequent years. At present, $T_c = 135$ K under ambient pressure and $T_c = 164$ K under 31 GPa observed in $HgBa_2Ca_2Cu_3O_8$ [20] are the highest values obtained so far.

A schematic view of the historical development of superconductivity (or T_c) is presented in Fig. 2.1(a-b). As also shown, during very recent years, a new class of iron-based superconductors has emerged [21]. However, this is beyond the scope of this thesis.

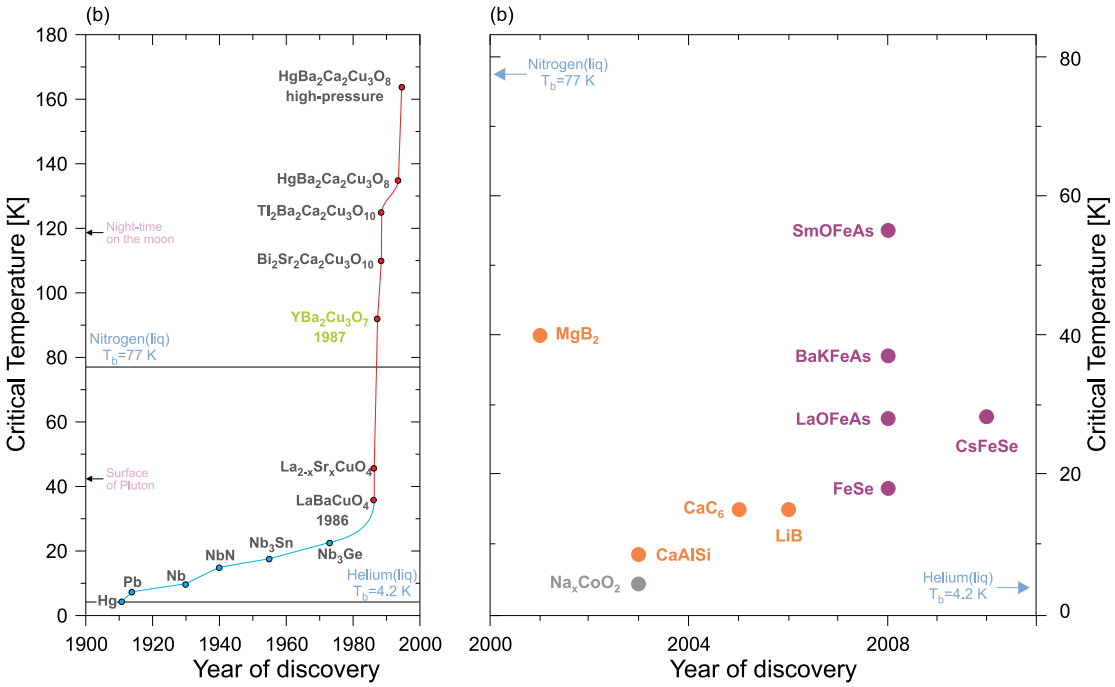

Figure 2.1: (a) Evolution of the superconducting transition temperature (T_c) from year 1900 to 2000 and (b) from 2000 to present.

2.2 Crystal structure

All cuprate superconductors have a quasi-two-dimensional (2D) layered structure in common, where one or more copper oxide (CuO_2) planes are contained. Their structure is based on an alternate stacking of CuO_2 planes separated by other oxide layers. These *intermediate* layers normally acts as charge reservoirs [22], which maintains both charge neutrality as well as cohesion of the structure. The interaction between CuO_2 planes and charge reservoirs plays an important role for the control and change of the carrier concentration. Indeed, substitution or insertion of oxygen in the layers separating the CuO_2 planes dopes the material by either electrons or holes. Figure 2.2(a) shows an illustration of the common structure of hole-doped cuprate HTSC. Three different structures of CuO_2 planes can be distinguished: the first one consists of the CuO_6 octahedrons as in $La_{2-x}Sr_xCuO_4$ (LSCO)[Fig. 2.2(b)], the second one is the CuO_5 pyramids as in $YBa_2Cu_3O_{7-\delta}$ (YBCO)[Fig. 2.2(c)] and the third one is the planar CuO_4 squares

as in $Nd_{2-x}Ce_xCuO_4$ (NdCeCO) [Fig. 2.2(d)].

The main material studied in this thesis is YBCO. When $\delta = 1$, the parent antifer-

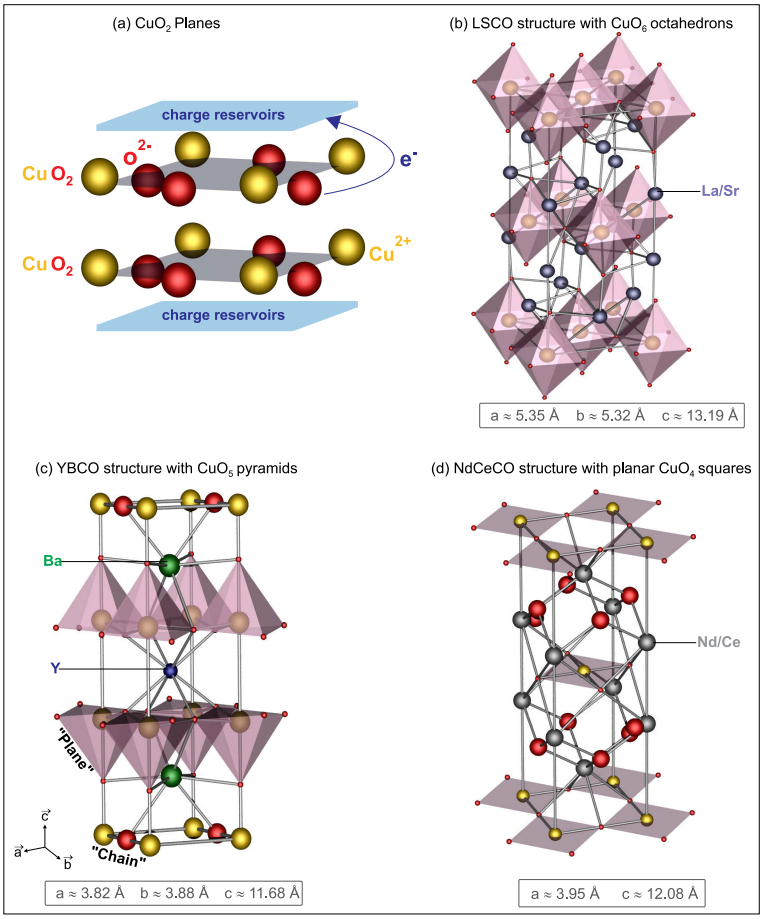

Figure 2.2: (a)Illustration of the common crystallographic structure of HTSC. CuO_2 planes are separated from each other by the so-called charge reservoir layers. Hole doping is symbolized by the transfer of electrons (e^-) from the CuO_2 planes to the charge reservoirs by the blue arrows. (b) Crystal structure of $La_{2-x}Sr_xCuO_4$ (LSCO) where the CuO_6 octahedrons are represented. (c) Structure of $YBa_2Cu_3O_{7-\delta}$ (YBCO) showing the CuO_5 pyramids and CuO chains. (d) Structure of $Nd_{2-x}Ce_xCuO_4$ (NdCeCO) with the planar CuO_4 squares.

romagnetic compound $YBa_2Cu_3O_6$ is a Mott-Hubbard insulator with a tetragonal crystal structure. By adding oxygen into the charge reservoirs i.e. decreasing δ, the CuO_2 planes are hole-doped, the compound becomes superconducting and the crystal structure is orthorhombic. The main difference between the parent compound and the superconducting YBCO is the existence of one dimensional CuO chains[1], which plays the role of charge reservoirs for the superconducting CuO_2

[1]By definition, the chains correspond to the association of Cu and O atoms forming 1D layers in YBCO.

planes. The crystal structure of superconducting orthorhombic YBCO is shown in Fig. 2.2(c). Starting from the center of the unit cell, there is a single Y atom. On each side are the CuO_2 planes arranged as shown in Fig. 2.2(c). Moving outwards is a plane of Ba and O atoms, then, terminating the cell, the CuO chains along the b-axis.
YBCO has a variable oxygen stoichiometry and accordingly, a variable T_c. The change in oxygen content occurs in the CuO chains, although the holes provided by the oxygen atoms are transferred to the CuO_2 planes [23]. Further, oxygen vacancies in the chains tend to order [24,25] giving rise to superstructures [26,27]. Figure 2.3(a) shows a CuO chain layer with a ratio of copper and oxygen atoms of 1:1. This ideal case would correspond to an oxygen content $n = 7$ (δ =0) with a maximum $T_c \approx 90$ K. Figure 2.3(b-d) illustrates some of the possible configu-

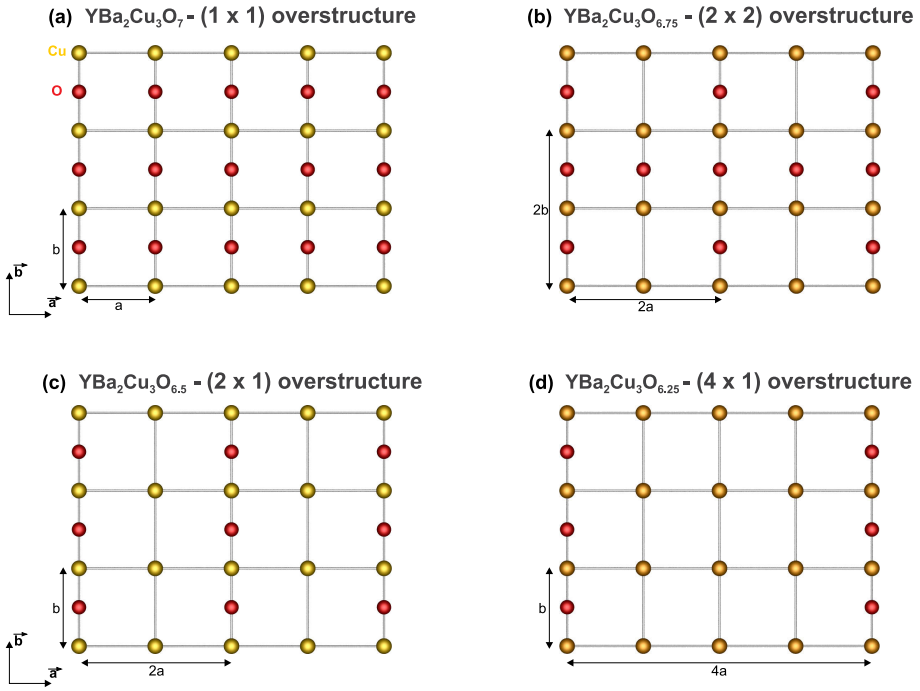

Figure 2.3: Model of oxygen ordering in the YBCO CuO chain layers. (a) Representation of the chains for the Ortho I structure corresponding to an oxygen content closed $n = 7$ with a maximal $T_c = 90$ K. All the chains are completely filled in contrast with the ortho-II phase (c) where one chain of two is filled. This corresponds to an oxygen content $n = 6.5$ with $T_c = 60$ K and a doubled unit cell ($2a$). (b,d) (2×2) and (4×1) overstructures corresponding to an oxygen content $n = 6.75$ and $n = 6.25$, respectively.

rations of oxygen vacancy ordering within the CuO chains. The superstructure shown in Fig. 2.3(b) gives rise to a (2×2) reconstruction with the absence of every second oxygen atom along the a and b direction, respectively. This corresponds to an oxygen content $n \approx 6.75$. Figure 2.3(c) represents the so-called ortho-II superstructure, which is characterized by a periodic alternation of filled and empty

CuO chains resulting in a unit cell doubling along the a-axis. The oxygen content is $n \approx 6.5$ and the $T_c \approx 60$ K. The ortho-II superstructure have gained a lot of interest since quantum oscillations experiments conducted on high quality ortho-II single crystals [28, 29] have revealed that the Fermi surface reconstructs into one [30–32] or several [33, 34] pockets. This exciting YBCO superstructure will be further developed in chapter 5. Finally, the (4×1) overstructure is shown in Fig. 2.3(d) with a model of three subsequently absent oxygen rows corresponding to an oxygen doping of $n \approx 6.25$. It is important to specify that changing the oxygen stoichiometry in YBCO does not induce a drastic change of T_c. In fact, for $n = 6.8$ or $n = 7$, T_c remains very close to its maximum value. Chain Cu atoms surrounded by two oxygen atoms have a valence of +1. The oxygen atom donates an electron to each Cu and thus, the valence of the Cu becomes +2. The transfer of electrons to the Cu atoms creates holes that are injected into the CuO_2 planes. As a result, it is possible to change the hole concentration without changing the oxygen stoichiometry, *e.g.* by annealing, which changes the degree of vacancy ordering.

2.3 Electronic structure

To understand the complexity of HTSC, one should consider the electronic structure of the undoped CuO_2 plane. Due to a splitting of the degenerate copper 3d (Cu-3d) levels in a crystal field of square-planar symmetry, the $3d_{x^2-y^2}$ orbital of Cu-3d and O-2p orbitals hybridize. Such hybridization gives rise to a (half filled) metallic antibonding (AB) band σ^*. Figure 2.4(a) illustrates the crystal field splitting of the Cu-3d level. The Cu^{2+} is surrounded by four oxygens in the CuO_2 plane and apical oxygen perpendicular to the plane, the crystal field splits the otherwise degenerate five d-orbitals where the four lower energy orbitals (xy, xz, yz, $3z^2 - y^2$) are fully occupied, while the orbital with the highest energy ($x^2 - y^2$) is half-filled. Since the energies of the Cu-3d and O-2p orbitals are close, there is a strong hybridization between them. As a result, the topmost energy level has both Cu-$3d_{x^2-y^2}$ and O-$2p_{x,y}$ character. The hybridization of the other Cu-3d levels is smaller. However, the localized nature of the Cu-3d orbitals makes the undoped system a Mott insulator [5, 35] meaning that the on-site Coulomb interaction U splits the AB band into a filled lower Hubbard band (LHB) and an empty upper Hubbard band (UHB) [Fig. 2.4(a)]. Further, a Mott insulator system has also an antiferromagnetic ground state due to the superexchange interaction [7] between the neighboring spins. This interaction originates from the fact that the two neighboring spins on copper sites could lower the kinetic energy by virtually hopping to the oxygen sites and/or one of the copper site together. The non-bonding band (NB) located between the LHB and UHB bands has essentially an oxygen O-2p origin and the lowest excitation is not a Mott-Hubbard like insulator but instead a charge transfer (CT) type [36] [Fig. 2.4(b)] since the

charge transfer energy Δ is smaller than the on-site Coulomb repulsion ($\Delta < U$). Common for the transition metal oxides, the excitation conducts to $d^9 \rightarrow d^8$ the LHB band and the charge transfer gives an additional hoping from the NB band to the LHB band, which lowers the energy of the system. As a result, the complete process is $d^9 \rightarrow d^{10}\mathrm{L}^{-1}$ where L^{-1} represents a hole in the NB band. When doping the system with holes, a Cu-O hybridization occurs, which strongly binds a hole on each square of O atoms to the central Cu^{2+} ion to form a local singlet called the Zhang-Rice singlet (ZRS) [37] [Fig. 2.4(c)]. The ZRS moves trough the lattice in a similar way as a hole in the single band effective Hamiltonian of the strongly interacting Hubbard model. Since the low energy excitation is mainly the ZRS band, it can also be found in the literature as effective LHB.

Doping the parent insulating cuprates is usually performed by a modification of

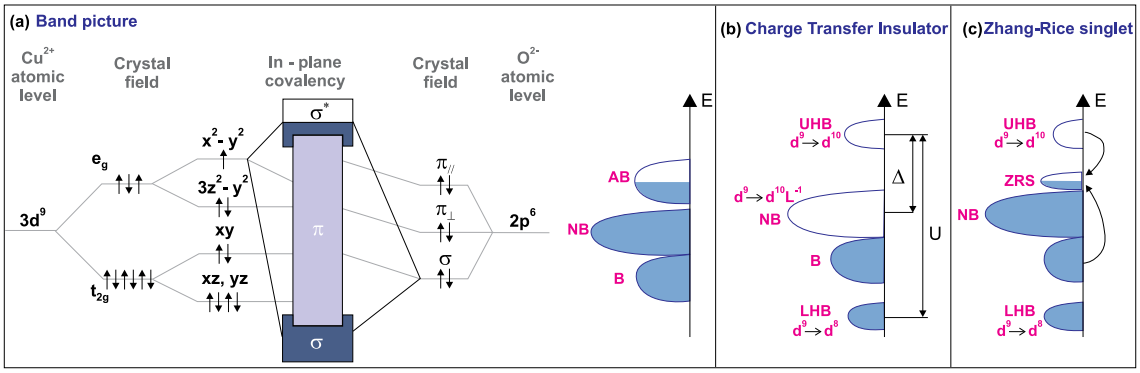

Figure 2.4: (a) Band picture of the hybridization of oxygen and copper orbitals. (b) Charge transfer insulator due to the local $d-d$ Coulomb repulsion. (c) The formation of Zhang-Rice singlet band due to coherence superposition of the four oxygen orbitals surrounding the copper atom. The arrows indicate the transfer of spectral weight due to doping. (Adapted from [35, 38])

the layers separating the CuO_2 planes, either by a heterovalent substitution or by changing the oxygen content. In both cases, the ions introduced into the structure create a modification of the Coulomb potential, which disrupts the lattice periodicity and will be felt as a scattering potential by the carriers in the CuO_2 layers. The doping can be done by either electrons or by holes. In the case of YBCO, the substitution of Y^{3+} ions by Ca^{2+} ions or changing the oxygen content in the CuO chains correspond in both cases to a hole doping. As a result, YBCO becomes a conductor and, under the right condition, superconducting. The phenomenological phase diagram is described in the following subsection.

2.4 The cuprate phase diagram

As mentioned above, the parent compound of HTSC can be doped by changing the carrier concentration of the CuO_2 planes. Upon electron or hole doping, the

cuprate HTSC have rich and complex phase diagrams [Fig. 2.5]. Despite the fact that both phase diagrams (electron or hole doped) look qualitatively similar, their electronic properties in the normal and superconducting states show significant differences. To date, the hole doped family (right side of the phase diagram) has been subjected to a much more extensive theoretical and experimental investigation. In the following, only hole doped cuprates is considered. At zero doping ($x = 0$), the material is an antiferromagnetic (AF) Mott insulator at half-filling as described in the previous subsection. Upon doping, the AF ordering is easily

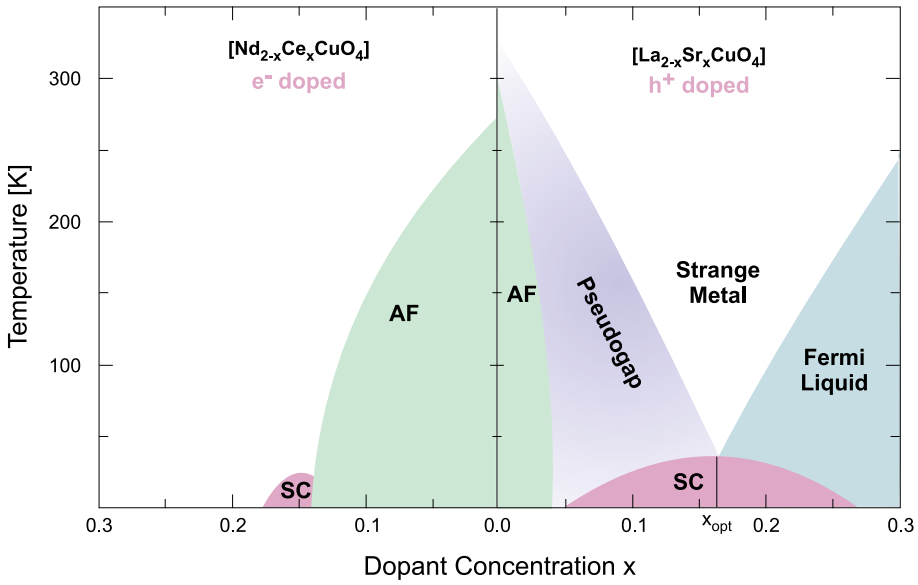

Figure 2.5: Phase diagram of electron (left) and hole (right) doped cuprates (adapted from [39]).

destroyed by only a small amount of hole doping $x \approx 0.05$ giving rise to superconductivity (SC) at low temperatures. By further doping, the superconducting transition temperature T_c rises and reaches its maximum value for an optimum value $x_{opt} \approx 0.16$. Upon additional doping, T_c successively decreases and SC finally vanishes for $x \approx 0.27$, above which a metallic behavior takes place. Here, the x values indicated are essentially valid for the YBCO compound. For convenience, the general phase diagram can be divided in three areas: the *underdoped* (UD) region ($x < x_{opt}$), the *optimally doped* (OPT) region ($x \approx x_{opt}$) and finally, the *overdoped* (OD) region ($x > x_{opt}$). These three regions, enclosed by T_c, is commonly known as the SC *dome*.

The OD regime can be well explained by a Fermi liquid theory, which describes the electronic excitations at the Fermi level in terms of a non-interacting gas of renormalized *quasiparticles*. On the other hand, the OPT regime cannot be described by the classical Fermi liquid theory even though the thermodynamic properties are similar to such description. In fact, this regime is characterized by linear temperature dependence of the resistivity over a large temperature range. Phenomenologically, this can be explained by the marginal Fermi liquid theory [40, 41], where

the scattering rate is a linear function of temperature and energy. However, the normal state properties of the OPT region named also the "strange metal phase", is still inadequately understood. The UD regime is also a very intriguing part of the phase diagram where the so-called *pseudogap* (PSG) presents many anomalous aspects. The main characteristic of this phase is that the gapped state persists up to a temperature T^*, which is well above T_c. Moreover, the PSG seem to have the same symmetry as the SC gap. This interesting state has been intensively studied by various experimental techniques [42], which all conclude a common feature, the reduction (or disappearance?) of T^* when moving into the OPT region [43, 44]. Nevertheless, as well as the OPT regime, the PSG state is unsettled and is still under debate. The PSG phenomena has attracted extensive interests and a main question is if superconductivity arises through the pseudogap state. The comprehension of the PSG state is thus, a very essential subject for HTSC. At present time, two main interpretations are proposed. In the first one, the PSG is considered as a precursor of SC where pre-formed Cooper pairs [45] exist locally but without long-range phase coherence in the normal state. Therefore, the PSG "coexists" with the SC state [46]. In the second case, a "hidden" or "competing" order exists in the PSG state, that is suppressed inside the SC dome. Both scenarios are separately and partly supported by experimental results [47–49] and consequently, the PSG state remains mysterious and under continuous debate.

2.5 $YBa_2Cu_3O_{7-\delta}$ phase diagram

The compound studied in this thesis is YBCO and a brief description of its phase diagram is made. Figure 2.6 shows the phase diagram of YBCO as function of both hole doping p and oxygen content n. At an oxygen content $6.0 \leq n \leq 6.4$, YBCO

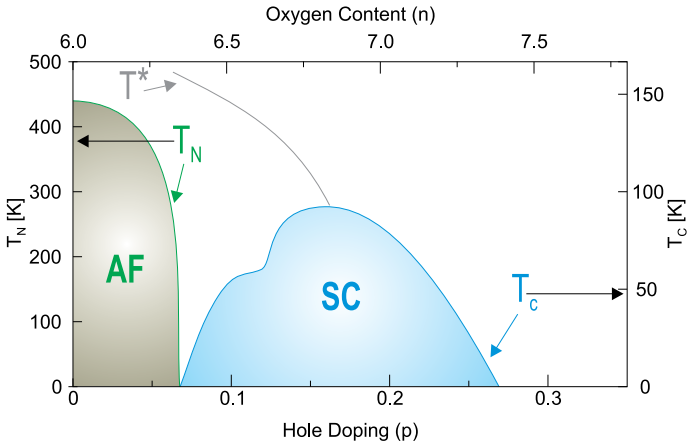

Figure 2.6: Phase diagram of $YBa_2Cu_3O_{7-\delta}$ as function of hole doping p and oxygen content n. (Adapted from [30])

is an insulating material with antiferromagnetic long-range order [50]. When

increasing the hole concentration by transferring holes between the CuO chain and CuO_2 plane, the antiferromagnetic order is destroyed around $n \approx 6.4$ and the compound become metallic and superconducting at low temperature. Considering the SC region of YBCO delineated by T_c in Fig. 2.6 (blue shaded area), two characteristic plateaus at $T = 60$ K and $T = 90$ K are visible. The $T = 90$ K plateau is interpreted as an optimum doping with a small overdoped region while the $T = 60$ K plateau remains controversial [51, 52]. Two main explanations have been developed. The first one suggests oxygen ordering in the CuO chain layers and asserts that the hole concentration p in the CuO_2 planes is unchanged in a certain range of n [53]. The second one assumes that p is changing and instead relates the plateau to the "1/8 anomaly", which is a suppression of T_c at the hole doping of $p = 0.125$ per Cu due to a charge density wave instability (*e.g* charged stripe formation) [54, 55]. At $n = 7$, T_c starts to decrease and SC disappear for $n \gtrsim 7.4$.

2.6 Symmetry of the superconducting order parameter

This section is devoted to the symmetry of Cooper pairs as well as the SC energy gap (Δ) of cuprates. The pairing mechanism of HTSC has for more than fifteen

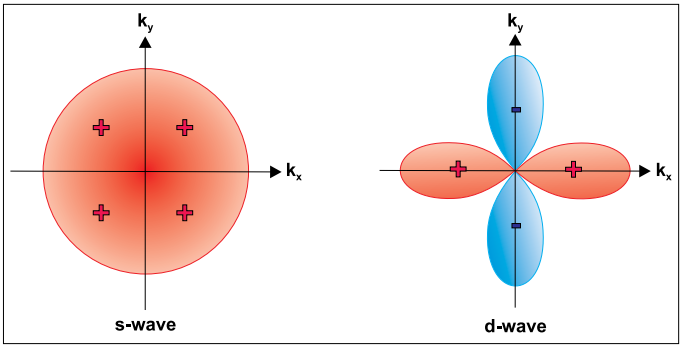

Figure 2.7: Symmetry and phase of the order parameter for conventional *s*-wave (left) and of unconventional *d*-wave (right) superconductors.

years received great attention since the classical *s*-wave pairing [13] for conventional superconductors was found to be invalid. From theoretical point of view, instead of the conventional *s*-wave superconductivity, a $d_{x^2-y^2}$ wave symmetry is predicted [56–60]. Later, in the 1990's, intensive experimental investigations have clearly demonstrated the anisotropic gap structure of HTSC [61, 62] and finally confirmed the *d*-wave nature of the pairing symmetry [63–65]. Moreover, angle-resolved photoelectron spectroscopy (ARPES) conducted during the last decade, has firmly established the $\vec{k}$-dependance of the SC gap and confirmed the existence of nodes ($\Delta = 0$) along the diagonal directions $k_x = \pm k_y$ [66–70].

2.7 Theories concerning cuprates

In the present section, a brief review of theories of high temperature superconductivity (HTSC) is given. A considerable number of theories have been proposed since the discovery of HTSC, but here just four of them are cited. For a more extensive view of different theoretical approaches, see *e.g.* [35, 39, 71].

Phonon-mediated HTSC: As in conventional BCS superconductors, it has been suggested that also in HTSC, lattice vibration mediated by phonons could play an important role [72, 73]. Even though the isotope effect on T_c has been observed for some doping levels, it vanishes at optimum doping. As a result, the isotope effect is still under debate.

RVB: Historically, the resonant valence band (RVB) theory was proposed for quantum spin system with frustration [7]. A simple picture is to view it as an underlaying spin-liquid state, which results in SC when lightly doped with holes. Among several descriptions, the slave-boson method for the t-J model has been widely used [74, 75]. In this theory, two essential excitations, spinon and holon, appear in the mean-field level and couple through a gauge field. The pseudogap state is regarded as a singlet pairing state of spinons and the superconductivity is described as a Bose-Einstein condensation of holons. The RVB approach provides a good explanation of the existence of the PSG region as well as the d-wave symmetry of the gap function.

Hidden/Competing order: In this theory, the PSG is characterized by an order parameter that vanishes at a quantum critical point (QCP) inside the SC dome. The nature of this order is a matter of debate, but one suggestion is that the PSG state is associated with circular current order [76] and the quantum critical fluctuation around the QCP give a reasonable explanation for the strange metal phase. Other hidden orders such as d-density wave order [77] or nematic order have also been proposed [78, 79].

Antiferromagnetic spin fluctuations: Based on the spin fluctuation theory [80], this approach can explain the strange metal phase present above the OPT region. In a highly simplified picture one can assume that spin fluctuations plays the same role as the phonon does for conventional superconductors.

To summarize, the understanding of HTSC is far from complete. Since more than 20 years after its discovery, many physical properties are still unclear. The mechanism of the Cooper pairs or the normal state properties such as the pseudogap and the strange metal phase, are important issues for the understanding of HTSC.

All proposed theories have their strong and weak sides and neither of them can be excluded. Choosing a theory over the another is very delicate and thus, the important role of experiments to distinguish between the different scenarios is apparent. As mentioned in the previous chapter, the main technique used in this thesis is angle-resolved photoelectron spectroscopy (ARPES). This technique has greatly participated to the understanding of the electronic properties of HTSC and a small overview of the main results obtained by ARPES, specifically from YBCO, is presented later in ***Chapter 5***.

3 Pulsed Laser Deposition

Pulsed Laser Deposition (PLD) is a powerful technique, which offers the possibility to grow a large variety of materials. The first thin film made by laser ablation or PLD was done by Smith and Turner in 1965 who used a ruby laser. However, at that period, the technique did not achieve great impact mainly due to laser inefficiency. It is only in the late 1980's with the discovery of HTCS that the PLD was reconsidered. In 1987, the first YBCO films were realized [81] shortly after the discovery of superconductivity in this material. Until now, the PLD technique is still one of the most reliable techniques to synthesize high-quality films of complex oxides in general and HTSC in particular.

In the following subsections, the principle of laser ablation is explained along with a description of the experimental set-up and a review of film characterization techniques. Finally, the substrate preparation and YBCO films deposition procedures established in this project are described in detail.

3.1 Principle of laser ablation

The basic idea of laser ablation [Fig. 3.1(a)] is to focus high-power laser pulses (excimer or Nd:YAG lasers) onto a solid target to evaporate a small amount of material. The impact between the laser spot and the target creates a plasma of atoms named "plume". After many laser pulses, the ablated species condense on the substrate forming a film with the same stoichiometry as the target. The deposition process can be described by four general steps [82–84]:

1. Laser-target interaction
2. Plasma formation (plume)
3. Plume expansion
4. Plasma-substrate interaction

Even if the principle described above seems rudimentary, in practice the process is more complicated and strongly depends on the experimental conditions such as the target quality, gas-pressure, laser wavelength, pulse duration, laser fluence or substrate temperature. In the following sections, the four general steps of pulsed laser deposition process are discussed in detail.

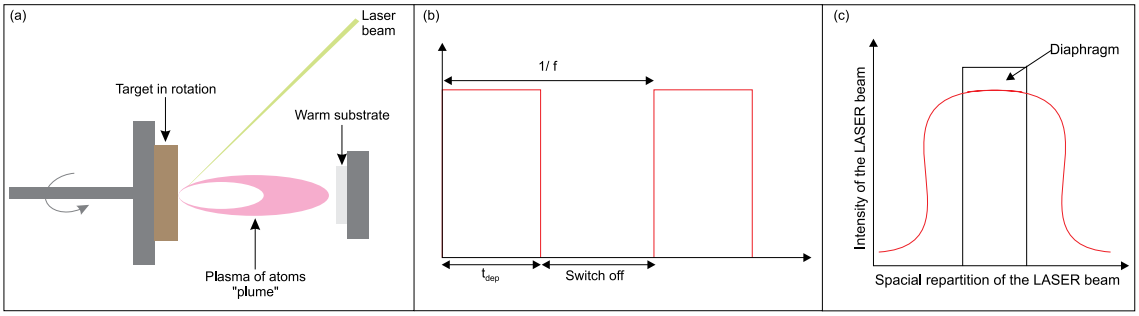

Figure 3.1: (a) Principle of laser ablation. (b) Schematic diagram of a pulsed laser flux in the PLD process. f and t_{dep} are the pulse frequency and duration, respectively. (c) Spatial repartition of the LASER beam (red solid curve). To only select the maximum LASER intensity, a diaphragm (black solid line) is placed before the lens to keep only the maximum intensity.

3.1.1 Laser-target interaction

Typically, the intensity of a laser used for deposition is approximately 10^8-10^9 W/cm^2. Therefore, a pulse duration t_{dep} is on the order of a few nanoseconds, which determine the available time for thermal processes to occur [85]. Figure 3.1(b) shows an illustration of a typical pulsed flux characterized by sharp steps during the pulse duration t_{dep} of a cycle. In this process, the pulse is absorbed, distributed through the material by electron-phonon coupling, which heats up the material and finally vaporizes it. To obtain a homogenous vaporization of the material, the laser beam is cut by a diaphragm to keep only the maximum intensity [Fig. 3.1(c)]. The laser pulse absorption is described by the Beer-Lambert law:

$$I(z) = I_0(1-R)e^{-\alpha(\lambda)z} \tag{3.1}$$

where $I(z)$ is the intensity of pulses in the target at a depth z, I_0 the intensity of the incoming laser beam, R the material reflection coefficient, λ the laser wavelength and $\alpha(\lambda)$ the material absorption coefficient. This last coefficient is related to optical penetration depth δ_a defined by:

$$\begin{aligned} \delta_a &= \alpha^{-1} \\ &= \lambda 4\pi n_2 \end{aligned} \tag{3.2}$$

with n_2 being the extinction coefficient of the material. Then, the energy absorbed will be distributed into the material by thermal conduction. The thermal diffusion length L_{th} measures how deep into the material the depositing energy penetrates during the length of a pulse τ. This is described by:

$$L_{th} = (2\chi\tau)^{1/2} \tag{3.3}$$

where χ is the thermal diffusivity, which depends on the thermal conductivity K_{th}, the material density ρ and the specific heat capacity C_{vap} according to:

$$\chi = K_{th} C_{vap} \rho. \tag{3.4}$$

Considering a thickness N_{th}, ablation can occur if the absorbed energy (E_a) is higher than:

$$E_a > \frac{N_{th}\rho(C_{vap}\Delta T + \Delta H_{vap})}{(1-R)\tau} \tag{3.5}$$

where ΔH_{vap} is the enthalpy of vaporization and ΔT the increasing temperature of the material. The important parameter is how sensitive the target is to the wavelength but also to the length of a pulse. Since the pulse repetition rate is very low, ∼10 pulses/s, the material may be assumed to be completely cooled between pulses. A typical excimer or Nd:YAG pulse delivers 0.2 J into a 0.1 cm^2 area, corresponding to a "fluence" of 2 $J{\cdot}cm^{-2}$. Thus, thermal diffusion and optical penetration depth are the two principal criteria, which influence the laser-target interaction. For example, copper-oxide compounds like cuprate superconductors, which are compounds with rather poor thermal conductivity, are relatively easy to ablate. Here, only the target area covered by the laser spot will be heated, leading to a very local evaporation and ejection of material.

3.1.2 Plasma formation (Plume)

When the laser hits the target, the impact point gets rapidly heated. Atoms and electrons are then ejected from the surface and a thin layer of confined material is created (Knudsen layer). The thickness of this layer is correlated to the optical penetration depth and exist only at the time of a pulse. The Knudsen layer is characterized by three types of particles:

- Particles which are directly connected to the surface
- Particles created by collisions and are backscattered to the target
- Backscattered particles that condenses onto the surface of the target

In general, the Knudsen layer evaporates faster than a pulse length. Indeed, the high temperature at the surface induces almost instantaneously vaporization of the target constituents, followed by the ionization process that produces the plasma.

3.1.3 Plume expansion

Just after its formation, the plasma expands perpendicularly to the target having the shape of a "plume" (hence the name given to the plasma). During the first ∼300 ns the plasma expands unidirectionality (1D), which after it evolves in all directions (3D) creating the final plume [Fig. 3.2].

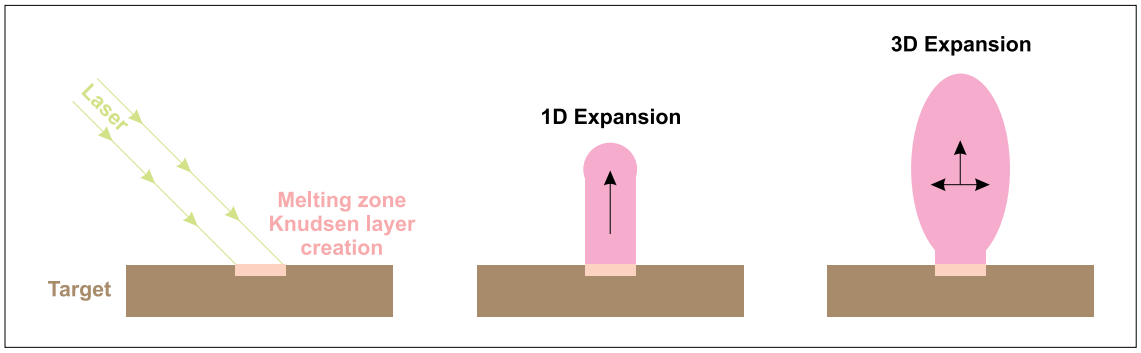

Figure 3.2: Schematics of the plume evolution. The first step is the formation of the Knudsen layer leading to the expansion of the plasma, first in 1D and then finally 3D.

It is possible to distinguish between two kinds of expansion:

- **Expansion under vacuum:** the pressure is on the order of 10^{-5} to 10^{-3} mbar and the plume expands without loosing energy. The particles do not have many collisions and their velocity is about 15 to 90 km·s^{-1} with an energy between 100 and 400 eV. Their mean free path is estimated to 1 mm and the traveling time of the particles between the target and the substrate is on the order of μs. This case is also called *free expansion*.
- **Expansion under controlled gas:** in general, for many materials, the deposition is made under gas pressure. Considering a pressure of 0.1 mbar, the number of collisions between the particles and the ambient gas corresponds to a mean free path of 0.6 mm. At the beginning, the expansion is as in vacuum for a few nanoseconds (free expansion explained above), then like a blast wave and finally the plasma confines itself. The velocity of the particles is then on the order of a few km·s^{-1} corresponding to an energy of approximately 10-100 eV.

Since the plume is the core of the deposition process, many *in situ* techniques have been developed to study its properties and its influence on the film growth.

3.1.4 Plasma-substrate interaction

The main difference between PLD and other techniques, *e.g.* molecular beam epitaxy (MBE) or chemical vapor deposition (CVD), is the high deposition rate of 10^{22} atoms·cm^{-2}·sec^{-1} and the high energy of the particles (1 to 100 eV instead of 0.1 eV). The common point between all deposition techniques is how the films crystallize itself, which can be divided into three main modes [Fig. 3.3]:

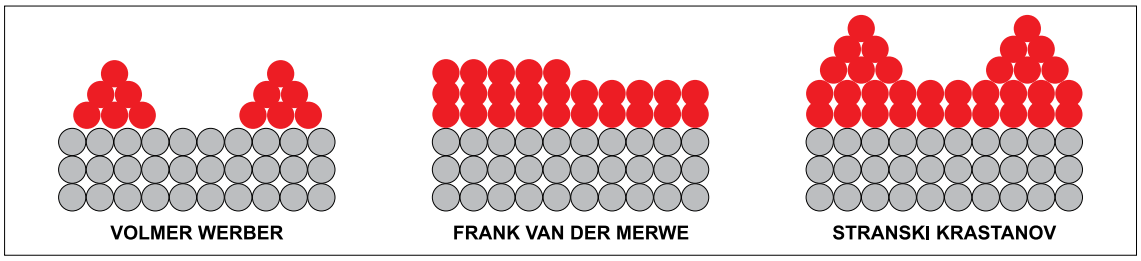

Figure 3.3: Schematics of the different growth modes.

- **VOLMER WEBER**: the atoms condense themselves in 3D islands. Such heteroepitaxial growth is in general not desirable and the surface of the resulting film is generally very rough [86].
- **FRANK VAN DER MERWE**: the atoms attach preferentially to the substrate resulting in atomically smooth and fully formed layers. This layer-by-layer growth is 2D and gives high-quality sample surfaces.
- **STRANSKI KRASTANOV**: It can be seen as a combination of the two modes already mentioned. Above a critical thickness, the film does not grow layer by layer (2D) but as islands (3D). This is in fact the common growth mode for many materials [87].

To produce a high-quality film is a complex process, which depends on many parameters such as the deposition rate, the substrate (temperature and physical properties), the ambient pressure, the target-substrate distance and of course the plume itself. By tuning these parameters, it is possible to favor a specific growth mode. It is also important to mention that one set of parameters can result in nice films for one PLD setup and be completely different in the other. Moreover each materials have their own particularity and a continuous optimization is needed. Growing thin films is far from trivial and requires a lot of patience combined with a systematic and parallel characterization of the output.

3.2 Experimental set-up

The PLD used in this thesis is located at the Surface/Interface spectroscopy (SIS) beamline of the Swiss Light Source (SLS), Paul Scherrer Institute (PSI). A photograph of the PLD machine (named ELLA) used in this thesis is shown in Fig. 3.4 and for more details on the instrument itself see [88]. From the beginning of this project until the first and reproducible films were obtained, almost one and a half year of optimization procedures was needed.

3.2.1 UHV Chambers

ELLA consists of three ultra-high vacuum (UHV) chambers: a load-lock where the substrate can be introduce, a distribution chamber and the main chamber where the deposition takes place. Mounted on an air-cushion platform, the machine can be moved and so, connected via the distribution chamber to other instruments such as the angle-resolved photoelectron spectroscopy (ARPES) end-station. The typical vacuum pressure in each chamber is on the order of 10^{-8}-10^{-9} mbar. For YBCO deposition, oxygen gas is introduced in the main chamber via a leak-valve from PFEIFFER Vacuum Technology. Further, to control the surface quality of the film a reflection high-energy electron diffraction (RHEED) set-up from STAIB Instrument is installed. Recently, the single target holder has been replaced by a double one offering the possibility to grow multilayer compounds. To avoid creating holes in the target, when growing a film, the target is rotated and translated vertically up and down via external motors. The target holder also offers the possibility to have two kind of targets: a cylinder target (rod) or a classical "disc" target (palette). The utilization of a rod target is more delicate since the illuminated area is smaller and defects on the surface are difficult to observe. As a result, the direction of the plume is not always directed towards the substrate, giving inhomogeneous films. Moreover, since a rod target is not the conventional shape for PLD, it requires custom order i.e. longer manufacturing time and a higher price. For these reasons, we decided to switch to a standard disc target bought from Surface Net.

3.2.2 The Laser

The laser is a quadruple frequency (4ω) QUANTEL-Brillant Neodymium: Yttrium-Aluminium-Garnet (Nd: YAG). The amplification stage is composed by of Garnet Yttrium -Aluminium ($Y_3Al_{14}O_{12}$) rod doped with neodymium ions Nd^{+3}. The optical pumping is made with a diode calibrated on the Nd^{+3} absorption peak. The main emission is between the two electronic levels $^4F_{3/2}$ and $^4L_{11/2}$, which appears for a wavelength of 1064.14 nm. Combining with a higher-harmonic generation

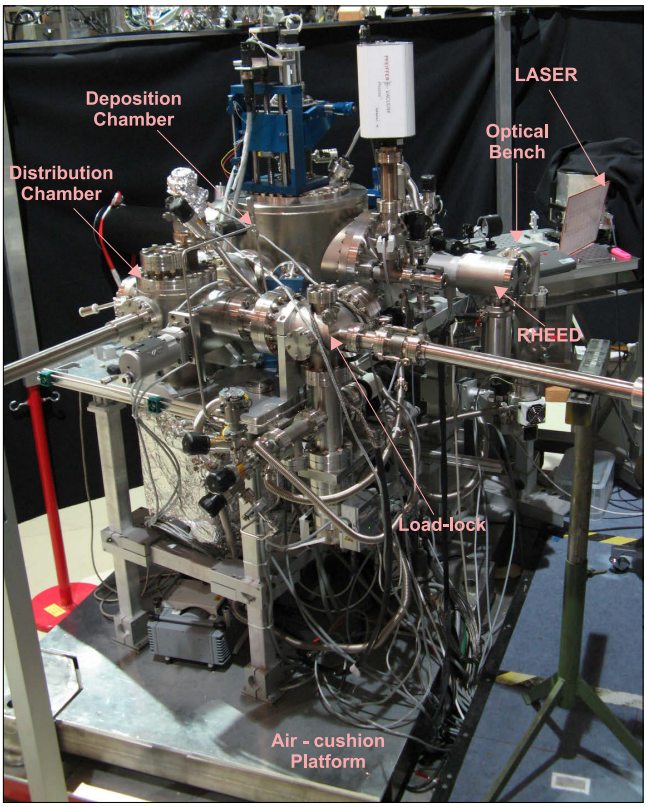

Figure 3.4: Picture of the PLD ELLA at the SIS beamline, SLS.

(HHG) stage, it is possible to obtain doubled (532 nm) and quadrupled (266 nm) frequencies. Therefore, the laser can be use at three different frequencies: 1064 nm (infrared), 532 nm (visible) and 266 nm (ultraviolet). The pulse length is approximately 4 to 6 ns and the energy of a pulse is between 98 mJ to 850 mJ depending of the wavelength. For all depositions, we used $\lambda = 266$ nm with an energy of 80-100 mJ set with an attenuator placed just after the laser. For more details on the laser, see [89]. The laser is focused onto the target by an UV converging lens type with "V-coating" and a focal length f = 600 mm from Laser Component. Further, to keep only the uniform part of the laser beam a diaphragm is used and its energy is measured with a power meter. All these elements are on an optical bench between the deposition chamber and the laser.

3.2.3 Sample holder and heater

One particularity of this PLD setup is the sample holder. An essential point was that each sample made by this system could be transferred/measured *in situ* to the ARPES end-station. Consequently, the holder needed to be compatible for both ARPES and PLD techniques. A picture of the holder is shown in Fig. 3.5(a), where the holder "head" is made of two titanium pieces, the "foot" in stainless

steel and all the parts are separated by a ceramic piece [Fig. 3.5(b)]. The substrate is mounted on a silicon wafer and both are clamped to the holder using two titanium clips. The substrate is heated by injecting a current trough the silicon and the temperature is measured by an external pyrometer from MAURER. Typically, to achieve a temperature of T = 800°C on the substrate, the maximum current is $I_{max} \approx 3$ A. However, the drawback of this system is the non-uniform temperature due to physical defects in the silicon wafer and an non-reproductive clipping procedure causing a heterogenous distribution of the heating current. This induces a

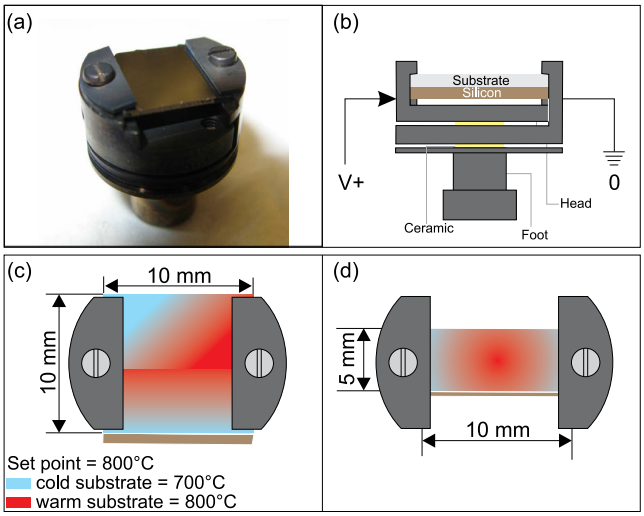

Figure 3.5: (a) Photo of the PLD sample holder with a silicon wafer. (b) Schematic picture of the sample holder. (c-d) Gradient temperature with a (10×10)mm^2 and (5×10)mm^2 substrate. The blue and red colors represent the temperature of the substrate. The (10×10)mm^2 substrate does not have a uniform temperature while the (5×10)mm^2 has a homogenous center.

temperature gradient on the substrate [Fig. 3.5(c)] resulting in an inhomogeneous film. In fact, the temperature of the substrate when growing a film is very important since it directly influences the growth mode (see above). In the present case, the difference in temperature between one part and the other could be as much as 100°C, causing a number of problems, *e.g.* a mix of *a* and *c*-axis oriented YBCO films. By a careful investigation using a pyrometer, it was concluded that the temperature gradient was not reproducible i.e. that the cold part was not always on the same side of the substrate. To compensate for this effect, the size of both silicon and substrate were reduced [Fig. 3.5(d)]. A uniform temperature was then more easily obtained at the center and the film quality was immediately improved. Even trough this solution gave good and reproducible results, the temperature on the substrate borders is still lower than in the center (50-100°C difference). So, when characterizing the films, as well as for the ARPES measurements, only the center part of the sample (3-5×5 mm^2) is taken into account.

3.2.4 Samples Characterizations

To characterized the films, several *in situ* and *ex situ* techniques were used. In this section, a description of these techniques is made.

Reflection high-energy electron diffraction

Electron diffraction techniques are often use to analyze film quality during, as well as after the deposition, and provide important information about the surface. Depending on the kinetic energy, two methods can be distinguished. The first one is at low kinetic energy (20 eV< E_{kin} <200 eV) where the electron beam is directed perpendicular to the surface. This is called low-energy electron diffraction (LEED). The second one is at higher kinetic energy (E_{kin} =5-40 keV) and named reflection high-energy electron diffraction (RHEED). Due to the energy

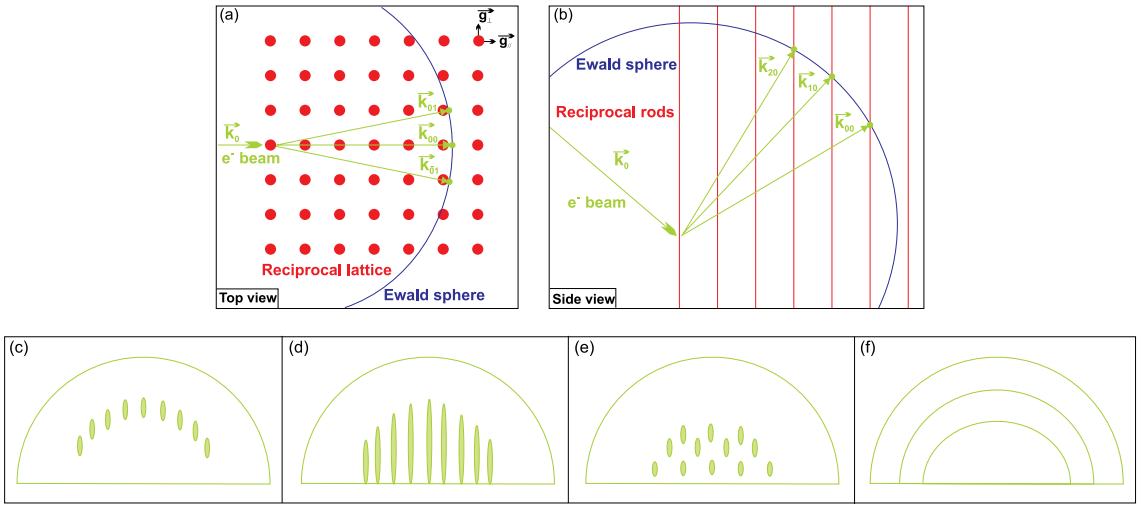

Figure 3.6: Illustration of the operation principle of RHEED for a sample with a cubic lattice. (a) Top view of the reciprocal space and (b) the side view with the so-called reciprocal rods. (c-f) RHEED diffraction patterns. (c) Perfectly smooth surface under the ideal conditions of diffraction. (d) Surface smoothes under experimental conditions. (e) Rough surface. (f) textured surface.

of the electrons, the mean free path for RHEED is higher than for LEED and, hence, it is necessary to have a grazing incidence beam. Since both high and low energy electrons penetrate only a few atomic layers beneath the surface, these two techniques give information mainly regarding the periodicity of the 2D surface lattices with some influence of the underlying layers.

A RHEED system is *a priori* very simple: it requires an electron source (gun), a sample with a clean surface and a photoluminescent screen. The electrons generated by the gun strike the sample at grazing-incident and are diffracted by the

atoms at the surface. The diffracted electrons interfere constructively/destructively at specific angles and form regular patterns on the screen. Figure 3.6(a-b) is a schematic illustration of the operation-principle of RHEED for a sample with cubic lattice. Figure 3.6(a) represents a top view of the reciprocal space of a quadratic array of atoms illuminated by electrons with a momentum $\vec{k_0}$. The electrons arrive at the surface with grazing-incident angle and are scattered from the top layer atoms of the sample. Considering no energy transfer from the electrons to the sample, the scattered wave vector $\vec{k_{ij}}$ lies on the surface of a sphere of constant energy called *Ewald sphere*. Figure 3.6(b) is the side view of the reciprocal space. The 2D arrays of the surface atoms turns into vertical lines named reciprocal rods. The intersection of these rods with the Ewald sphere fulfills the condition for constructive interferences and therefore, determine the directions of the electrons in real space. However, due to the high energy of the electrons, the Ewald sphere is very large compared to the reciprocal lattice spacing, e.g oxide crystals. As a result, only a few reciprocal lattice rods are intersected at the small grazing incident angle. Thus, intersection of the Ewald sphere with the reciprocal lattice rods of a perfect crystalline surface produces sharp diffraction spots lying on Laue circles. Deviations from such perfect surface, like additional roughness and crystal defects, cause broadening of spots or a change in the position and/or intensity of the spots and streaks. A sketch of RHEED diffraction patterns for different surfaces are shown in Figure 3.6(c-f). For a 2D flat surface the expected pattern is streaky lines and for a rough surface or 3D islands, disorganize spots. It is common to have a combination of both patterns specially for thick films where after a certain thickness the growth mode is mainly 3D (Stranski Krastanov mode).

The combination of a RHEED with a PLD is very common since it is a powerful tool for *in situ* analysis of thin film deposition. Its intensity and pattern give information about roughness and its oscillations on the growth process. This two characteristics made the RHEED essential for monitoring surface crystallography during epitaxial film growth. Figure 3.7 illustrates the fluctuating RHEED intensity during a growth process. Each peak represents the formation of a new monolayer that corresponds to an integer coverage number (Θ = 1,2,3..etc.). During the growth of one monolayer ($\Theta \neq 1$), electrons are scattered off the specular direction producing a drop in the intensity (solid green line in Fig. 3.7). The maximum intensity is reached again when a complete layer is formed. This usually corresponds to a full period of these oscillations. Further, the overall intensity is decreasing as more layers are grown. This is because the electron beam is focused on the original surface and as more layers are grown, more surface defects are created, which causes a decreased of the oscillation intensity. Note that the figure is only a schematic illustration similar to those used by film growth experts. However, RHEED and its oscillation of intensity are very complex phenomena. Although, this tool is used for *in situ* monitoring, many details of its nature remains unknown. Several properties and behaviors of the oscillations are not yet understood. For example, some of these problems are the different phases of

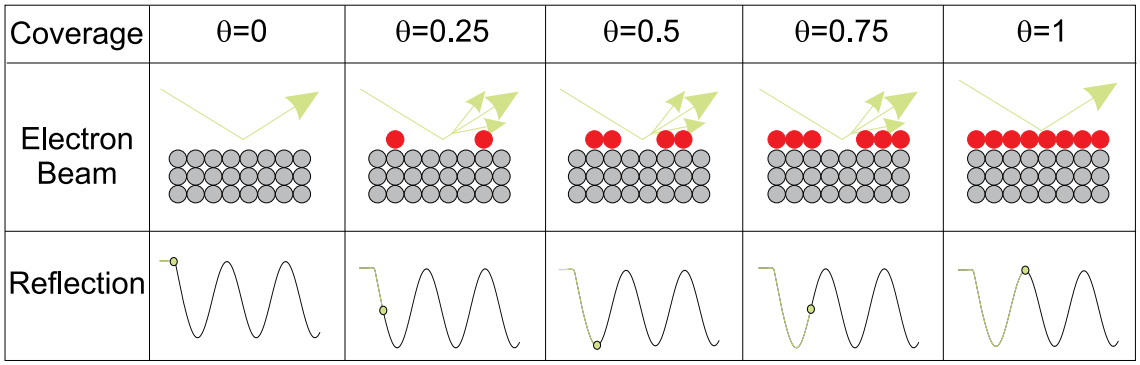

Figure 3.7: Illustration of the RHEED oscillations during deposition process. The substrate is grey, the deposit material red and the electron beam green

the specular and nonspecular RHEED beams [90], and the varied behavior of the oscillations in the case of various materials [91].

In the present PLD set-up a RHEED from STAIB instrument is mounted, however the monitoring mode can only be used for low-pressure deposition ($\leq 10^{-5}$ mbar). Since $SrTiO_3$ (STO) thin-films can be grown at low-pressure, the growth of such films could be observed and the evolution of the surface monitored during growth. For YBCO films, the RHEED was only used after deposition to verify the surface quality since the growth takes place at higher oxygen pressure. A more detailed description of the deposition of YBCO and STO is explained later in section "Substrate and Film Deposition". In order to use the RHEED in monitoring mode at higher pressures (10^{-1} mbar), an additional pumping stage is required and this will be implemented in a near future.

X-Ray Diffraction

X-ray diffraction (XRD) is an *ex situ* characterization tool, which gives information regarding the bulk crystallinity of the films. In this project, a Seifert 3003 PTS set-up with a Bragg-Brentano geometry was used [Fig. 3.8]. The beam is generated by a $Cu - K$ X-rays with λ =1.54 nm corresponding to an energy hν = 8.026 keV. The incident beam penetrates the lattice and scatters from each of the atoms. The incident and scattered angle θ are the same and result in constructive interferences with respect to the Bragg condition:

$$n\lambda \;=\; 2d\;\sin\theta \tag{3.6}$$

where λ is the wavelength of the beam, d the spacing between the atomic planes and n is the path-length difference between beams reflected from successive planes in the z direction. The geometry of a Bragg-Brentano set-up is shown in Fig. 3.8(b). The film surface is oriented in the x-z plane and θ is measured with respect to that

plane. Then, θ is scanned by rotating the sample around the y axis (ω). Simultaneously, the x-ray detector is rotated through 2ω to keep it at the specular angle with respect to the film. At values of 2ω for which the atomic periodicity d perpendicular to the film surface satisfies the Bragg condition, a peak appears. The

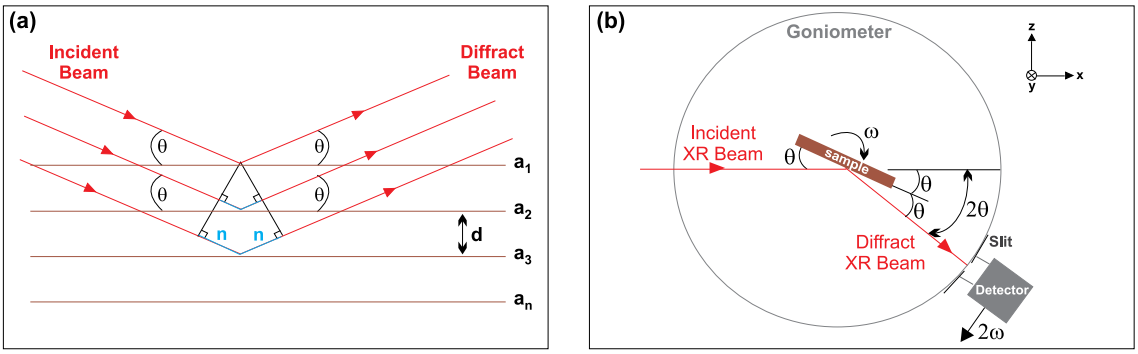

Figure 3.8: (a) Principle of bulk diffraction from a stack of atomic layers a_n. (b) Geometry of a Bragg-Brentano diffractometer.

d value identifies the atomic plane and the peak intensity is a qualitative measure of the crystallinity of the atomic plane parallel to the surface. The crystal grains can also be deduced from the width of the peak at half of its maximum intensity. To determine the degree of atomic ordering, the detector angle 2ω can be fixed at the Bragg angle. Then, the diffracted intensity is measured as the sample is "rocked" around ω. If the film have a close to perfect crystallinity, such so-called "rocking curve" is very sharp.

Resistivity measurement

The YBCO films grown in this PhD thesis project was also *ex situ* characterized by measuring the temperature dependence of the in-plane resistivity, $R(T)$. Here a conventional four-point probe method, also known as the Van der Pauw technique, was used. This is a very simple apparatus for measuring the resistivity of thin-films but gives a first estimate of the superconducting properties. First, four gold contacts are made on the film surface and by passing a current, I, through two outer contacts and measuring the voltage, V, through the inner probes [Fig. 3.9(a)], the resistivity R of the film is deduced using Ohm's law ($R = V/I$). In PSI, a physical property measurement system (PPMS) from Quantum Design has been used to measure the resistivity of the grown YBCO films. All the resistivity measurement were performed in-plane (I parallel to the ab plane) as function of temperature ($T = 10-300$ K). Via this method, the critical temperature T_c of the material is determined and the shape of the $R(T)$ curve gives further information concerning the doping level of the film. A schematic overview for in-plane resistivity in superconducting films is shown in Fig. 3.9(b). For the undoped (insulating) region, the in-plane resistivity first falls with decreasing temperature, attaining its minimum

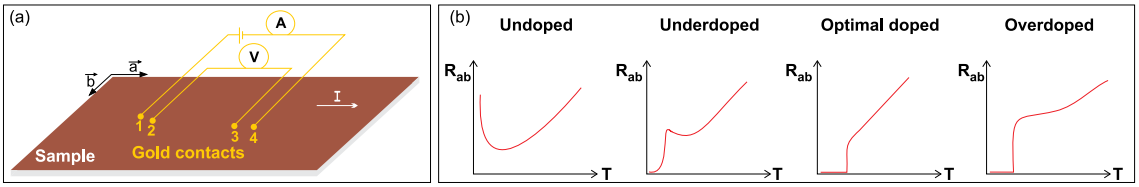

Figure 3.9: (a) Principle of a four-point resistivity measurement. Gold contacts are made on the film and the current is supplied via contacts 1 and 4 and the voltage is monitored via 2 and 3. The white arrow depict the direction of the current I. (b) Schematic overview of the in-plane resistivity of superconducting films for different doping levels.

value and then, sharply increases at low temperatures. For underdoped films, the resistivity passes through a minimum value, attains a maximum and then fall, vanishing below T_c. The sharp fall due to a transition into the superconducting state literally interrupts the rise corresponding to the insulating charge-ordered state. For both optimal and overdoped region, the resistivity is almost linear above T_c, which is connected to a metallic behavior.

Atomic Force Microscopy

To characterize the surface topography of a sample, Atomic force Microscopy (AFM) is one of the most common methods since it provides a 3D profile of the surface on a nanoscale. AFM is based on atomic forces such as Van der Waals, capillary, chemical, electrostatic, magnetic, and other atomic forces. An AFM consists of a cantilever with a small tip that interacts with the surface of the film. When the tip is close to the sample surface, forces between the tip and the surface lead to a deflection of the cantilever. The deflection is then measured by the reflection of a laser spot from the cantilever surface to a photodiode [Fig. 3.10(a)]. The sample is mounted on a piezoelectric tube, that can move the sample in the z direction for maintaining a constant force, and the x and y directions for scanning the sample laterally. Typically, the cantilever is made from silicon (Si) or silicon nitride (Si_3N_4) and the tip radius of curvature is on the order of nanometers. The vertical resolution is on the Ångström scale and tens of nanometers laterally. An electron micrograph of the AFM cantilever with the tip is shown in Fig. 3.10(b). To provide a topographic image of the surface, AFM can be used in two different modes. The first one is the so-called *contact mode* where the cantilever tip is dragged across the surface of the film. The surface is hereby measured directly using the deflection of the cantilever. The disadvantage with this mode is that the tip can easily break, especially on rough surfaces where the atomic forces are strong and may cause the tip to crash into the surface. Further, this method is very slow and in the case where loosely bound adsorbates are present at the surface, it is always a risk that they are "dragged along" by the tip. However,

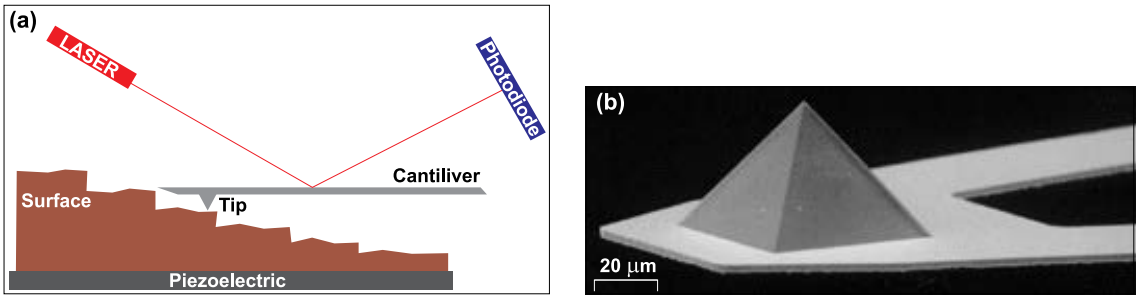

Figure 3.10: (a) Illustration of the AFM principle. (b)Electron micrograph of the AFM cantilever and tip.

once applied to the correct sample the possibility to obtain high-quality images cannot be neglected. The second mode is the so-called *tapping mode*, where the cantilever is driven to oscillate up and down with an amplitude of 20-100 nm near its resonance frequency by a small piezoelectric element mounted in the AFM tip holder. The main advantages for this mode is that it is much faster and the risk of damaging the tip or surface is very low. The tapping mode is the one used in these measurements.

3.3 Substrate and Film Deposition

The substrate plays a crucial role on the film quality/properties. Even if YBCO can be grown on many different substrates, good epitaxial, *c*-axis oriented films are more easily obtained using a strontium titanate $SrTiO_3$ (STO) substrate [92, 93]. In this study, all films are grown on STO (100) due to a very good compatibility

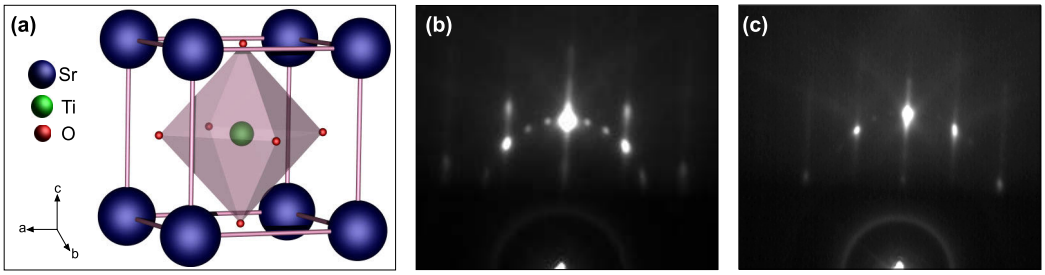

Figure 3.11: (a) $SrTiO_3$ structure. RHEED pictures of $SrTiO_3$ (b) as received and (c) after 4 hours annealing at T = 800°C.

in lattice constants and thermal expansion coefficients. Moreover, the chemical stability of STO and its high-melting point (2080°C) makes it suitable to be used at relatively high deposition temperatures, which is a common condition for growing high-quality crystalline superconducting films.

STO has a perovskite structure (ABO_3) consisting of alternating SrO (AO) and TiO_2 (BO_2) planes [Fig. 3.11(a)]. The surface can have two possible terminations: SrO or TiO_2. In general, as-received substrates have a mix of both terminations with non-regular step, which affects the film-growth and surface quality. Indeed, the termination of the grown film depends on the sequence of the underlying atomic layers, which can be controlled by the substrate termination. For instance, based on atomic force microscopy (AFM) studies [94], the growth of YBCO on TiO_2 terminated STO results in a CuO chain termination of the film. One disadvantage of using STO is that the resulting YBCO film is twinned, i.e. the presence of domains where the CuO chains are oriented in two different directions due to the existing mismatch. To avoid twinning, one can grow the films on $NdGaO_3$ (NGO) substrate, which has lattice parameters (a/b) that are very close YBCO. However, the growth control is much more difficult and as a result the film is often a axis oriented [16, 92, 93, 95].

Various techniques, like ion beam cleaning, bismuth absorption/desorption or annealing are used to improve the surface quality of the STO substrate. Figure 3.11(b) shows the RHEED pattern of an as-received STO substrate. Extra spots are clearly visible between the main lines, indicating a $c(6\times2)$ surface reconstruction. After 4 hours of annealing under vacuum at $T = 800°C$, the spots disappear [Fig. 3.11(c)] and only streaky lines are visible indicating a two-dimensional (2D), atomically flat, crystalline surface. Even though the annealing helps the surface recrystallization [96, 97], this process does not guarantee a surface with single termination and regular step structure. In order to achieve a nearly perfect single termination, an additional chemical treatment of the STO substrate is needed.

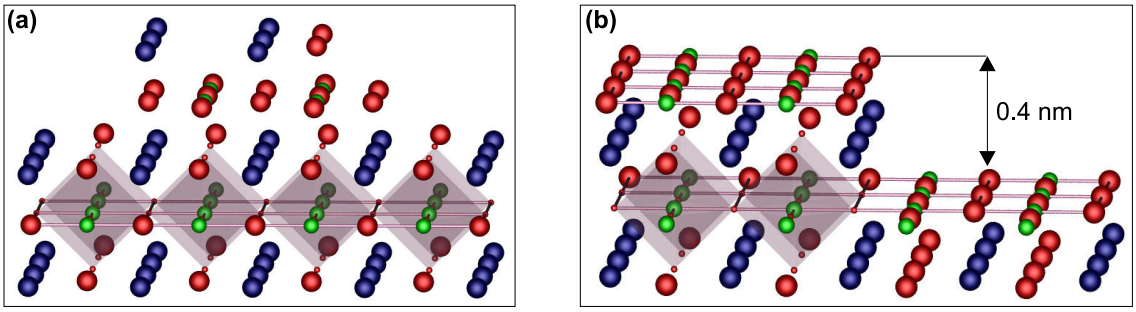

Figure 3.12: Representation of $SrTiO_3$ surface (a) as-received and (b) after chemical etching and annealing. The surface treatment gives a flat surface with a single TiO_2 termination and well-defined atomic steps.

3.3.1 Substrate preparation

Based on the different solubility of the Sr^{2+} and Ti^{4+} ions in acids, a selective etching was first established by Kawasaki *et al.* [98]. Such procedure consists of treating the STO substrate with NH_4 buffered hydrofluoric solution (BHF) of different *p*H value. Such treatment is thought to preferentially etch away the more basic oxide, which in this case is SrO and lead to a uniform TiO_2 surface. However, the reproducibility strongly depends on the polishing and annealing procedures prior to the BHF treatment. This often leads to uncontrolled etching, resulting in pits [97], which obstruct thin film growth. To obtain reproducible and nearly perfect TiO_2 surfaces, Koster *et al.* [99] proposed an intermediate step. The idea is to soak the substrate in demineralized water before the BHF etching. In this step a Sr-hydroxide complex $Sr(OH)_x$ is formed, which would be mostly dissolved by the acid at the step edges, thus leading to a single terminated TiO_2 surface. A complementary post-annealing would finally give a vicinal (stepped) TiO_2 surface. Figure 3.12(a-b) is a schematic view of the STO surface before and after chemical etching and annealing.

It is important to mention that the procedure itself is extremely hazardous and has to be performed in a laboratory made to handle BHF solution. In this perspective, other etchant like Hydrochloric acid (HCl) have been considered [100] giving adequately good results. Based on Koster *et al.*, we have established our own etching procedure, which can be described by three steps:

1. **Cleaning:** To remove the dust particles, the substrate is cleaned with acetone and then ethanol for 10 minutes in ultrasonic bath. Thenceforth, the substrate is soaked in demineralized water for 30 mins. The SrO is given the time to react with H_2O and form the $Sr(OH)_x$ complex, which can be dissolved in acidic solution.

2. **Etching:** The substrate is etched in BHF for 30 seconds followed by soaking in demineralized water for a few seconds to remove any leftovers. Since the etching is chemically selective, it removes preferentially SrO, ensuring that the surface is purely TiO_2 terminated. The substrate is then dried with nitrogen gas to avoid further reactions.

3. **Annealing:** Finally, to recrystallize the surface, an annealing in oxygen atmosphere $P_{O2} = 1000$ mbar is performed at $T = 1050°C$ for 3 hours. The annealing results in a nearly perfect regular step structure (terrace surface), which is mainly TiO_2 terminated.

After annealing, the surface has been studied by AFM. Figure 3.13(a-b) shows the STO surface where a single TiO_2 terminated surface and terrace ledges are observable. It is also clear that the crystal miscut is not only in one direction and that no Sr islands are formed on this surface. Also shown in Fig. 3.13(c), a

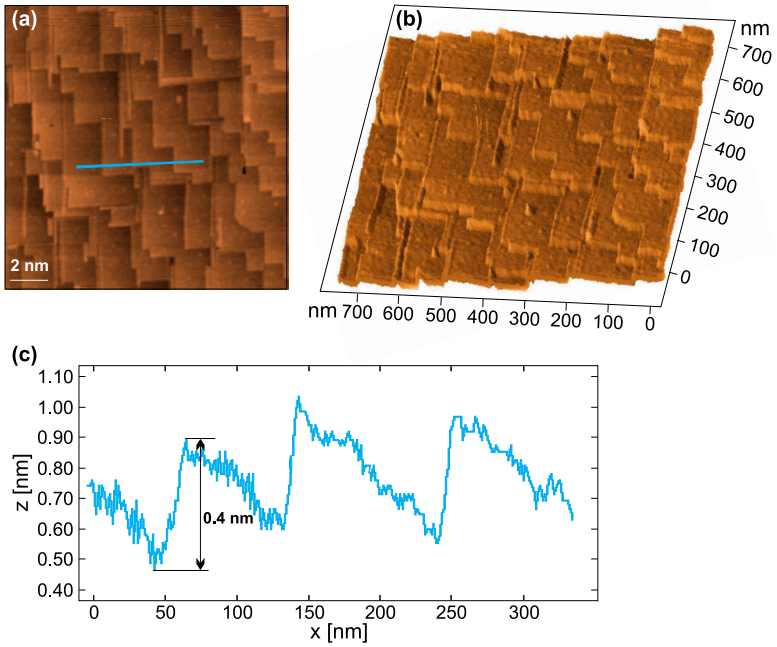

Figure 3.13: (a-b) AFM picture of $SrTiO_3$ after chemical etching and annealing. Clear terraces are visible. (c) Profile along the blue line indicated in (a).

scan profile corresponding to the blue line in Fig. 3.13(a). Single unit cell steps of 0.4 nm height are observed, indicating a nearly perfect atomically flat surface.

3.3.2 Film deposition

STO: Before growing YBCO films with the PLD, a simple deposition of STO on TiO_2 terminated STO substrate was performed. This initial test was made for controlling the monitoring mode of the RHEED. Since STO can be deposited at low pressure, we wanted to control and follow the STO layer-by-layer growth for other investigations. The substrate was first annealed in UHV at $T = 800°C$ for 30 minutes. Figure 3.14(a) shows the RHEED pattern of the TiO_2 terminated STO substrate after annealing. The streaky lines indicate a flat and 2D surface in line with the AFM measurement [Fig. 3.13]. The distance between the STO target and the substrate was $d_{S-T} = 40$ mm and the laser power and repetition rate are set to $P_{Laser} = 80$ mW and $\nu_{Laser} = 2$ Hz, respectively. The ablation was performed under an oxygen pressure $P = 10^{-5}$ mbar and the substrate temperature $T = 800°C$. Figure 3.14(b-c) shows the RHEED oscillations and image recording during the deposition of 10 unit cells (u.c.) of STO. The oscillations indicate a clear 2D layer-by-layer growth mode and the final RHEED image shows a nicely flat surface.

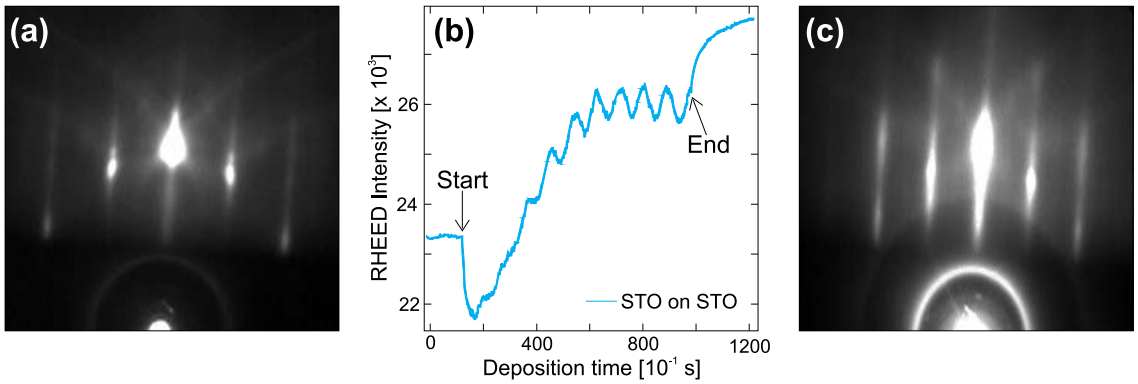

Figure 3.14: (a) RHEED pattern of TiO_2 terminated STO (100) substrate. (b) RHEED oscillations during deposition of STO layers. (c) RHEED pattern of STO film after deposition of 10 unit cells.

YBCO: To obtain good and reproducible YBCO films by using PLD, the correct ablation conditions (oxygen pressure, substrate-target distance, laser power, etc...) needed to be established. To obtain reasonable YBCO films, we first had to change the target since the initial one had a very low oxygen content. Further, we switched geometry from ROD shape to disc-shaped target. Consequently, the grown films where mostly insulating even after oxygen annealing and inhomogenous due to the small area of ablation and non discernable defects. A new disc-shaped target with oxygen content close to seven (i.e. $YBa_2Cu_3O_7$) was bought from SURFACE NET. The two targets geometries are shown in Fig. 3.15. The first parameter to be optimized was the oxygen pressure. The laser power was set to $P_{\text{Laser}} = 90$ mW and by moving the lens on the optical bench, a laser fluence $F = 2\text{-}3$ J.cm^2 (measure of the beam spot on the target) was obtained. Then, by progressively changing the oxygen pressure from 10^{-5} mbar to 10^{-1} mbar, the evolution of the plume shape was investigated. At low pressure, the plasma was narrow and did not really have the correct form of a plume. By increasing the oxygen pressure, the plasma expanded and obtained a correct shape for a pressure $P_{O2} = 0.53$ mbar. Even if the oxygen pressure was set correctly after this optimization, the repetition rate of the laser ($\nu_{\text{Laser}} = 10$ Hz) was too high. Consequently, the atoms did not get enough time to re-organize themselves on the substrate between pulses, inducing a 3D growth

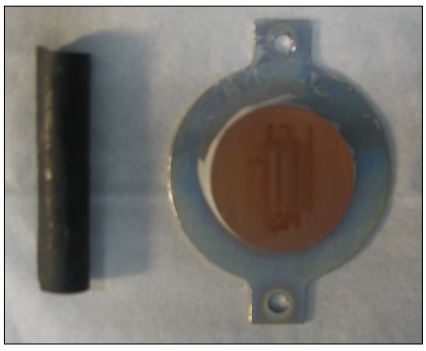

Figure 3.15: Geometry of the PLD targets. On the left, rod target of YBCO and on the right, disc-shaped target of STO.

mode. Further, the target-substrate distance was investigated and as mentioned above the heater was a major problem since the temperature of the substrate was not uniform. When correcting all these parameters, an adequate procedure for growing high-quality YBCO films was obtained according to the following.

Before starting the deposition, the substrate is annealed in UHV at $T = 800°C$ for two hours. The substrate-target distance $d_{S-T} = 30$ mm and the laser power and repetition rate are set to $P_{Laser} = 90$ mW and $\nu_{Laser} = 2$ Hz, respectively. The ablation is performed under an oxygen pressure $P_{O2} = 0.53$ mbar for 30 minutes at $T = 800°C$, which corresponds to a film thickness of 100 nm [later confirmed by *ex situ* profilometry and Rutherford backscattering (RBS), techniques]. Then, the sample is cooled in two steps. First, the temperature is rapidly decreased to $T = 650°C$, followed by ten minutes waiting. After that, the temperature is successively reduced to $T = 580°C$ and then slowly to $T = 450°C$ while simultaneously introducing oxygen little by little in the chamber until $P_{O2} = 200$ mbar at $T = 450°C$. The film is then annealed under these conditions for two hours and finally cooled down to room temperature. The deposition "recipe" is summarized in Table 3.1.

Phases	P_{O_2} [mbar]	$T_{substrat}$ [°C]	d_{S-T} [mm]	P_{LASER} [mW]	ν_{Laser} [Hz]	Time [mins]
Ablation	0.53	800	30	90	2	30
Cooling	0.53	650,450	30	Ø	Ø	5,30
Annealing	200	450	120	Ø	Ø	180

Table 3.1: Deposition parameters of YBCO films.

Immediately after deposition, an initial verification of the film-quality was performed by RHEED. Figure 3.16(a-c) shows in all sample directions a streaky RHEED pattern, suggesting an atomically flat crystalline surface. Moreover, we can clearly distinguish additional peaks around e.g. (0 1/2) and (0 -1/2) [Fig. 3.16(d-f)] suggesting a unit cell doubling. Later, we also acquired a LEED pattern [Fig. 3.16(g)], which displays a clear (2×1) reconstruction as indicated by the extra weaker spots. Moreover, it is clear that the film is twinned since the (2×1) spots appear in both directions. As mentioned in chapter 2, superstructures in YBCO are not unusual [101] since the oxygen vacancies within the chains tends to order themselves [24, 25]. The influence of the YBCO superstructure found in the film will be developed in chapter 5.

The crystallographic and electrical properties of the film were further investigated by *ex situ* measurements. Figure 3.17(a) shows the X-ray diffraction (XRD) pattern, which displays strong Bragg peaks from both the substrate and the superconducting orthorhombic YBCO phase. The films show strong (00l) orientation with l = 1-7. The rocking curve of the (005) reflection displays a full width half

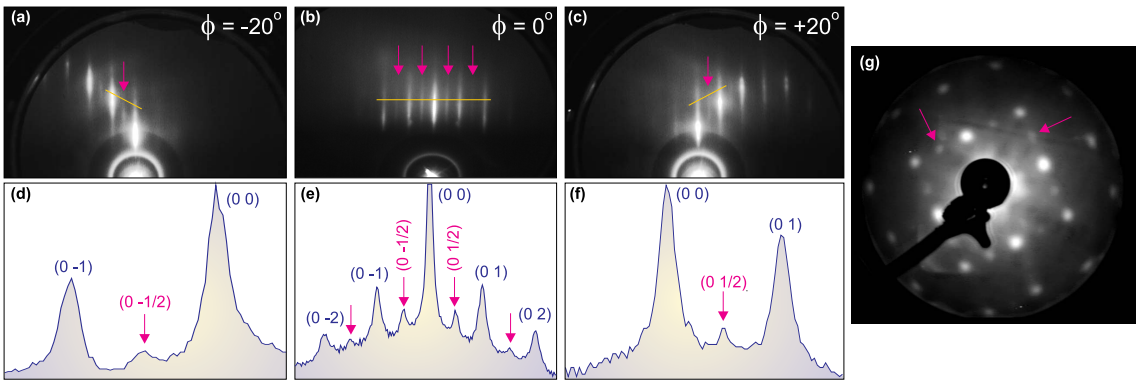

Figure 3.16: (color online) (a-c) Reflection high-energy electron diffraction (RHEED) pattern for different azimuthal orientations of the sample. (d-f) Cut along the solid (yellow) lines in (a-c). All directions show a 2D growth and clear surface reconstruction peaks are visible, e.g. at (0 -1/2) and (0 1/2)(magenta arrows). (d) Low-energy electron diffraction (LEED) pattern showing the extra spots from the (2×1) reconstruction (magenta arrows) in both directions, i.e. twinning.

maximum FWHM $\approx 0.08°$, indicating a good crystallinity. Figure 3.17(b) displays the temperature dependence of the normalized resistance, $R(T)$, measured by conventional four-point probe method. Note that the transition of the film has $T_c \approx 88.9$ K and from the derivative $dR(T)/dT$, $\Delta T_c \approx 0.8$ K is deduced. As expected for hole-doped cuprates, and quantum critical systems in general [49], a linear temperature dependence of the resistivity is found. By a linear fit up to room-temperature (gold dashed line), a residual resistance very close to 0 Ω is obtained, confirming that the film has a low impurity level. In addition, linearity of the $R(T)$ curve in a wide temperature range is a signature of a close to optimally doped sample. The relation between T_c and the number of holes per copper atom in the CuO_2 planes (p_{bulk}) is given by the empirical law [102, 103]:

$$T_c(p_{bulk}) = T_c^{max} [1 - 82.6 (p_{bulk} - p_{opt})^2] \quad (3.7)$$

where T_c^{max}= 92.5 K and p_{opt} is fixed to 0.16. Using Eq. 3.7, we deduce the hole doping of the film to be p_{bulk}= 0.18 ± 0.004 corresponding to $YBa_2Cu_3O_{6.92}$, *e.g* according to the phase diagram in chapter 1 [Fig. 2.6], meaning close to optimal doping (as expected from the target composition). It is important to clarify that the T_c obtained by an $R(T)$ measurements represent the *bulk* properties.

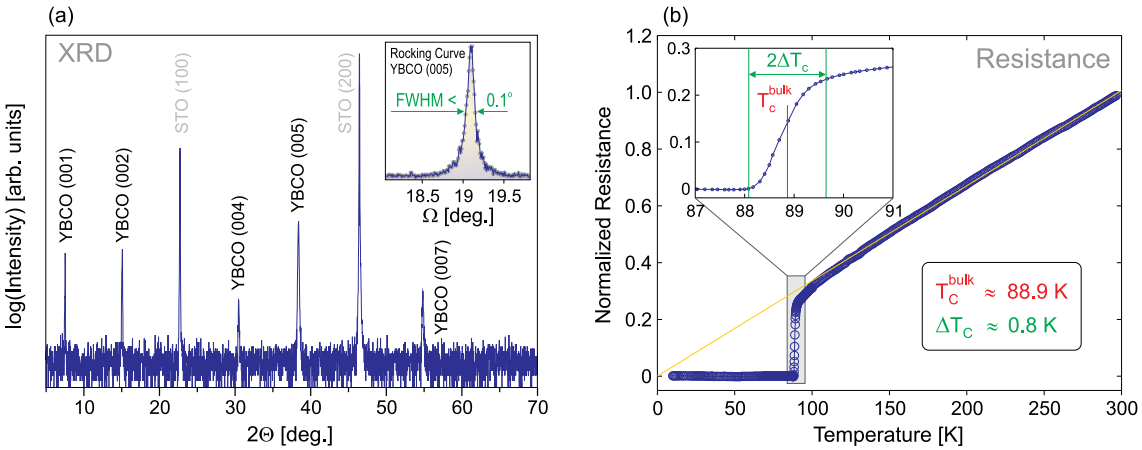

Figure 3.17: (color online) Film characterization data showing (a) X-ray diffraction (XRD) θ-2θ pattern of the film. Inset shows a rocking curve of the YBCO(005) reflection of film. The small value of the calculated FWHM shows good c-axis orientation. (b) Resistance measurements as a function of temperature. Dashed (yellow) line is a linear fit to $T \geq 150$ K giving a residual resistance close to zero. Inset shows $T_c \approx 88.9$ K and $\Delta T_c \approx 0.8$ K.

To summarize, we have managed to grow high-quality and reproducible STO and YBCO films with the PLD set-up ELLA. We have established and optimized current procedures for both substrates preparation and film deposition. The heating system has been improved in order to achieve a homogenous temperature of the substrate and the special rod-shaped target was replaced by a conventional disc-type target. From an extensive *in situ* and *ex situ* characterization we find that all YBCO films display a good crystallinity with a flat and well *c*-axis oriented surface. Further, the films show a close to optimal doping level in the bulk with a very narrow T_c, comparable to single crystalline samples.

4 Photoelectron Spectroscopy

Photoelectron or photoemission spectroscopy (PES) is a technique based on the photoelectric effect. In 1887, Hertz discovered that electrodes illuminated with ultraviolet (UV) light create electric sparks [104]. This observation caught the attention of Thomson [105] and Lenard [106–108] who identified this effect as the emission of electrons. Later, in 1905, based on Max Plank's theory of black body radiation [109], Einstein explained the photoelectric effect [110] by introducing the corpuscular nature of light, *i.e* photons. When shining light to a sample, the photon energy is absorbed and as result, electrons are ejected from the material. Einstein expressed these phenomena in terms of a simple relationship:

$$E_{kin} = h\nu - \omega - \Phi_{sample} \tag{4.1}$$

where $h\nu$ is the photon energy, E_{kin} is the kinetic energy of the photoelectron, ω is the energy of the electron in its initial state (binding energy) and Φ, the work function, which denotes the energy necessary to release the electron from the material. For this explanation, Einstein was rewarded the Nobel Prize in Physics (1921) for his contributions to theoretical physics.

The practical aspects of the photoelectric effect were soon recognized and exploited by means of photocells and, later, photomultipliers [111]. Moreover, PES became an essential tool to study the electronic properties of materials after a series of improvement in other experimental techniques, *e.g* ultrahigh vacuum (UHV), the design of electron analyzer and the development of synchrotron radiation. In the following part, the PES principle is explained, followed by a description of the experimental set-up used in this thesis.

4.1 Principle

The photoemission spectra in solids are interpreted within the single-particle approximation and the Einstein equation (4.1) can be extended to describe all electrons. In a rigorous way, the photoemission process is a quantum mechanical event described by the so-called $one - step\ model$ [112–114]. In this model an electron, under the effect of the electromagnetic field, is removed from an occupied state and

emitted into the detector. In practice, due to the complexity of the crystal structure, correlation effects, multiple scattering etc., a comprehensive and accurate calculation of the photoemission based on the one-step model is not feasible. Instead, photoemission data are usually discussed within the *three – step model* [115–119]. The advantage of this intuitive and phenomenological model has played an important role in the development of PES. Thus, the three-step model is the most common model used nowadays to understand the complicated PES process. This phenomenological approach breaks up the PES procedure into three steps:

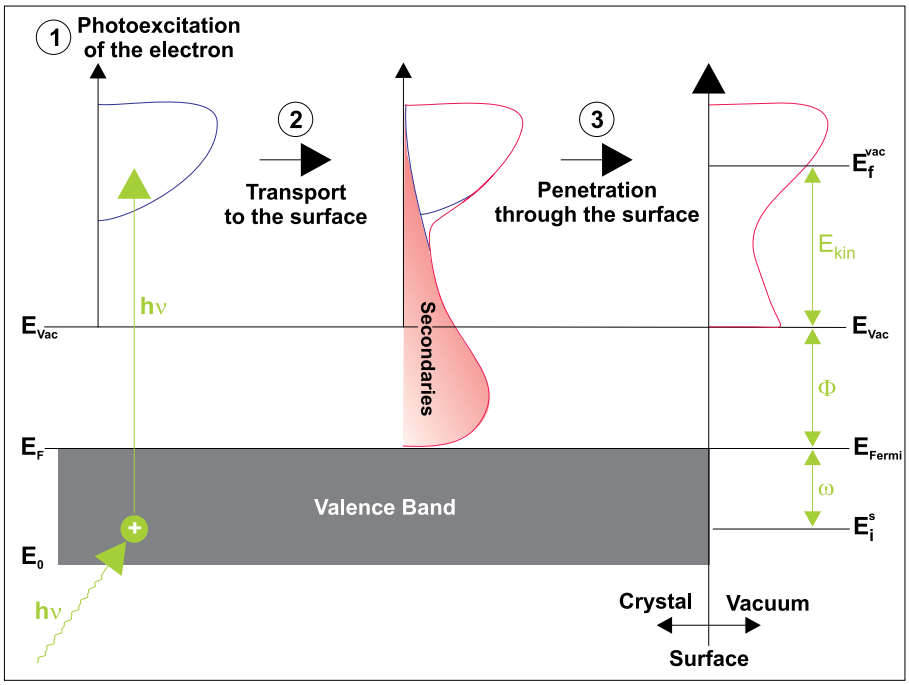

Figure 4.1: Three step process of Photoelectron Spectroscopy: ① photoexcitation of electrons followed by ② their traveling to the surface with concomitant production of secondary (*shaded area*) and ③ their penetration through the surface (*barrier*) and finally, their escape into the vacuum (adapted from [119]).

1. Excitation of the photoelectron;
2. Transport of the electron to the surface;
3. Escape of the electron into vacuum.

An illustration of the three-step model is shown in Fig. 4.1. In step ①, an incident monochromatic light with a well-defined photon energy $h\nu$ is shined upon the material. The photon energy is absorbed and an electron is excited from an initial state to a final state under the law for conservation of energy and momentum

$$E_f^s - E_i^s - h\nu = 0 \tag{4.2}$$

$$\hbar\vec{k}_f^s - \hbar\vec{k}_i^s - \hbar\vec{k}_\gamma - \vec{G} = 0 \tag{4.3}$$

where E_f^s , E_i^s and $\vec{k}_f^s$, $\vec{k}_i^s$, $\vec{G}$ are the energy and wave vector of the initial and final states and the reciprocal wave vector in the solid, respectively. For photon energies in the UV region, the wave vector of the impinging photon $\vec{k}_\gamma$ is negligible compared with the crystal momentum of the electrons in the Brillouin zone (BZ). Hence, the first step can be simply considered as a vertical transition from the initial state at E_i^s to the final state at E_f^s.

In step ②, the electron travels through the solid to the sample surface. During this movement, the electron can be inelastically scattered. If such scattering event occurs, the kinetic energy and momentum of the emitted electron would be different, resulting in a background signal of secondary electrons in the photoemission spectra. The scattering rate of a propagating electron can be estimated via the electron mean-free path λ_{mfp}, which defines an average distance of the traveling electrons without losing energy through collisions [120]. The "universal" electron

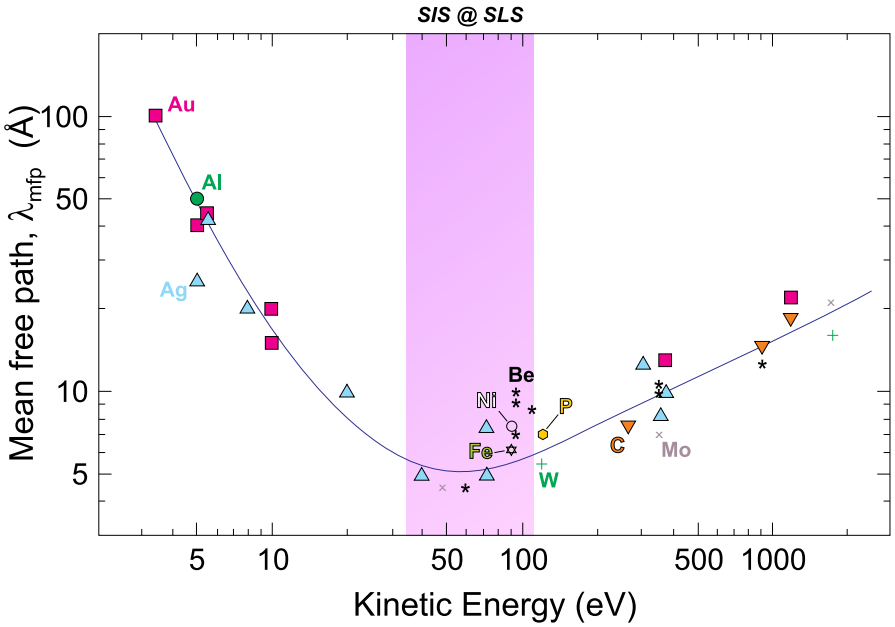

Figure 4.2: Universal curve of the electron mean-free path for various metals [121]. The shaded region represents the range of photon energies used in this thesis.

mean-free path curve as a function of the kinetic energy for different materials is presented in Fig. 4.2. The shaded region corresponds to the photon energies used in this thesis, which are also the energies most commonly used in modern (angle-resolved) PES experiments. As seen, this corresponds to the minimal escape depth of ~ 5 Å. Consequently, photoemission experiments probe essentially the electronic states in the surface region of the sample and is therefore,

considered to be a surface sensitive technique. By tuning the photon energy to either higher (soft X-ray) or lower (LASER) energies, it is possible to increase the mean-free path of the electron and hereby conduct a more "bulk-sensitive" PES experiment. It is important to specify that bulk-sensitive in PES *jargon* means that the maximal escape depth of the electron is approximatively 15-30 Å. Only three synchrotrons in the world offers the possibility to use the soft x-ray ARPES technique including the Swiss Light Source (SLS), at the ADvanced RESonant Spectroscopies (ADRESS) beamline [122] where the photon energy ranges from 400 eV to 1.8 keV.

In step ③,the transmission of the photoexcited electrons into vacuum occurs if their kinetic energy normal to the surface is sufficient to overcome the surface potential barrier. Hence, the electrons must satisfy the condition

$$E_f^s \geq (E_{vac} - E_0) \tag{4.4}$$

$$(\frac{\hbar^2}{2m_e})\vec{k_f^s} \geq (E_{vac} - E_0) \tag{4.5}$$

where the electrons travel in a potential (E_{vac} - E_0) inside the crystal. E_0 is the energy of the bottom of the valance band, E_{vac} is the vacuum level, m_{e} is the mass of the electron and $\vec{k_f^s}$ is the wave vector of the excited electron inside the solid. The transmission of electrons through the surface leaves the parallel component of the wave vector conserved such as:

$$\vec{K_\parallel^{vac}} = \vec{k_\parallel^s} \tag{4.6}$$

where $\vec{k_\parallel^s}$ is the electron momentum inside the solid, $\vec{K_\parallel^{vac}}$ the electron momentum in the vacuum. However, the perpendicular component of the wave vector $\vec{k_\perp^s}$ is not conserved, since the crystal is no longer periodic along the perpendicular direction due to the sample surface. The kinetic energy of the emitted photoelectron is defined as:

$$\begin{aligned} E_{kin}^{vac} &= \frac{\hbar^2(\vec{K_\parallel^{vac}}^2 + \vec{K_\perp^{vac}}^2)}{2m_e} \\ &= E_f^{vac}(\vec{k}) - E_{vac} \end{aligned} \tag{4.7}$$

where $E_f^{vac}(\vec{k})$ is not a single plane wave but a Bloch wave containing plane-wave contributions with a number of reciprocal lattice vectors $\vec{G}$.

Finally, it is important to specify that in the third step, the electron can escape from the sample into vacuum if its kinetic energy is higher than the work function of the material Φ_{sample}. In reality, the sample and the analyzer are both grounded,

i.e in electrical contact, hence their Fermi levels are aligned. As a consequence, the work function of the measurement

$$\begin{aligned} \Phi_{meas} &= \Phi_{sample} - (\Phi_{sample} - \Phi_{analyzer}) \\ &= \Phi_{analyzer} \end{aligned} \tag{4.8}$$

is the work function of the analyzer and not the sample. Consequently what is measured in a PES experiment is $E_{kin}^{anlyzer}$ as shown in Fig. 4.3. From this point of view, a very precise knowledge of the $\Phi_{analyzer}$ is required in order to extract ω from the experiment. This calibration problem is usually solved by measuring, at the same photon energy, both the spectrum of interest and a Fermi edge of a metallic reference in electrical contact with the sample. By evaluating the difference between the two obtained kinetic energies all unknown factors are cancelled and ω is obtained.

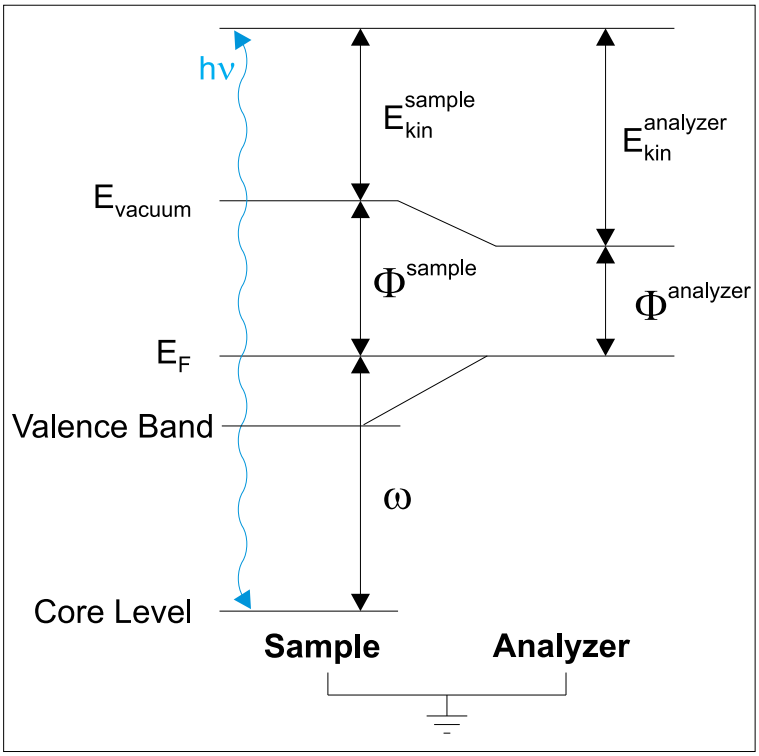

Figure 4.3: Schematic energy diagram for the photoemission process from a sample in electrical contact with the electron analyzer. (Courtesy of Dr. Martin Månsson [123].)

4.2 Angle-Resolved Photoelectron Spectroscopy (ARPES)

If one records not only the kinetic energy of the detected electrons but also their emission angles, the experimental technique is called angle-resolved photoelectron spectroscopy (ARPES). The basic geometry of an ARPES measurement is shown in Fig. 4.4.

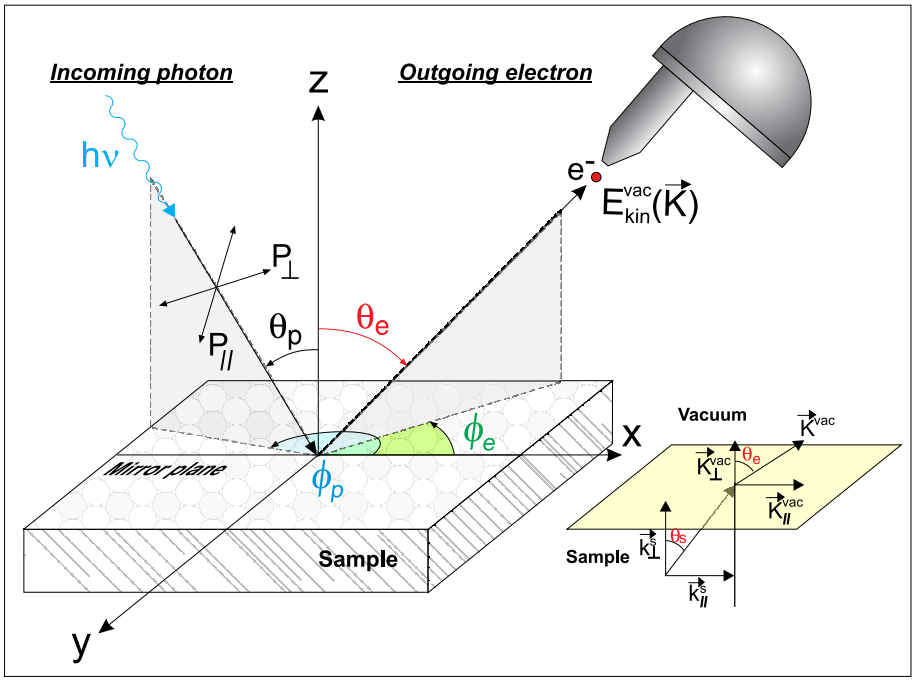

Figure 4.4: Basic geometry for an ARPES experiment. Polar and azimuthal (θ and ϕ) angles of the incoming photon (p) and outgoing electron (e), polarization (P) of the light, and kinetic energy (E_{kin}^{vac}) of the photoelectron are displayed. The inset to the right shows how the parallel component ($\vec{k}_{\parallel}^{s}$) is conserved while the perpendicular component ($\vec{k}_{\perp}^{s}$) is not. (Courtesy of Dr. Martin Månsson [123].)

Considering the angles inside and outside the solid [Fig. 4.4], θ_s and θ_e, respectively, and equation 4.6, the conservation of the parallel momentum can be written:

$$\vec{k_i^s} \sin\theta_s \;=\; \vec{k_f^{vac}} \sin\theta_e \tag{4.9}$$

with

$$\sin\theta_s \;=\; \left(\frac{E_f^{vac}}{E_f^{vac}+V_0}\right)^{\frac{1}{2}} \sin\theta_e \tag{4.10}$$

where the inner potential V_0 is the energy difference between E_{vac} and E_0. The momentum $|K_{\parallel}^{\vec{vac}}|$ and $|K_{\perp}^{\vec{vac}}|$ can be deduced by:

$$\begin{aligned} |K_{\parallel}^{\vec{vac}}| &= \sqrt{\frac{2m_e E_{kin}^{vac}}{\hbar^2}} \sin\theta_e \\ &= 0.5123\sqrt{E_{kin}^{vac}} \sin\theta_e \\ &= |\vec{k_{\parallel}^s}| \end{aligned} \tag{4.11}$$

$$|K_{\perp}^{\vec{vac}}| = \sqrt{\frac{2m_e E_{kin}^{vac}}{\hbar^2}} \cos\theta_e \tag{4.12}$$

Although $\vec{k_{\parallel}^s}$ is determined by the equations (4.6) and (4.11), $\vec{k_{\perp}^s}$ remains unknown and its connection with $K_{\perp}^{\vec{vac}}$ is not straightforward. Nevertheless, with additional assumptions such as a free-electron like behavior of the final state, $\vec{k_{\perp}^s}$ can be calculated. The free-electron final state is:

$$E_f^{vac}(\vec{k_f}) = \frac{\hbar^2 \, \vec{k_f^s}^2}{2m_e} - V_0 \tag{4.13}$$

However, the assumption of the free-electron final state has limits and its validity essentially depends on the material studied and what photon energy is used. At low photon energies (10 eV $\leq$ hν $\leq$ 100 eV), this assumption only works satisfactory for *e.g* valence band (VB) spectroscopy of metals. When considering correlated materials (*e.g.* CoO [123]), this approximation breaks down.

For 2D, quasi-2D materials or layered compounds like cuprates, the dispersion of the energy bands along the $\vec{k}_{\perp}$ direction is rather small and considered to be negligible [66]. In this case, the relation between energy and momentum is simplified and the Fermi surface (FS) can be mapped out by following the energy distribution curves (EDC) or momentum distribution curves (MDC). Figure 4.5(a) shows a typical ARPES spectrum where the intensity is displayed as function of momentum and binding energy. Figure 4.5(b) and (c) display the two type of curves MDC and EDC, respectively, extracted from the excitation spectrum. However, regardless of their quasi-2D structure, recent ARPES experiments on HTCS at high and low photon energies shows a significant change of the FS [124]. The FS modification can be attributed to either the change in probing depth suggesting dissimilarity of the intrinsic electronic structure between surface and bulk regions, or a considerable *c*-axis dispersion signaling a strong interlayer coupling. Those issues are still unclear and further investigations are needed.

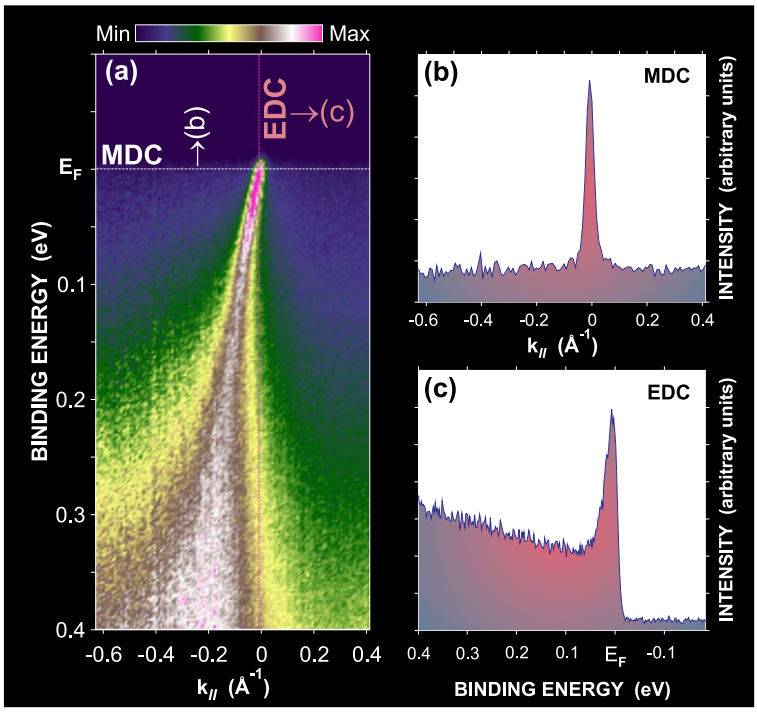

Figure 4.5: (a) ARPES intensity as function of momentum and binding energy. The white and pink lines represent the cut of the momentum distribution curve (MDC) at the Fermi level E_F (b) and the energy distribution curve (EDC) at constant momentum (c), respectively.

For materials with a 3D electronic structure, the $\vec{k_\perp^s}$ component can no longer be neglected. To experimentally determine the band dispersion as function of $\vec{k_\perp^s}$ is only reliable and straightforward if ones uses high photon energies, in the soft X-Ray range (500 ev $\leq$ $h\nu$ $\leq$). Then, by simply scanning the photon energy it is possible to map out the $\vec{k_\perp^s}$-dependence along a certain direction ($\vec{k_\parallel^s}$).

4.3 Experimental set-up

In this thesis, all ARPES measurements were performed at the synchrotron Swiss Light Source (SLS). A brief description of synchrotron radiation and a presentation of the ARPES end-station is made in the following sub-sections.

4.3.1 Synchrotron radiation

Historically, the first observation of artificial synchrotron light was made in 1947 at the General Electric Research Laboratory in New-York [125]. In the last 60 years,

the development of synchrotron radiation evolved constantly and has become an essential research tool for the study of matter.

The main principle of synchrotron radiation is that the acceleration of charged particles induces the emission of electromagnetic radiation. A synchrotron radiation facility is a storage ring for electrons/positrons circling around orbits at large velocity. Each time a circulating electron is accelerated it emits electromagnetic radiation with a certain angular distribution over a certain wavelength spectrum. At non-relativistic speed ($v \ll c$), an electron moving in a circular orbit, emits radiation with a distribution pattern of an oscillating dipole or a classical antenna. However, for an electron moving at relativistic speed ($v \approx c$), the radiation pattern experiences strong focusing into a narrow cone in the tangential direction. An illustration of the emitted radiation at $v \ll c$ and $v \approx c$ is presented in Fig. 4.6(a-b) [126, 127]. In general, a synchrotron radiation facility such as SLS is composed

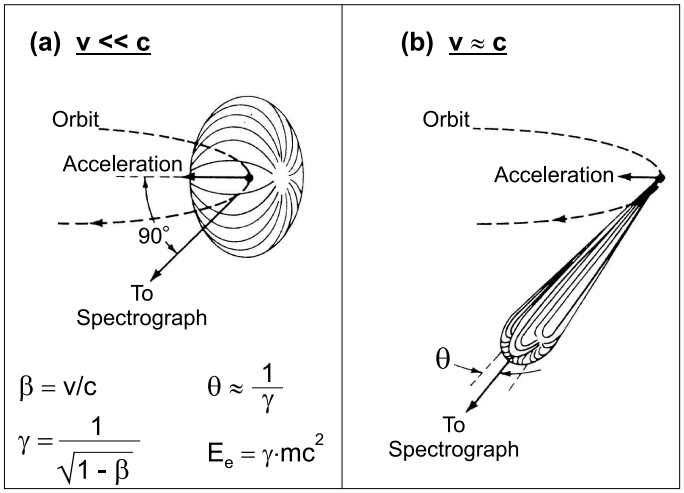

Figure 4.6: Schematic representation of the radiation emitted by an electron with a uniform speed in a circular trajectory. (a) Non-relativistic speed. (b) Relativistic speed (From refs. [126, 127]).

of three major parts: a LINAC, a booster and a storage ring [Fig. 4.7(a)]. The LINAC or *linear accelerator* pre-accelerates electrons produced by an electron gun. The electrons from the LINAC are subjected to a second acceleration into the booster resulting in an energy of the order of GeV. Finally, these electrons are injected into the storage ring, where the electrons are circulating in an UHV environment. Every time the electrons are turned in the storage ring by a bending magnet, synchrotron light is emitted. The radiation is emitted in a broad continuous wavelength spectrum ranging from the microwave region all the way to hard x-rays. A typical spectral distribution curve of the emitted light obtained from a bending magnet is shown in Fig. 4.7(b). The wavelength of the radiation depends on the kinetic energy of the electrons E and the radius R of the storage ring. The maximum photon flux is then obtained at a characteristic wavelength

λ_c. At SLS, the kinetic energy of the electrons $E = 2.4$ GeV, the storage ring has a circumference of 288 m and was designed to have several straight sections of different lengths (from 4 to 11 m). When circling around the storage ring, a decay of the ring-current is observed. This is principally due to the synchrotron radiation in the bending magnet and the scattered electrons resulting in Bremsstrahlung effect. To compensate for this loss, in SLS the storage ring is gently refilled in a permanent way using the so-called "top-up" mode. As a result, the photon flux (*i.e* ring current) remains more or less constant and experiments can be performed without interruption. [126, 127].

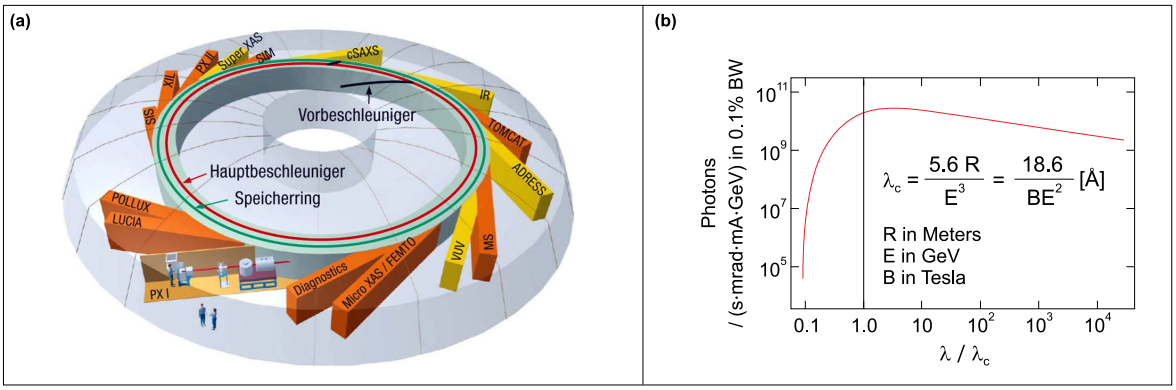

Figure 4.7: (a) Illustration of the Swiss Light Source, third generation synchrotron radiation facility. (b) Typical spectral distribution of synchrotron radiation from a storage ring bending magnet. λ_c is the characteristic wavelength, which depends on the electron kinetic energy E and the radius of the electron storage ring [127].

Third generation facilities, like SLS, make use of *undulators* inserted in the straight sections of the storage ring. An undulator is a periodic magnetic structure, which forces the electron beam to follow a trajectory with a smaller local radius of curvature than in the bending magnets by using a weak local magnetic field. Their design aims at the production of quasi-monochromatic light and the periodic electromagnetic structure gently leads the electrons to oscillate transversely in a given plane (planar undulator) or to describe a helix along its mean path (helical undulator). The angular deflection of the beam is smaller or equal to the natural emission angle of the radiation. In this case, all the beam is concentrated in a narrow cone and the amplitudes of the field radiated at each period of the electrons trajectory may thus interfere, resulting in a periodic radiation field. The resonant wavelengths depend among other, on a dimensionless parameter K, which characterizes the optical properties of the device. K is defined as:

$$\begin{aligned} K &= \frac{eB_0\lambda_u}{2\pi mc} \\ &= 0.934\lambda_u B_0 \end{aligned} \tag{4.14}$$

where B_0 is the magnetic field on the axis of the undulator and λ_u is the periodicity of the undulator . It is therefore possible to tune the wavelength to the desired value by changing the magnetic field strength. Practically, this is done by, *e.g*, adjusting the gap between the upper and lower parts of the magnets. A representation of a typical undulator is shown in Fig. 4.8(a). To conclude, the main advantages of the undulator are its higher brilliance (factor of 1000 higher than the light from a bending magnet) and the possibility to tune both photon energy and polarization.

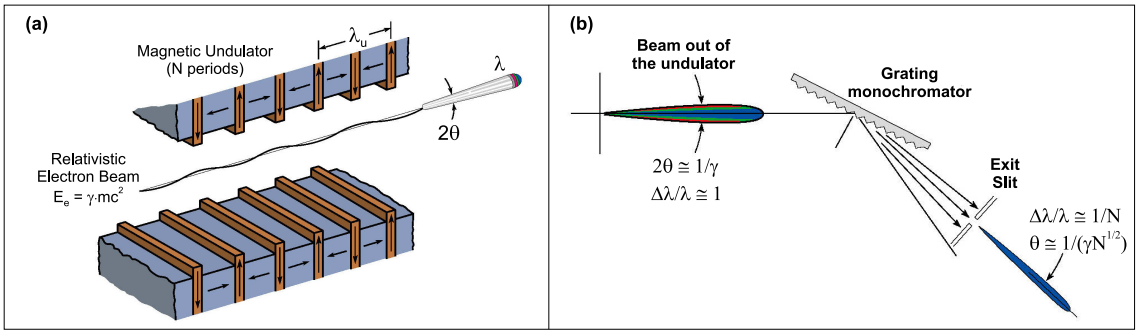

Figure 4.8: (a) Schematic view of an undulator. (b) Schematic view of a plane grating monochromator. N is the number of lines in the grating and $\Delta\lambda$ the bandwidth of the outgoing light (From ref. [128]).

The light emitted from the undulator is guided to the experimental end-station via the beamline. One of the most important element of the beamline is the monochromator, which is in the most common configuration consists of a plane grating and an exit-slit. A schematic view of the beam arriving on the plane grating monochromator is shown in Fig. 4.8(b). The selection of the wavelength is made by tilting the grating and scanning the exit slit. The number of line N of the grating and the size of the exit slit determines the bandwidth $\Delta\lambda$ of the outgoing photon beam. Consequently, when choosing a narrow $\Delta\lambda$, the energy resolution is improved. However, the number of photons decreases resulting in a loss of intensity and the measurement takes longer time. A compromise between energy resolution and intensity is essential for a successful experiment. In the present work, all the experiments were performed in SLS at the X09LA beamline. The technical characteristics of this beamline is reported in Table 4.1.

Beamline X09LA-SIS	Energy range
Linear horizontal	15-800 eV
Linear vertical	100-800 eV
Circular (left and right)	50-800 eV
Beam spot	50 × 100 μm

Table 4.1: Technical characteristics of the SIS beamline.

4.3.2 ARPES end-station

All the experiments reported in this thesis were performed at the ARPES end-station at the SIS X09LA beamline of SLS in Villigen [129]. A detail description of the end-station with the manipulator and the electron analyzer is made.

UHV chambers and connection to the PLD: The ARPES machine is composed of four UVH chambers: a load-lock (PC3), two preparation chambers (PC2 and PC1) and an analyzing chamber (AC). A picture of the SIS end-station is shown in Fig. 4.9(a). The actual ARPES experiment is performed in the AC, that is directly connected to the beamline. The electron analyzer is also connected to the AC and its optical axis is aligned at 45° to the beamline in the horizontal plane. To avoid sample degradation and preserve the high-vacuum of the beamline, the typical pressure is in the order of 5×10^{-11} mbar. To access this main AC chamber, the sample should first be introduced into PC3 and then transferred trough PC2 and PC1. PC1 is the chamber just above AC and contains the manipulator where the sample is mounted. Once the sample is mounted to the manipulator, it can be transferred down into the AC and aligned in front of the analyzer.

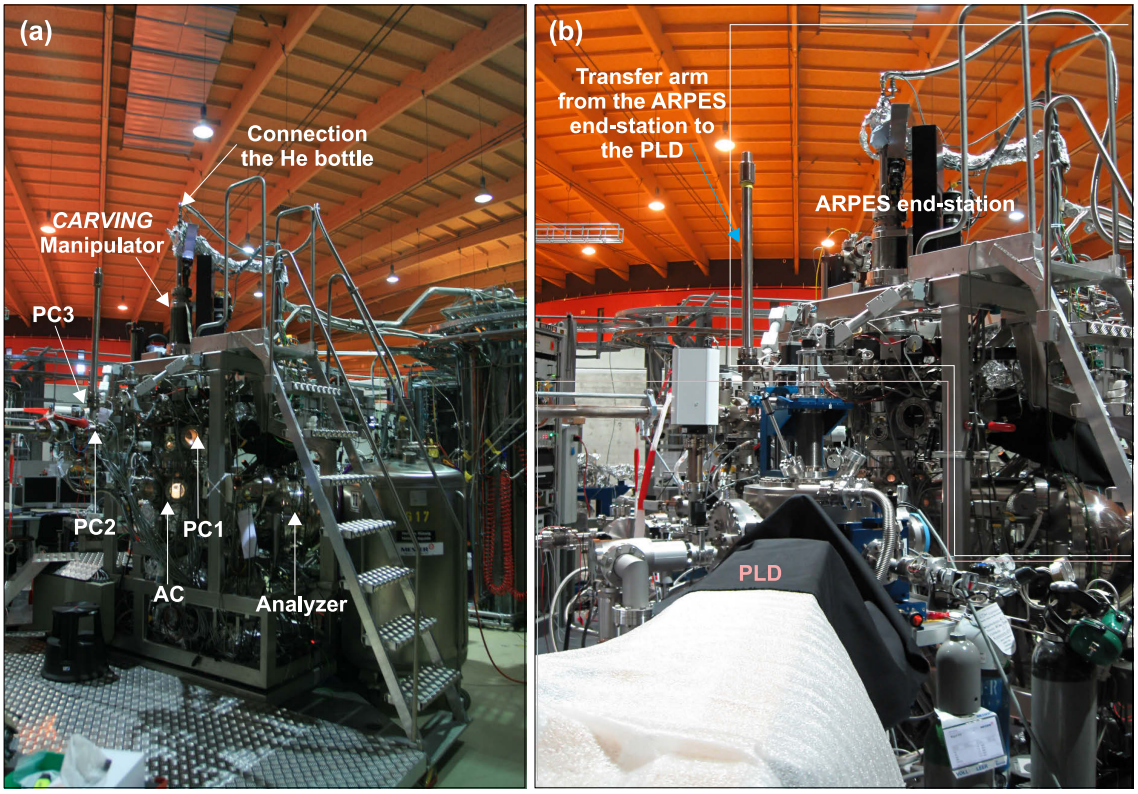

Figure 4.9: (a) Picture of the SIS HR-PES end-station.(b) Picture of the PLD ELLA connected with the end-station.

Since ARPES is a surface sensitive technique, a clean and flat surface is required. The common method to obtain such surface is to *cleave*[1] the sample under UHV (10^{-11} mbar). This process is usually performed in the PC1 chamber and the residual pieces fall down on a shutter that separates the PC1 from the AC chamber. As a result, the AC chamber is protected from contamination. Both PC2 and PC1 have a low-energy electron diffraction (LEED) set-up, which allows to control the surface quality of the sample and its orientation. Sample preparation, *e.g* evaporation of material, sputtering, etc., is usually performed in the PC2 where the typical base pressure is $\sim 3 \times 10^{-10}$ mbar. Further, the PLD can be connected to the ARPES end-station via this chamber [Fig. 4.9(b)]. After growing the film, the sample is directly transfer from the PLD to the ARPES machine using a vertical transfer arm as indicated in Fig. 4.9(b). The *in situ* transfer significantly reduces the risks of contamination and consequently, the sample does not need to be cleaved. The PC3 chamber has a base pressure of low 10^{-8} mbar and a *carousel* where four samples can be introduced at the same time. When measuring films grown by PLD ELLA, PC3 chamber is not used since the film transfer is done from the PLD to the PC2, directly. A final remark is that each chambers are separated by pneumatic valves in order to limit the risk of contamination and to preserve vacuum in the entire system.

Photoelectron spectrometer: The creation of 2D hemispherical electron analyzers in the beginning of the 1990's [130, 131] has played an important role on the study of HTSC. These detectors measure the intensity of photoemitted electrons as function of both their kinetic energy and momentum. Within a single measurement, it provides energy-momentum information along an extended cut in k-space using the so-called $angle - resolved\ mode$. The electrons are first focused by an electron lens on the entrance slit of the analyzer at different positions depending on the direction of their initial momentum. Then, using an advanced technical electro-optical system, each electron trajectories corresponding to different momenta are guided and finally placed along the angular $\vec{k}$ axis of the detector. The angular range of momenta is determined by the *angular acceptance* of the analyzer and the kinetic energy. Further, the detector offers the possibility to select the *pass energy*, which only allows electrons with an energy close to the pass energy to travel along the hemispherical analyzer. Then, depending of their energies and trajectories, the electrons hit the detector at different places along the energy (E) axis, which is orthogonal to the $\vec{k}$ axis. Therefore, the resulting spectrum contains both momentum and energy dependence of the photoelectrons. Electrons with higher or lower energy than the bandwidth of the pass energy, *e.g* bandwidth which corresponds to approximately $\pm$ 10 % the pass energy, cannot reach the detector. However, if one wants to measure them, by applying a voltage on the optical elements of the analyzer, these electrons can be accelerated or decelerated

[1] In its general sense, the word cleave is applied when cutting a diamond as its crystal structure. From physical point of view, it means splitting a single crystal along a natural weakness plane.

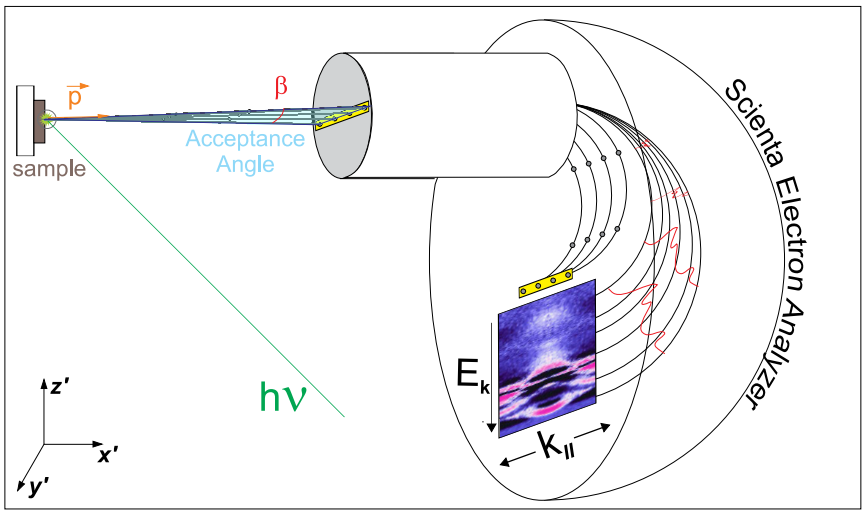

Figure 4.10: Schematic of a hemispherical VG-Scienta electron analyzer. The beam is represented by the green line and the shaded blue region is the acceptance angle of the detector. Note that the orientation of the entrance slit is horizontal. (Courtesy of Dr. Martin Månsson [123].)

in order to match the pass energy of the detector. An illustration of the hemispherical electron analyzer process is presented in Fig. 4.10. Here, the photon beam from the beamline hits the sample where electrons are "kicked out" and guided trough the analyzer resulting in a 2D spectrum. All data shown in this thesis were acquired with the two hemispherical $VG-Scienta$ analyzers SES 2002 and R4000 from Gammadata Mätteknik AB. Their technical comparison are summarized in table 4.2. The above description of the hemispherical analyzer is highly simplified and for more complete explanation/details, see Ref. [131, 132]. As all instruments, the analyzer has a resolution, which can be tuned by changing, *e.g* the analyzer slit or its pass energy. Moreover, depending how the analyzer is attached to the UHV chamber, the slit can be vertical or horizontal. This two geometrical configurations has to be taken into account, particulary when converting the detector angles into $\vec{k}$-space. The transformation for real space to $\vec{k}$-space will be detailed later.

$VG-Scienta$ Spectrometer	SES 2002	$R4000$
Acceptance angle	$\pm$ 7°	$\pm$ 15°
Angular resolution	$<$ 0.2°	$<$ 0.1°
Energy resolution	$<$ 2 meV	$<$ 1 meV
Pass energy	5-200 eV	1-100 eV
Minimal entrance slit	0.2 mm	0.1 mm

Table 4.2: Technical characteristics of the two electron analyzers used in this thesis.

Manipulator CARVING: In order to investigate the reciprocal space of a sample and *e.g*, establish its Fermi surface, one need to make different cuts in $\vec{k}$-space. To perform such measurements at the SIS end-station, a highly sophisticated and motorized manipulator called $CARVING$ with 3 rotational and 3 translational degrees of freedom is accessible. A picture of the rotatable head of $CARVING$ is shown in Fig. 4.11. The rotational motion is composed of a polar (θ), an azimuthal (φ) and a tilt (χ) angle. All motions have a reproducibility better than 0.1°, which makes it possible to obtain very precise cuts in $\vec{k}$-space. The angular ranges of the rotational motion are summarized in Table (4.3). Further, the polar, azimuthal and tilt axes pass trough the center of the sample which means that if the sample surface is uniformly flat, a readjustment of the translational motion should not be necessary. The sample is fixed to the manipulator with a clamping ring and since

Manipulator Angles	*Angular range*
θ	210°
φ	360°
χ	±30°

Table 4.3: Angular acceptance of the CARVING manipulator.

the manipulator is connected to a liquid Helium bottle, the sample can be cooled down. A temperature sensor connected behind the head gives the possibility to regulate the temperature of the sample and with the help of a shielding (orange piece in Fig. 4.11), the lowest reachable temperature is $T = 10$ K. Further, attached above the rotatable head is a heater and the highest feasible temperature is $T = 380$ K. Glued onto the shielding is a fluorescent YAG screen where the photon beam can be detected and marked. Since the $CARVING$ manipulator is used when acquiring ARPES spectra, it is important to mention that all its elements are non magnetic and thus, do not perturb the measurement.

4.3.3 Transformation from real space to $\vec{k}$-space

As explained above, the main function of the $CARVING$ manipulator is to position the sample in front of the analyzer and to give precise access to different cuts in $\vec{k}$-space. However, in view of the analyzer slit (vertical or horizontal), the transformation between manipulator angles (θ, φ, χ) to the reciprocal space is not intuitive and geometrical consideration is necessary. In this thesis work, both vertical and horizontal analyzer slits were used when performing experiments. The transformation of the manipulator angles into $\vec{k}$-space is made for a horizontal slit of the $VG-Scienta$ analyzer since most of the data presented here were acquired with this geometry. As shown in Fig. 4.4, an intrinsic oriented coordinate system $\{x, y, z\}$ of the sample is presented where the z axis is perpendicular to the sample

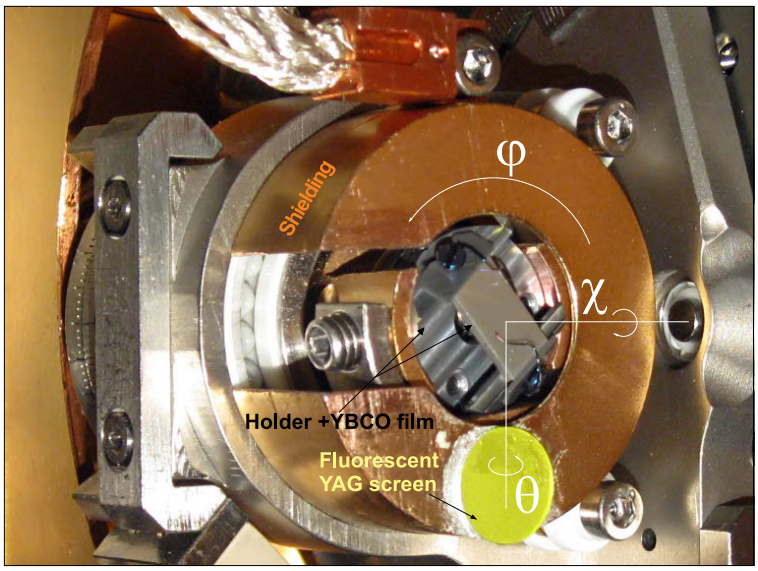

Figure 4.11: Picture of the *CARVING* manipulator with ELLA sample holder and a YBCO film. The polar, azimuthal and tilt angles are noted as φ, θ and χ respectively.

surface, *i.e* normally parallel to the *c*-axis of the sample, and x-y axis corresponds to the high-symmetry directions, *i.e* *a*- and *b*-axis of the sample. Now, let us consider the laboratory coordinate system $\{x', y', z'\}$ with x' and y' axis parallel and orthogonal to the analyzer slit, respectively and z' axis pointing along the optical axis of the analyzer. This coordinate system depends exclusively of the 3 manipulator angles θ, φ, χ and can be defined independently. Figure 4.12(a)

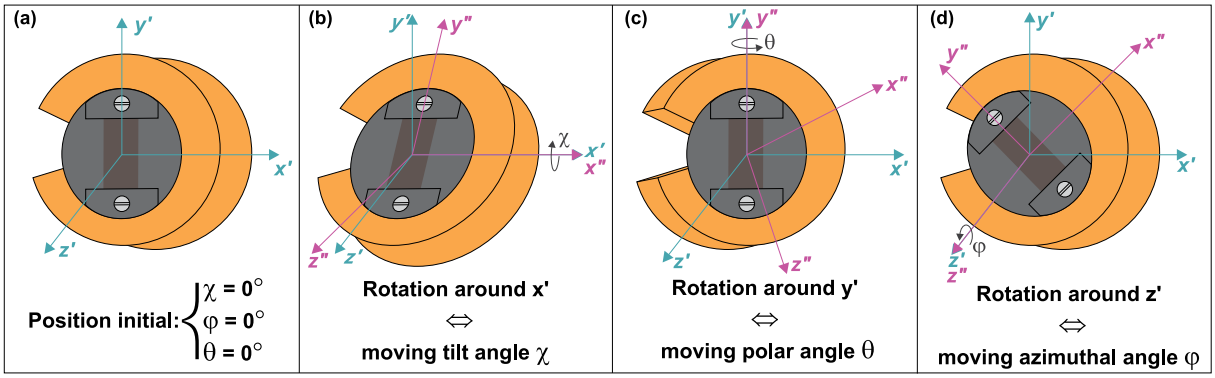

Figure 4.12: Illustration of the *CARVING* manipulator at its initial position (a), when moving χ (b), θ (c) and φ (d). $\{x',\ y',\ z'\}$ represents the intrinsic coordinate system of the laboratory.

represents the *CARVING* manipulator at its initial position and after moving one after each other χ, θ and φ (b-d). Moving only the tilt angle χ from its initial position [Fig. 4.12(b)] is equivalent to a rotation around the x' axis and thus, χ

angle does not affect x'. Taking into account geometrical aspects, the resulting matrix M_χ is:

$$M_\chi = \begin{pmatrix} 1 & 0 & 0 \\ 0 & \cos\chi & -\sin\chi \\ 0 & \sin\chi & \cos\chi \end{pmatrix} \tag{4.15}$$

By applying the same logic on the other two angles [Fig. 4.12(c-d)], one can deduce that θ and φ angles do not affect y' and z', respectively and their corresponding matrices M_θ and M_φ are:

$$M_\theta = \begin{pmatrix} \cos\theta & 0 & -\sin\theta \\ 0 & 1 & 0 \\ \sin\theta & 0 & \cos\theta \end{pmatrix} \tag{4.16}$$

$$M_\varphi = \begin{pmatrix} \cos\varphi & \sin\varphi & 0 \\ -\sin\varphi & \cos\varphi & 0 \\ 0 & 0 & 1 \end{pmatrix} \tag{4.17}$$

As a result, the coordinate transformation can be presented as the product of the 3 matrices[2] mentioned above:

$$\begin{pmatrix} x \\ y \\ z \end{pmatrix} = M_\varphi\, M_\chi\, M_\theta \begin{pmatrix} x' \\ y' \\ z' \end{pmatrix} \tag{4.18}$$

$$\begin{pmatrix} x \\ y \\ z \end{pmatrix} = \begin{pmatrix} \cos\varphi & \sin\varphi & 0 \\ -\sin\varphi & \cos\varphi & 0 \\ 0 & 0 & 1 \end{pmatrix} \begin{pmatrix} 1 & 0 & 0 \\ 0 & \cos\chi & -\sin\chi \\ 0 & \sin\chi & \cos\chi \end{pmatrix} \begin{pmatrix} \cos\theta & 0 & -\sin\theta \\ 0 & 1 & 0 \\ \sin\theta & 0 & \cos\theta \end{pmatrix} \begin{pmatrix} x' \\ y' \\ z' \end{pmatrix} \tag{4.19}$$

The electrons detected by the analyzer can be defined by $|\vec{p}| = \{p\sin\beta,\ 0,\ p\cos\beta\}$ where β is the angle between the electron momentum $p = \sqrt{2mE_{kin}}/\hbar$ and the analyzer acceptance angle [Fig. 4.10]. Considering conservation of the parallel component of the electron momentum and the equations (4.18, 4.19), the coordinate representation of this vector is:

$$k_x = \frac{\sqrt{2mE_{kin}}}{\hbar}\,[\sin\beta\cos\chi\cos\varphi + \cos\beta(\cos\theta\sin\chi\sin\varphi - \sin\theta\cos\varphi)] \tag{4.20}$$

[2]Note that the matrices are not permutable.

$$k_y = \frac{\sqrt{2mE_{kin}}}{\hbar}\,[\cos\beta\sin\theta\sin\varphi + \cos\varphi(\cos\beta\cos\theta\sin\chi - \sin\beta\cos\chi)] \tag{4.21}$$

The transformation from the manipulator angles to $\vec{k}$-space described above is applicable if the crystallographic axis of the sample and the manipulator axis are identical. In real ARPES experiment, a mismatch between those axis is common and consequently needs to be corrected. Let's consider γ, the angle between the z' axis of the manipulator and c-axis of the sample and α, between the x' axis and the a-axis. Correcting the mismatch between the sample and the manipulator axis results in the product of:

$$\begin{pmatrix} x \\ y \\ z \end{pmatrix} = M_{\varphi,\chi,\theta} \begin{pmatrix} \cos\alpha & \sin\alpha & 0 \\ -\sin\alpha & \cos\alpha & 0 \\ 0 & 0 & 1 \end{pmatrix} \begin{pmatrix} \cos\gamma & 0 & \sin\gamma \\ 0 & 1 & 0 \\ -\sin\gamma & 0 & \cos\gamma \end{pmatrix} \begin{pmatrix} \cos(-\alpha) & \sin(-\alpha) & 0 \\ -\sin(-\alpha) & \cos(-\alpha) & 0 \\ 0 & 0 & 1 \end{pmatrix} \begin{pmatrix} x' \\ y' \\ z' \end{pmatrix} \tag{4.22}$$

where $M_{\varphi,\chi,\theta} = M_\varphi M_\chi M_\theta$.

All the $\vec{k}$ points that can be detected by the analyzer at a given manipulator position corresponds to a parallel curve segment, which varies over the acceptance angle interval $-\beta_{min} < \beta < \beta_{max}$. It is called the *slit image* and varying the manipulator angles induce a change of its position in $\vec{k}$-space. It is important to specify that all the $\vec{k}$ lie within a sphere with a radius r. Further, the curvature of the slit image depends strongly on the photon energy. By increasing the photon energy both the accessible momentum space and the momentum coverage of the slit image is enlarged. However, increasing the photon energy induced a loss of energy resolution and a change in the out-of-plane component. In two-dimensional systems like cuprates, this poses no large problem, since no energy dispersion is expected as a function of the $\vec{k_\perp}$ coordinate. For the transformation from the manipulator angle to $\vec{k}$-space with a vertical slit of the analyzer, see Ref. [133].

4.4 ARPES and HTSC

This section is made in two parts: the first one aims to explain how to perform ARPES data analysis and the second part is a summary of the main results resulting from this technique.

4.4.1 Analyzing tools

This section is devoted to explaining how the ARPES data analysis can be performed for HTSC materials. Assuming the validity of the sudden approximation [134], the intensity spectrum measured in an ARPES experiments is given by:

$$I(\vec{k},\omega) = I_0(\vec{k}) f(\omega) A(\vec{k},\omega) \tag{4.23}$$

where $\vec{k}$ is the initial state momentum, ω is the energy relative to the chemical potential μ and $I_0(\vec{k})$ is an intensity factor, which is proportional to the matrix element squared [135]. The Fermi function is written $f(\omega) = (e^{\omega/k_B T} + 1)^{-1}$ and $A(\vec{k},\omega)$ is the one-particle spectral function, which represents the probability of adding or removing a particle from the interacting many-body system. The spectral function is proportional to the imaginary part of the Green's function, which is defined by:

$$G(\vec{k},\omega) \;=\; \frac{1}{[\omega - \varepsilon_{\vec{k}} - \Sigma(\vec{k},\omega)]} \tag{4.24}$$

where $\varepsilon_{\vec{k}}$ is the "bare" dispersion and $\Sigma(\vec{k},\omega) = Re\Sigma(\vec{k},\omega) + iIm\Sigma(\vec{k},\omega)$ is the electron $self-energy$, which covers the effect of many-body interactions. Consequently, the one-electron spectral function is expressed as:

$$A(\vec{k},\omega) \;=\; -\frac{1}{\pi}\, ImG(\vec{k},\omega) \;=\; -\frac{1}{\pi}\, \frac{Im\Sigma(\vec{k},\omega)}{[\omega - \varepsilon_{\vec{k}} - Re\Sigma(\vec{k},\omega)]^2 + [Im\Sigma(\vec{k},\omega)]^2} \tag{4.25}$$

Two-dimensional multi-channel electron analyzers such as the one used in this work, measure the photoemitted intensity as a function of energy and momentum and offer the possibility of a direct visualization of the spectral function. The raw ARPES spectrum obtained from the detector has an energy scale corresponding to the kinetic energy of the photoelectrons. To transform the kinetic energy scale to binding energy ω, a reference spectrum is taken from a polycrystalline copper piece, which is in direct electrical and thermal contact with the sample. As a result, a well-defined Fermi step is obtained, which can be fitted by a $f(\omega)$ function. From such fit, the chemical potential μ is determined and the transformation to a binding energy scale is done by:

$$\omega(n) \;=\; E_{kin}(n) - \mu \tag{4.26}$$

where n represents a detector channel. After this process, the intensity $I(\vec{k},\omega)$ can be plotted in two manners. The first one consists to plot $I(\vec{k},\omega)$ as function of binding energy for a fixed momentum, which corresponds to an EDC analysis.

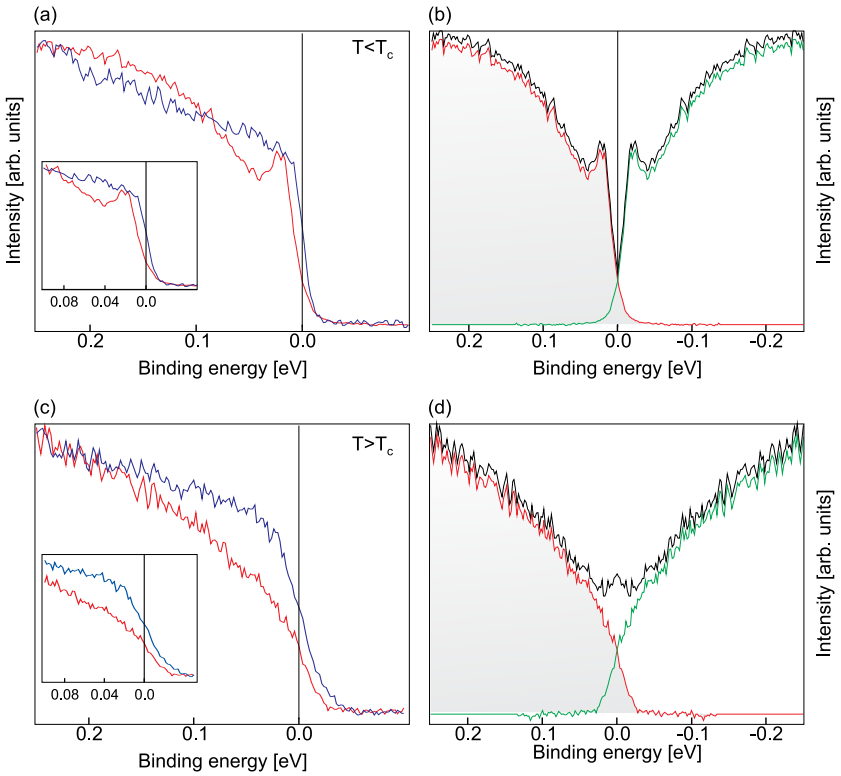

Figure 4.13: (a,c) EDC curves (red solid line) with the Cu reference spectra (dashed blue line) in electrical contact with the sample taken at T = 10 K and T = 90 K, respectively. The insets are a zoom around E_{F} to get a clear observation of the midpoint shift of the leading edge of the EDC relative to the Cu reference. The shift between the two curves indicates the presence of a spectral gap in (a) and its absence in (c). (b,d) Symmetrized EDC where the resulting curve of $I(\omega) + I(-\omega)$ is represented in solid black line. Note the closing of the spectral gap in (d) indicated by a single peak centered around E_{F}.

The second is an MDC study where $I(\vec{k},\omega)$ is plotted as function of $\vec{k}$ for a fixed ω. An EDC analysis is delicate since the spectral function has a strong ω dependence. This makes $A(\vec{k},\omega)$ non-lorentzian in ω and the EDC lineshape is asymmetric with a background that might change with the binding energy. Another complication is the influence of the Fermi function that eliminate the positive ω part of the spectral function, *i.e.* ARPES only probes occupied states. However, $f(\omega)$ can be compensated by using a method to "sum out"the Fermi distribution [136]. This is the EDC so-caled *symmetrization procedure*, which is commonly used for studying the gapped states of HTSC materials (SC and PSG states). Neglecting the matrix element effects, the symmetrized EDC intensity is as follows:

$$\begin{aligned} I_{sym}(\vec{k_F},\omega) &= I\left(\vec{k_F},\omega\right) + I'\left(\vec{k_F},-\omega\right) \\ &= I_0 A\left(\vec{k_F},\omega\right) f(\omega) + I_0 A'\left(\vec{k_F},-\omega\right) f'(-\omega) \end{aligned} \tag{4.27}$$

Considering the particle-hole symmetry, the spectral function $A'(\vec{k_{\mathrm{F}}}, -\omega) = A(\vec{k_{\mathrm{F}}}, \omega)$ and $f'(-\omega) = [1\text{-}f(\omega)]$. The symmetrized EDC intensity is then:

$$\begin{aligned} I_{sym}(\vec{k_F}, \omega) &= I_0 A\left(\vec{k_F}, \omega\right) f(\omega) + I_0 A\left(\vec{k_F}, \omega\right)[1 - f(\omega)] \\ &= I_0 A\left(\vec{k_F}, \omega\right) \end{aligned} \tag{4.28}$$

To confirm the validity of the symmetrization procedure in the study of SC/PSG gaps, a simple verification is presented. Figure 4.13(a,c) displays EDCs recorded on YBCO film (red solid line) below and above the critical temperature. The blue dashed line represents the Cu reference spectrum taken at the same temperature than the EDCs. The inset is a zoom around E_{F} to observe the midpoint shift of the leading-edge, which is commonly used to evaluate the existence of a gap. In Fig. 4.13(a), a clear midpoint shift is observed between the Cu spectrum and the EDC, which indicates the presence of a gap. On the contrary, Fig. 4.13(c), no shift is noticeable. Using the symmetrization procedure defined in equation (4.28), the opening/closing of the gap becomes even more obvious. Figure 4.13(b,d) display the symmetrized EDC shown in Fig. 4.13(a,c). The red and green curves are $I(\vec{k_F}, \omega)$ and $I(\vec{k_F}, -\omega)$, respectively, and the black solid line represents their sum, $\mathrm{I}_{sym}(\vec{k_F}, \omega)$. As deduced from Fig. 4.13(a,c), a clear gap is observed in Fig. 4.13(b) whereas Fig. 4.13(d) displays a small peak centered around E_F.

Analysis from MDC is simpler since it is assumed that the self energy is essentially independent of $\vec{k}$-momentum and thus, the MDC has a Lorentzian lineshape with a simple extrinsic background that can be subtracted. Further, its peak position gives the normalized dispersion, which is proportional to the imaginary part of the self-energy. The full-width half maximum (FWHM) of the MDCs is then related to the inverse mean free path and can be extracted as function of ω. Experimentally, one can fit MDCs with a Lorentzian function at each ω and extract the dispersion. Figure 4.14(a) shows a typical ARPES spectrum where the solid yellow line represents the Lorentzian fit of the MDC taken at the Fermi level. The blue dashed line in Fig. 4.14(a) represents the band dispersion deduced from MDC peak positions, which in turn are extracted from Lorentzian fits to the MDC's as a function of binding energy [see Fig. 4.14(b)]. By following the MDC peak positions as function of the binding energy, one can easily observe the evolution of the band dispersion and it is possible to make further analysis of its shape.

4.4.2 Main ARPES results on cuprates

Since the discovery of cuprate HTSC, ARPES experiments has become more than just a tool for chemical analysis and band mapping. Its improvement in angular

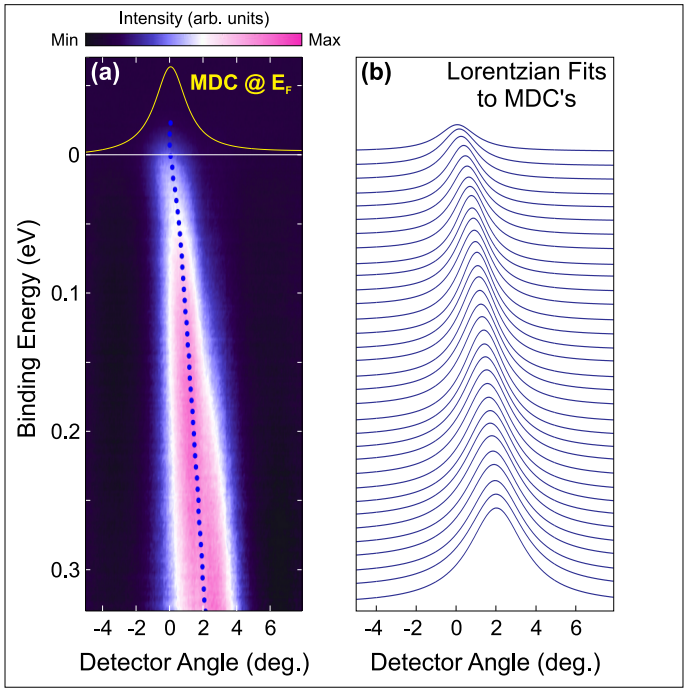

Figure 4.14: (a) ARPES intensity spectrum from an LSCO sample, where the yellow solid line represents the Lorentzian fit of the MDC taken at E_F. (b) Lorentzian fits of the MDCs as function of the binding energy. The blue dashed line in (a) represent the dispersion extracted from the MDCs.

and energy resolution as well as the remarkable progress in high-quality single crystal have been the key to turn this technique into a sophisticated many-body spectroscopy technique and have revealed/confirmed many physical aspects of the HTSC phase diagram. Due to its large orthorhombic unit cell (a = 5.42 Å, b = 5.38 Å and c = 30.72 Å) and its very low charge density between the two adjacent Bi-O planes, the Bi based cuprate family (BiSCO) is easy to cleave and yields a stable BiO surface. As a result, many early ARPES studies were performed on BiSCO compounds. However, general physical aspects such as the pseudogap or the symmetry of the SC gap, established for this compound have been verified in other cuprates and hence recognized as common features of HTSC materials. However, with the development of instrumental cleaving technique, ARPES studies on the lanthanum family, *e.g* LSCO, has became feasible and reproducible. Indeed, since LSCO is difficult to cleave because of its strong bonds, a special cleaving tool, the so-called "on-board sample cleaver", has been specially designed [137]. Cleaving LSCO single crystals with this device result in a close to atomically flat surface and thus, ARPES investigations on this material suddenly became significant [45, 138–141]. Further, also in LSCO the pseudogap and the symmetry of the superconducting gap, established for BiSCO compound was verified. In what follows, a brief summary of ARPES results on HTSC is presented. Some typical HTSC features found/confirmed by ARPES since the last two decades are

depicted and examples from different superconducting materials are given. However, characteristics only related to the compound itself have been neglected. For more extensive knowledge, additional information/details are available in the following references [134, 135, 142].

Fermi surface: One of the central advantage of ARPES is to give a direct access to the Fermi surface (FS) of materials. A FS corresponds to a reciprocal space intensity map (or k_F) obtained at the Fermi Level E_F. Information extract from the FS give topological details as well as low-energy properties of the sample. Figure 4.15 displays the FS of two HTSC materials. Figure 4.15(a) shows the FS representation in the normal state of strongly Pb-overdoped (OD) BiSCO[3] (Pb-Bi2212) sample [147]. As expected from conventional Landau Fermi liquid theory, the FS in the OD region consists of four large hole-pockets centered at (π, π), (-π, π), (π, -π), (-π, -π) and has been confirmed for other HTSC material [148]. However, it is evident that there are two FS pieces in Pb-Bi2212 (blue and red parts), which stems from the fact that there are two CuO_2 planes in the unit cell giving rise to the bonding and antibonding bands. The separation of this bands is named *bilayer splitting* and has also been found at optimal and slightly underdoped materials. The fact that this splitting was not detected in earlier ARPES experiments was due to the lack of momentum resolution and was taken as evidence for electronic confinement within the planes. The confirmation of its existence is a testament of technical improvement and has given important information about the HTSC electronic structure. Figure 4.15(b) represents the FS of underdoped (UD) $Ca_{2-x}Na_xCuO_2Cl_2$ (Na-CCOC) ($T_c = 13$ K) sample measured in the pseudogap state [149]. As for the OD side, large hole-barrels FS are expected. However, ARPES experiments shows that the FS is reduced to a small gapless portion centered around the nodal direction (0,0)-(π, π) line called *Fermi arcs*[4]. The Fermi arcs cannot be understood in terms of existing theories, although there is a solution in the form of conventional FS pockets associated with competing order, but with the back folding side that for detailed reasons is invisible [152]. However, recent ARPES experiments performed on Nd-doped LSCO [139], LSCO [141] and La-doped BiSCO [153] have revealed the coexistence of hole pockets around the nodal point. The qualitative observation of a hole pocket is compatible with many theories such as band structure calculations, which has shown that pockets can be formed in orthorhombic crystal structures [154]. Further, also models that invoke spin and charge separation of the electron quantum numbers [155, 156] or competing orders [80, 157, 158] predict a hole pocket in the pseudogap phase. Nevertheless, the existence of pockets around ($\pi/2$, $\pi/2$) remains controversial and has not yet been confirmed in other UD cuprates.

[3] Here, Bi2212 was not chosen as an example due to its complex FS involving the so-called *shadows* and *umklapp* bands [143, 144]. For the Pb-doped Bi2212 this superstructure is suppressed [145, 146].

[4] The original observation was made in the BiSCO compound [150, 151]

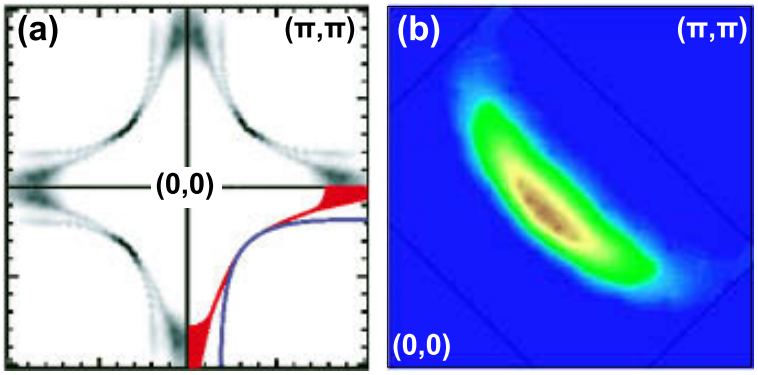

Figure 4.15: (a) Underlying Fermi surface of OD Pb-Bi2212 (T_c = 70 K) measured in the superconducting state at T = 20 K. The lower right quadrant of the Brillouin zone in panel identifies the bonding (blue) and the antibonding (red) bands. The two hole pockets centered around (π, π) is in agreement with conventional Fermi liquid theory [147]. (b) Underlying Fermi surface of underdoped UD Na-CCOC (T_c = 13 K) measure in the pseudogap state. The FS is reduced to a gapless region called *Fermi arc* centered around the (0,0)-(π, π) line [149].

Kink: In its most simple form, the ARPES manifestation of an electron's interaction with phonons, or any collective mode, corresponds to an abrupt change of the slope in the dispersion. Such feature is commonly known as the so-called low-energy *kink* [159, 160]. Given the fact that electron-phonon interaction is the mechanism for conventional superconductivity, its role in cuprates is very controversial due to the lack of evidence for lattice effects on the electron self-energy. Figure 4.16(a) shows the doping dependence of the dispersion for LSCO system taken along the (0,0)-(π, π) direction [161]. It is easy to see that the dispersion shows a sudden change near 70 meV, exactly where the in-plane oxygen bond stretching mode showed anomalous softening in neutron scattering experiments (indicated by the black arrow). The striking co-incidence between the anomalous electronic and phononic self-energy effects at the same energy makes a likely case for strong electron-phonon coupling. Further, it is interesting to point out that the slope of the dispersion along the nodal direction remains the same over a wide doping range (from the UD to the OD region), even where the sample is not superconducting. Since the MDC width is proportionally related to the scattering rate of electrons, by plotting the full width at half-maximum (FWHM) of the MDCs as function of the binding energy, one observes that at the same kink energy, an increase of the electron scattering rate occurs. Considering the dispersion at binding energies higher than the kink, the data show an increasing velocity with decreasing doping level. This is completely different from the Fermi liquid picture where the velocity beyond the phonon energy from the Fermi level (bare band velocity) is expected to be universal. Figure 4.16(b) displays the normalized ARPES intensity of LSCO (x = 0.17) recorded along the nodal direction where in addition

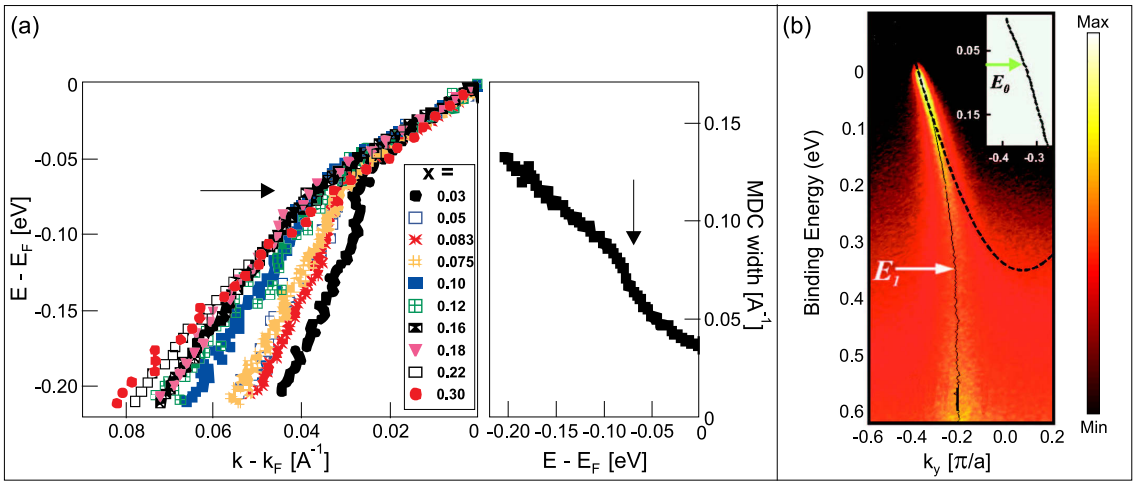

Figure 4.16: (a) Left panel shows the dispersion of LSCO from x = 0.03 to x = 0.30 measured at $T = 20$ K along the (0,0)-(π, π) nodal direction. A discontinuity in the slope of the quasiparticle dispersions, the so-called low-energy kink, is indicated by the black arrow. Right panel presents the scattering rate extracted from the full width at half-maximum (FWHM) MDC of LSCO (x = 0.063) at $T = 20$ K. The arrow indicates an increase of the scattering rate at an energy of about 70 meV [161]. (b) Plot of normalized ARPES intensity of LSCO (x = 0.17) at $T = 15$ K obtained along the nodal direction. The thin black line represents the MDC peak positions as function of binding energy and the dashed one is from a tight-binding fit of the band. In addition to the E_0 kink (green arrow shown in the inset with $E_0 \approx 70$ meV), a less intense vertical feature emerges below E_0 called the high-energy threshold E_1 (white arrow) [140].

to the low-energy kink around 70 meV, a less intense vertical feature emerge in the dispersion at higher energy (white arrow). This feature is commonly known as the high-energy threshold or waterfall [140]. Such a high-energy threshold E_1 was also observed in the BiSCO family of cuprates [162, 163] and consider to be a separation between coherent quasiparticle peaks at low energies from broad incoherent excitations at high energies. Moreover, the boundary between these low and high energy features exhibits a cosine-shaped momentum dependence, reminiscent of the superconducting d-wave gap. Such intriguing similarity between characteristics of the incoherent excitations and quasiparticle properties suggests a close correlation of the electronic response at high and low energies in HTSC.

Quasiparticle peak, superconducting gap and pseudogap: From ARPES point of view, two common features define the superconducting state. The first one is the sharp quasiparticle peak with the so-called *peak − dip − hump* feature appearing at (π, 0), which then evolves with $\vec{k}$ [46]. Figure 4.17(a) shows EDCs cuts recorded from OD Bi2212 [164] at two different locations in $\vec{k}$-space

as indicated in the top inset. The second feature is the *d*-wave symmetry of the superconducting gap. Below the superconducting transition $T < T_c$ (blue curves), the quasiparticle peak does not cross the Fermi level for cut A indicating the presence of the superconducting gap. However, for cut B along the nodal direction, no gap has been detected. The *d*-wave pairing leads to a strong momentum space anisotropy in the superconducting gap and dictates that the gap is zero along the (0,0)-(π, π) line (node) due to a sign change of the orbital pair wave-function. To estimate the gap value, the EDCs can be symmetrized. Figure 4.17(c) displays the symmetrized EDC of UD LSCO in the SC state ($T = 12$ K) [45]. Contrary to the nodal direction, a large open gap is visible at the antinode. Figure 4.17(b-d) shows the evolution of the superconducting gap as function of the FS angle for OD Bi2212[5] [165] and UD LSCO (blue filled circles) [45, 138], respectively. The maximum value of the gap is at the antinode (0, π) and decreases progressively until it vanishes at the node. Further, it has been observed that the maximum value of the gap changes as function of doping but still conserves its *d*-wave symmetry [65]. Above the superconducting transition $T > T_c$ for OD samples, the gap is closed and the sharp quasiparticle peak remains, as expected for a conventional metal. However, measurements for underdoped samples in the pseudogap state result in more unexpected properties.

The first observation is a loss of the quasiparticle peak when passing the transition temperature. Second, as mentioned before, a "destruction" of the FS where just a gapless region centered around the nodal point remains. Figure 4.17(e) presents two spectra of UD Nd-substituted LSCO (Nd-LSCO) [139] obtained closed to the antinodal and nodal point, respectively at $T > T_c$. Also shown are their corresponding EDCs at $\vec{k_F}$. The nodal EDC displays a small and sharp quasiparticle peak while the antinodal does not show any spectral weight around E_F. Moreover, it is clear that even above the SC transition, the gap remains open at the antinode. The loss of spectral weight and the opening of a gap is a typical behavior of the pseudogap state and has been observed in many cuprates [135]. When plotting the pseudogap value as function of FS angle [Fig. 4.17(d) (green open circles) and Fig. 4.17(f)], the *d*-wave gap symmetry is still present even though a small portion of the FS has zero gap. This behavior is clearly visible in Fig. 4.17(c) which displays the symmetrized EDCs for UD LSCO in the PSG state ($T = 49$ K). One of the remaining question is to understand if the pseudogap is a precursor [138] or a competitive order to superconductivity [42, 167]. ARPES experiments performed in the pseudogap state are controversial and until now, this question remains unresolved.

Another important issue is the existence of local inhomogeneity or nano-scale phase separation, which can take the form of one-dimensional *stripes* [168, 169]. Even though several attempts have been made to address these issues, the manifestation of these effects in ARPES are often quite subtle.

[5] The original observation was made by Wells *et al.* (1992) [166] and Shen *et al.* (1993) [164] and was later confirmed by Ding *et al.* (1996) [165].

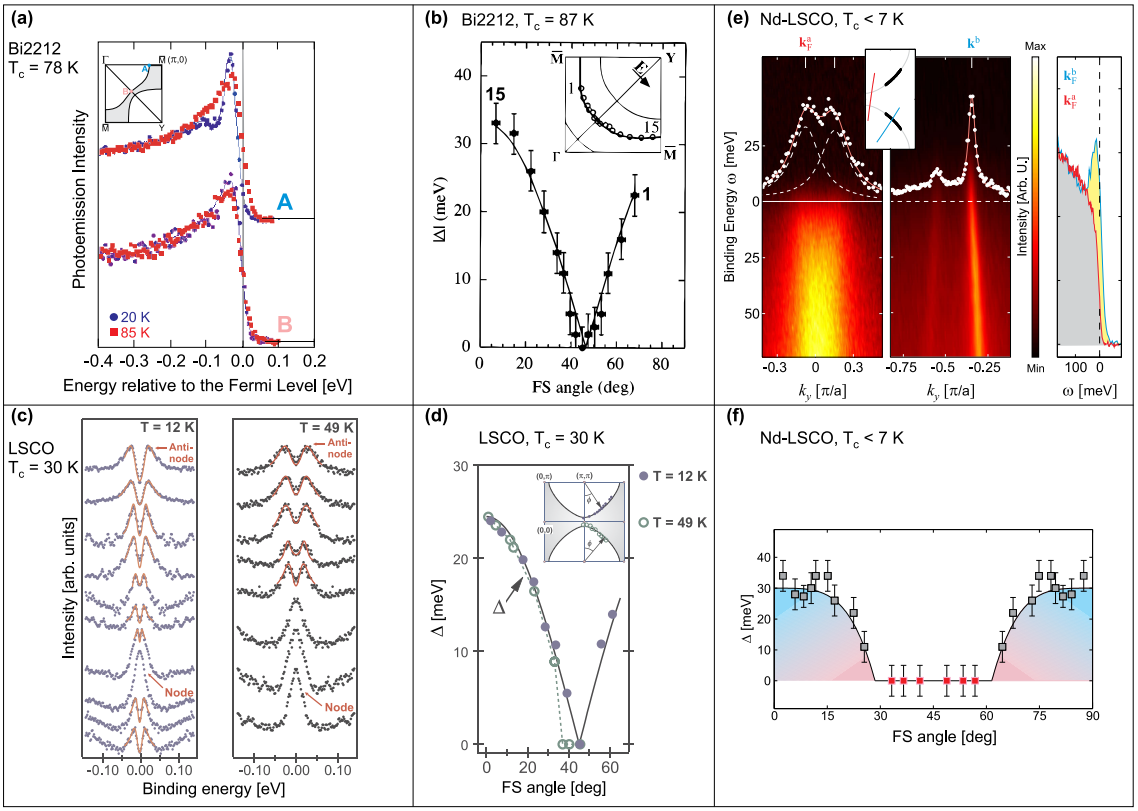

Figure 4.17: (a) Photoemission spectra from Bi2212 (T_c = 78 K) recorded at two locations in $\vec{k}$-space (A and B) as indicated by the inset. The shift of the quasiparticle peak from the Fermi level at T = 20 K designates the opening of a superconducting gap [164]. (b) Superconducting gap of Bi2212 (T_c = 87 K) as a function of Fermi surface angle (filled circles). The measurement was performed at T = 13 K and fitted by a d-wave gap function (solid black line). The inset shows the location of the corresponding spectra in the Y quadrant of the Brillouin zone as well as the photon polarization direction [165]. (c) Symmetrized spectra of UD LSCO (T_c = 30 K) for various k_F from the anti-node (top) to the node (bottom) at 12 K and 49 K, respectively. The solid red curves are fits. (d) Superconducting gap (filled circles) at 12 K and the pseudogap (open circles) at 49 K, as a function of the FS angle. The solid curve is the simple d-wave form. The upper right inset displays the FS at 12 K (filled circles) and at 49 K (open circles) [45]. (e) ARPES intensity spectra from Nd-LSCO (T_c < 7 K) measured in the pseudogap state at T = 15 K for two different positions in $\vec{k}$-space as indicated by the top inset (blue and red lines). The blue cut is taken along the so-called *arc* where no gap is detected and the red one close to the antinode where the gap remains open. (f) Pseudogap of Nd-LSCO (T_c < 7 K) as a function of the Fermi surface angle. The red and gray squares indicate the gapless and gapped regions of the FS, respectively. (For (e-f), Ref. [139]).

5 ARPES on $YBa_2Cu_3O_{7-\delta}$

$YBaCu_3O_{7-\delta}$ (YBCO/Y123) is one of the most studied compounds by other experimental techniques than ARPES. From ARPES point of view, although Y123 and BiSCO have similar T_c and both contain two CuO_2 planes, the lack of a natural cleavage plane makes Y123 much more difficult to investigate. Moreover, unlike BiSCO and LSCO, the existence of one-dimensional CuO chains along the b-axis contributing to the photoemission signal, makes the study complicated but also very exciting. Indeed, one of the main challenges is to understand the electronic interaction/hybridization between the chains and planes and to determine the role of the chains for superconductivity. Recent ARPES investigations on a very similar material, $YBa_2Cu_4O_8$ (Y1248), have led to interesting results [170–172]. The Y1248 crystal structure ($a \cong b \cong$ 3.9 Å and $c \cong$ 27.2 Å) also contains two CuO_2 planes per unit cell. However, in contrast to the related Y123 compound, Y1248 contains double CuO chains and is usually untwinned. The transition temperature is about $T_c = 80$ K and cannot be changed by simple variation of the oxygen content due to the very stable CuO double chains, which prevent oxygen loss. After cleaving, the Y1248 surface is stable, which makes this material more suitable for ARPES experiments even though, the cleaved surface will in most cases contain a mix of plane and chain termination. Figure 5.1(a) displays the intensity map at E_F measured at h$\nu = 105$ eV and Fig. 5.1(b) the FS of the AB (red filled circles) and B (blue filled circles) bands. Briefly, microprobe photoemission studies on Y1248 have revealed that the bilayer splitting of the CuO_2 planes is almost constant around the FS and that the electron scattering rate at the Fermi level is about 1.5 times stronger in the bonding band than in the antibonding band [170]. Moreover, a strong in-plane a-b asymmetry have been detected [171] where the antibonding band has a hole-like shape centered around (π, π) and an electron like shape centered around (0, 0). Another interesting feature in line with recent dynamical mean field theory (DMFT) calculations [173] is the observation of elongated pockets [Fig. 5.1(c,d)] along $\mathbf{k}_y$ in the 1D CuO FS [172]. This issue is very important since recent quantum oscillations experiments performed on both Y123 and Y1248 suggest the existence of very small Fermi pockets [30, 174]. Although the Y1248 compound is an intriguing material, the main subject of this thesis is to avoid the cleaving problem of Y123 and to obtain significant ARPES results. As already mentioned, the solution adopted in this work is to grow Y123 films and to transfer them *in situ* to the ARPES station. However, to the best of our knowledge, previous ARPES experiments on Y123 film were not successful

mainly due to the presence of an insulating surface layer [175]. In what follows, main ARPES results on Y123 single crystals from the last two decades are described. Then, the main advantage of studying Y123 films is exposed and finally, results obtained from these films are presented.

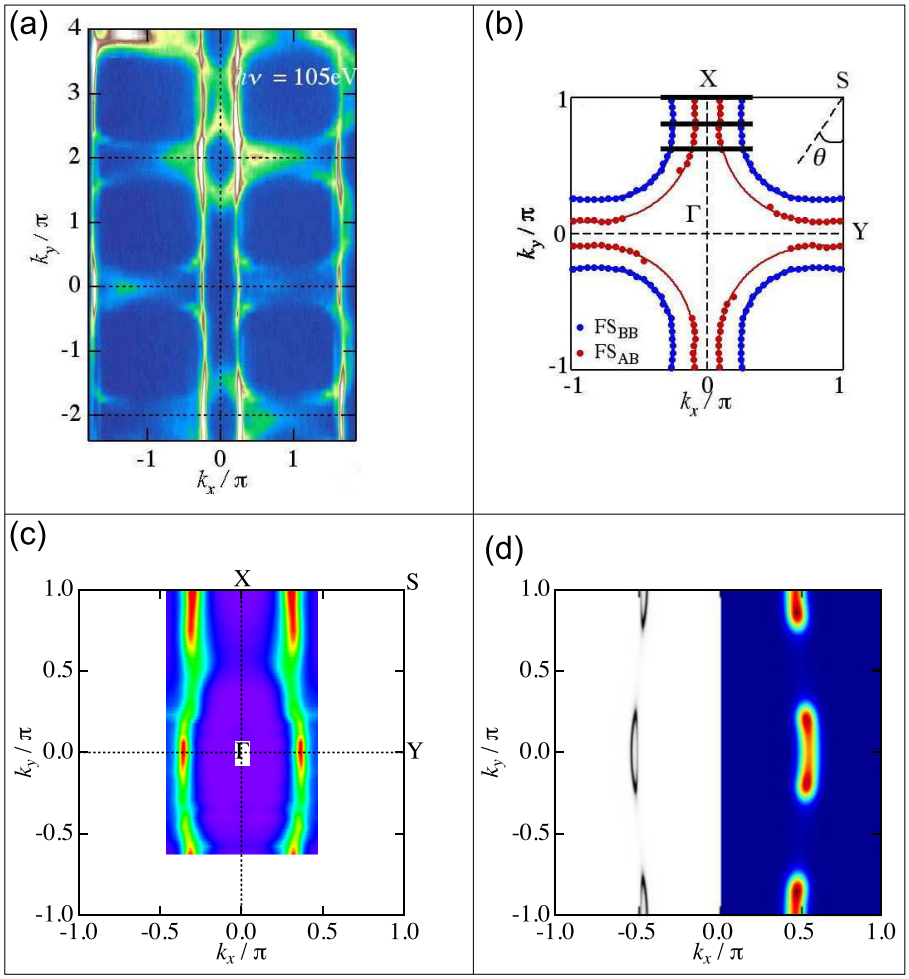

Figure 5.1: (a) ARPES intensity map of an Y1248 sample measured at the Fermi energy. (b) Fermi surface of the antibonding band (AB) and bonding band (BB) in the planes. θ represents the Fermi surface angle. Circles represent location of k_F obtained from MDC peak positions and solid lines are tight binding fits. (c) Measured Fermi surface determined by integrating the EDCs within $\pm$ 50 meV of E_F at T = 20 K with hν = 33 eV. (d) Calculated Fermi surface [173]: zero-energy spectral function $A(k, 0)$ at T = 0 K (left image) and expected ARPES intensity $I(k, 0)$ (right image).

5.1 Main ARPES results on YBCO single crystals

Compared to other compounds, relatively few photoemission experiments were performed on YBCO because of the lack of natural cleavage plane and that most of the crystals were twinned. Nonetheless, the study of these twinned crystals has provided very useful information. The first FS established on YBCO was presented by Campuzano *et al.* [176] on twinned optimally doped single crystals. The measured FS is a result of a superposition of two FS, one from the CuO_2 planes and one from the CuO chains. The 1D band corresponding to CuO chains appears twice in the FS and are rotated by 90° from each other due to twinning. Unlike the CuO chains, the twinning does not have a drastic effect on the large hole like pocket centered around (π, π) coming from the CuO_2 planes. Several measurements on twinned crystals have given a more complete study of

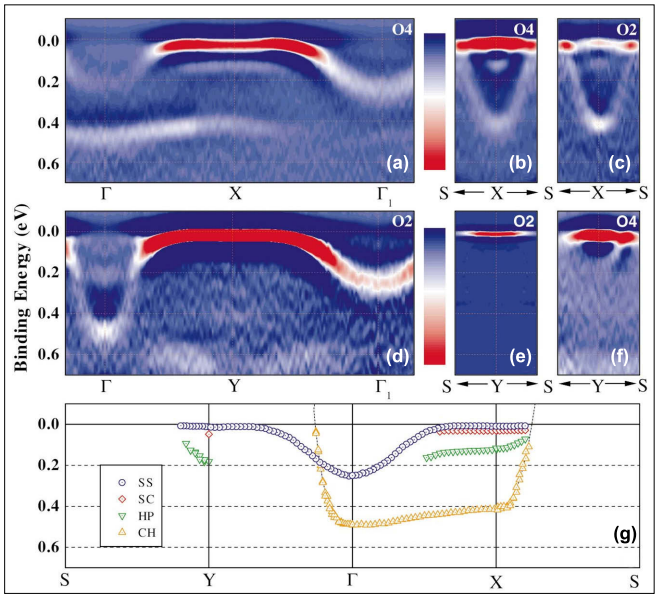

Figure 5.2: Electronic dispersion of overdoped YBCO (T_c = 89 K): (a)-(f) Second derivative with respect to the binding energy of the raw ARPES spectra from YBCO. (g) Summary of all the dispersive bands [177].

the FS [178] and have also revealed the presence of a narrow and intense surface-state peak located 10 meV below the Fermi level [179]. With the improvement of instrument resolution and sample quality, more detailed studies were carried out on untwinned YBCO samples. In addition to the surface-state peak, also the "peak-dip-hump" structure, the superconducting gap and the strong in-plane anisotropy were determined [177,180]. The presence of the CuO chains layers gives rise to an orthorhombic structure in YBCO [181], which, according to band calculations, results in a strong anisotropy of the CuO_2 planes [182]. Figure 5.2(a-f)

presents intensity plots of the second derivative of the ARPES spectra as function of binding energy. Four dispersive features can be identified and are summarized in Fig. 5.2(g): surface state (SS), superconducting peak (SC), hump (HP) and chain state (CH). After the study of Lu *et al.* in 2001, all ARPES investigations on YBCO compound stopped even if fundamental questions such as the origin of the surface-state or the existence of the bilayer splitting remained unsettled.

In 2006, Borisenko *et al.* revived the ARPES investigations on YBCO [183]. Their experiment were performed on high-quality detwinned YBCO single crystals with different hole concentration ranging from the underdoped to the overdoped region. To avoid the influence of surface-state effect reported in previous experi-

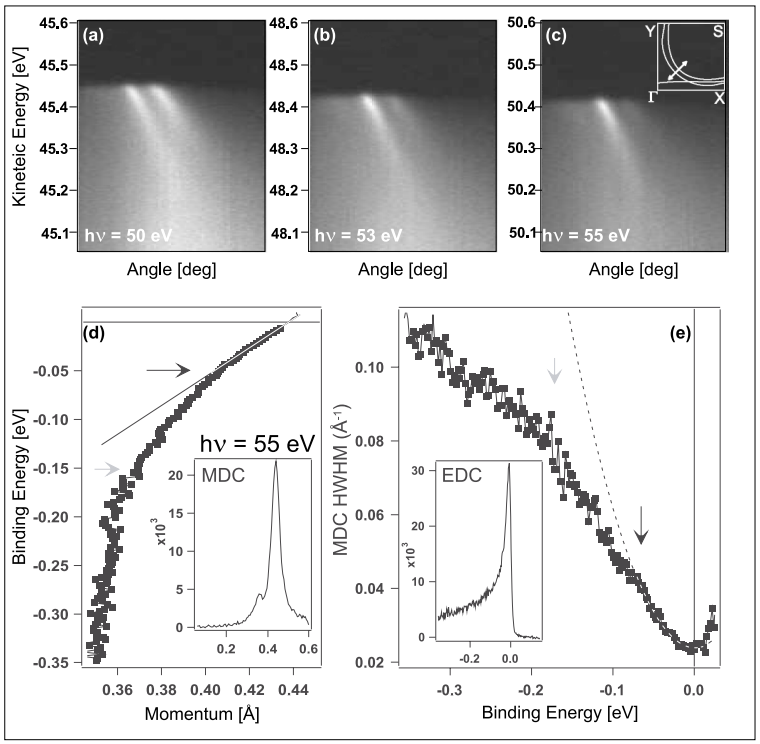

Figure 5.3: (a)-(c) Photoemission spectra of underdoped YBCO (T_c = 35 K) measured at T = 30 K along the nodal direction (top inset) as function of angle and kinetic energy. The spectra shows a clear bilayer splitting and depending of the photon energy, the intensity ratio between the bonding and antibonding bands fluctuates. Positions of the MDC's maxima (d) and their widths (e) as a function of binding energy. Dashed curves are fits to the low energy data. Black and gray arrows mark the energy positions of the low and high energy *kinks*, respectively. Insets show exemplary MDC and EDC [183].

ments [177, 179], the authors focused their attention in the nodal direction where a clear bilayer splitting is detected. They also demonstrated that the choice of

photon energy drastically influences the intensity ratio between the two bands. Figure 5.3(a-c) present ARPES spectra acquired along the nodal direction as indicated in the top inset. One can observes two features corresponding to the bonding (BB) and antibonding (AB) components, respectively. At hν = 50 eV, both BB and AB are clearly visible with an intensity ratio 1:1. By progressively changing the photon energy, the AB band becomes weaker leading to the dominance of the bonding band at hν = 55 eV. The significant intensity variation between the BB/AB bands when changing the photon energy was previously observed also in BiSCO and was attributed to matrix elements effects [184]. Another interesting characteristic in the nodal dispersion as already reported for other cuprates [140, 159, 161], are the so-called low and high energy kinks. Figure 5.3(d) shows the dispersion of the BB band extracted from the MDC's maxima as function of binding energy. Deviations in the dispersion are clearly visible around 50 mev and 150 mev. To confirm the presence of both features, Fig. 5.3(d) presents the half-width at half-maximum (HWHM) of the MDC's, which is directly proportional to the imaginary part of the self-energy. The presence of the two kinks is reproduced by the scattering rate but also the quadratic low energy behavior (dashed line), which clearly indicates the presence of quasiparticles [185]. Moreover, upon increasing the hole concentration, the low-energy kink shifts towards higher binding energy while the high-energy kink, on the contrary moves towards lower binding energy. As a result, for slightly overdoped YBCO sample, the two kinks seem to merge into one unique feature. Such kink dependence as function of doping is in agreement with other measurements performed on LSCO and BiSCO samples [186, 187].

Further investigations of the electronic properties on untwinned optimally doped samples were carried out in the following years. The FS measured by Zabolotnyy *et al.* [188] revealed an isotropic splitting of the BB and AB sheets with the expected 1D CuO chains running along the (0, π) direction in-between the two CuO_2 planes. However, although the sample was optimally doped, by calculating the surface area of the BB and AB FS sheets, the actual hole doping level of the CuO_2 planes were far above the superconducting dome and corresponded to a purely metallic region of the generic phase diagram. However, by changing the photon energy, it appeared that in addition to the metallic component, an extra non-dispersive flat band with a binding energy of 40 meV was also present [Fig. 5.4(a)]. This feature was associated with the superconducting state of the nominally doped bulk component since it disappeared above T_c and that a clear gap was observed below T_c. The total photoemission intensity was then broken down into two separate signals as shown in Fig. 5.4(b). The coexistence of metallicity and superconductivity in YBCO is explained by the absence of a natural cleavage plane. The most preferable cleavage bond is between the CuO chains and BaO planes [189, 190] leading to two terminations [Fig. 5.4(c)]. Since the CuO chain controls the doping level of the CuO_2 planes, cleaving YBCO results

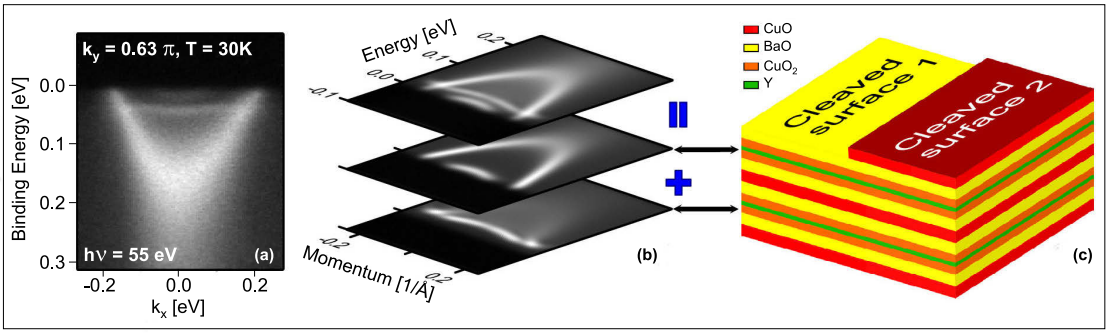

Figure 5.4: Coexistence of superconducting and metallic components when cleaving YBCO single crystals. (a) Experimental spectrum comprising the contribution from normal and superconducting states. (b) Simulation of the spectrum shown in (a) where the signal is split into two photoemission signals coming from the superconducting and overdoped (metallic) bilayer. The bottom most and middle images correspond to the superconducting and metallic phases, respectively. The topmost image is their sum, which agrees very well with the experimental spectrum (a). (c) Schematic structure of the cleaved crystal. The doping of the CuO_2 bilayer closest to the surface is modified due to the presence of both CuO chains and BaO layers, while the next bilayer remains unimpaired and retains superconductivity [188].

in a change of doping in the topmost bilayers. Further, since the cleaved surface is unstable, electronic reconstruction takes place in order to avoid the so-called "polar catastrophe" and thus, leads to an overdoped FS. Shortly after, the same observation and conclusion were made by an other group [191].

To avoid the problem of overdoped surface, Hossain *et al.* [192] proposed an alternative way by *in situ* evaporation of alkali metals, such as potassium (K) onto a cleaved surface. By absorbing K atoms, the self-hole-doping of the cleaved polar surfaces of YBCO is reduced since this process corresponds to doping the cleaved surface with electrons. The experiment was performed on twinned ortho-II $YBCO_{6.5}$, which displays the particular alternating filled and empty chains, as already mentioned in Chapter 2. The ortho-II phase have been in the center of attention since quantum oscillations experiments under magnetic field detected the existence of small Fermi surface pockets [30–34]. Moreover, due to the ordered oxygen vacancies within the chain layers, a folding of the CuO_2 planes is expected from band calculations [193–195]. Figure 5.5 shows the FS evolution of the ortho-II $YBCO_{6.5}$ as function of K evaporation. The as-cleaved FS [Fig. 5.5(a)] is constituted of four large hole pockets indicating an overdoped surface. When doping slightly the cleaved surface with electrons, the CuO chains running along both $(0,\pi)$ and $(\pi, 0)$ directions becomes more visible [Fig. 5.5(b)] and the area of the BB and AB FS sheets decreases. By doping the surface even more with

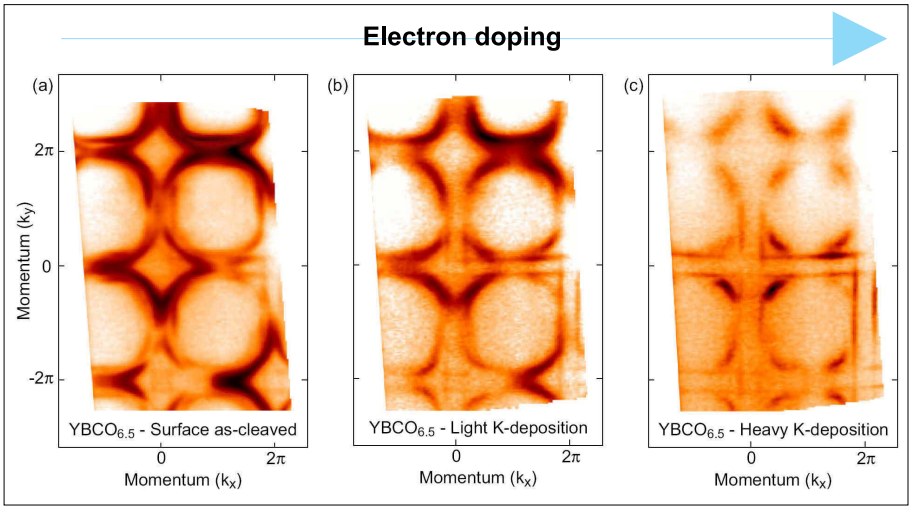

Figure 5.5: Ortho-II $YBCO_{6.5}$ Fermi surface evolution as function of electron doping. (a) ARPES Fermi surface of as-cleaved $YBCO_{6.5}$, exhibiting an overdoped FS with an effective hole doping $p = 0.28$ per planar Cu atom. (b)-(c) By evaporating potassium on the same cleaved surface, electrons are transferred to the topmost CuO_2 bilayer and the corresponding Fermi surfaces become progressively more underdoped. At heavy K-deposition (c), the ARPES intensity reduces to the 1D CuO-chain FS and four disconnected nodal CuO_2 Fermi arcs. The hole doping is estimated as $p = 0.11$ from the area of the chain FS [192].

electrons [Fig. 5.5(c)], the chain bands become clearer and the large FS sheets are reduced to simple arcs. The doping of the surface is estimated from the FS area of the chains and corresponds to a hole doping $p \approx 0.11$ meaning an oxygen content equal to $YBCO_{6.5}$. However, the pockets reported from quantum oscillations experiments were not found. Although the method of Hossain *et al.* gives the possibility of measuring an underdoped YBCO surface, the essential ordering of oxygen-vacancies was not fulfilled, which is most likely the reason why the predicted band folding was not detected.

To overcome this cleaving problem and to obtain a good control of the surface termination, another solution is adopted in this work: to grow YBCO films *in situ*. As explained in Chapter 3, to provide high-quality, *c*-axis oriented YBCO films, the PLD technique is the most suitable growing technique for HTSC materials. In addition, it gives the opportunity to gain control of surface termination (chain or plane), thickness, strain effects, (un-)twinning, and oxygen content. Depending of the film-substrate interface, the polar catastrophe of HTSC materials can be neutralized by electronic charge transfer through the interface [196]. This model has already been suggested for $LaAlO_3$ (LAO) films grown on $SrTiO_3$ (STO) (LAO/STO). Here, the alternation of charge layers causes a build-up of electric potential V_{elec}, which cannot be sustained [197, 198]. The polarity of the material

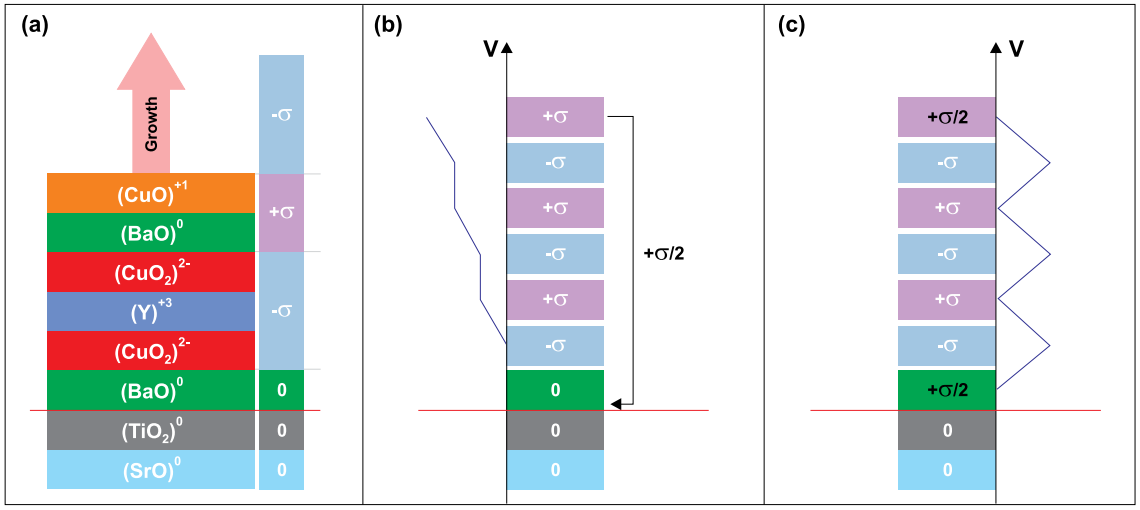

Figure 5.6: Schematic explaining how the polar surface of YBCO can be neutralized with the help of the substrate. (a) Stacking sequence for the deposition of YBCO on $SrTiO_3$ substrate when the first layer corresponds a BaO plane. The charge of each layer is also indicated. Considering two CuO_2 and the Y planes result in a negative charge of $-\sigma$ and $+\sigma$ for BaO and CuO chains layers. (b) From charge point of view, the growth can be considered as an alternation of positive and negative σ resulting in a divergent build-up potential V_{elec} and so, a polar surface. (c) To compensate this instability, electronic charges are transferred from the surface to the interface. The surface polarity is then canceled and the potential V_{elec} does not diverge.

is then canceled by charge transfer though the TiO_2 plane at the interface, by either oxygen doping or structural deformation. Since the YBCO films studied in this work are grown on TiO_2 terminated STO substrates and have a CuO chains surface termination, it implies a BaO/TiO_2 interface with a stacking sequence corresponding to Fig. 5.6(a). The layered structure of YBCO consists of alternating units having negative and positive charges, which means a divergent build-up of potential V_{elec} [Fig. 5.6(b)]. The surface polarity is canceled by transfer of charges from the YBCO layers into the TiO_2 bonds of the STO substrate. This is equivalent to the creation of oxygen vacancies. Further, to minimize its surface energy the oxygen vacancies in YBCO are driven to order themselves to the most stable configuration. Consequently, the potential V_{elec} does not diverge and the charges transfer from the surface to the interface result in a natural reduction of holes in the topmost CuO_2 layer [Fig. 5.6(c)].

To summarize, ARPES studied on YBCO compound is not an easy task essentially due to its polar surface. The approach adopted by Hossain *et al.* is promising but have some limits from an experimental point of view. For example, after evaporation of K atoms onto the cleaved surface, the sample cannot be warmed

up without losing K and thus, studies such as the evolution of the superconducting gap as function of temperature, cannot be performed. The film growth presents a real advantage since, once grown, the sample is stable and can be measured under different experimental conditions. In the next section, ARPES results on *in situ* grown YBCO films are presented.

5.2 Results on YBCO films

5.2.1 Antinode, off-node and node

By a direct *in situ* transfer between the PLD and ARPES UHV chambers, we have been able to measure YBCO films *as grown* (without cleaving). Figure 5.7(a,e,i) show typical ARPES spectra acquired at the antinodal, off-nodal and nodal points which are indicated by cut ①, ② and ③ [Fig. 5.7(h)], respectively. All the spectra were obtained at $T = 10$ K using a photon-energy $h\nu = 70$ eV to maximize their intensity.

Antinodal cut ①: Figure 5.7(a) shows the antinodal spectrum where two strong dispersive features are clearly observable. Between these two bands, a weak dispersion is also distinguishable. Figure 5.7(d) shows the first derivative of the antinodal spectrum. Two dispersive parabolic bands are clearly visible having their bottom around 300 and 10 meV, respectively. In analogy with another bilayer compound (Bi2212) and from previous ARPES experiments on YBCO single crystals, one can find the typical parabolic-like behavior of the plane derived bonding and antibonding bands. In Fig. 5.7(a) it is possible to observe four supplementary weaker bands that were not present in previous ARPES measurements. From the appearance it seems like the supplementary bands are created by a folding of the main bands. This would be coherent with the extra lines/points in our RHEED/LEED pattern shown in Chapter 3, that point towards an unit-cell doubling. Figure 5.7(b) shows the momentum distribution curve (MDC) obtained at the Fermi level (E_F). The MDC is composed of six peaks corresponding of the BB/AB bands and the folded bands. The six peaks are fitted by Lorentzians represented by the red dashed curves and blue solid line. Figure 5.7(c) represents the energy distribution curve (EDC) acquired at the Fermi wavevector ($\mathbf{k}_F$), i.e. maximum of the MDC at E_F), where no sharp quasiparticle peaks (QP) are observable. However, taking into account the leading edge of both EDCs, one can suspect the presence of a superconducting gap, which would be coherent since the measurement were performed at $T < T_c$. Details on the superconducting gap will be presented in section 5.2.3.

Off-nodal cut ②: Figure 5.7(e) shows the off-nodal spectrum and the corresponding cut is indicated in the FS [Fig. 5.7(h)]. Similar to the antinodal spec-

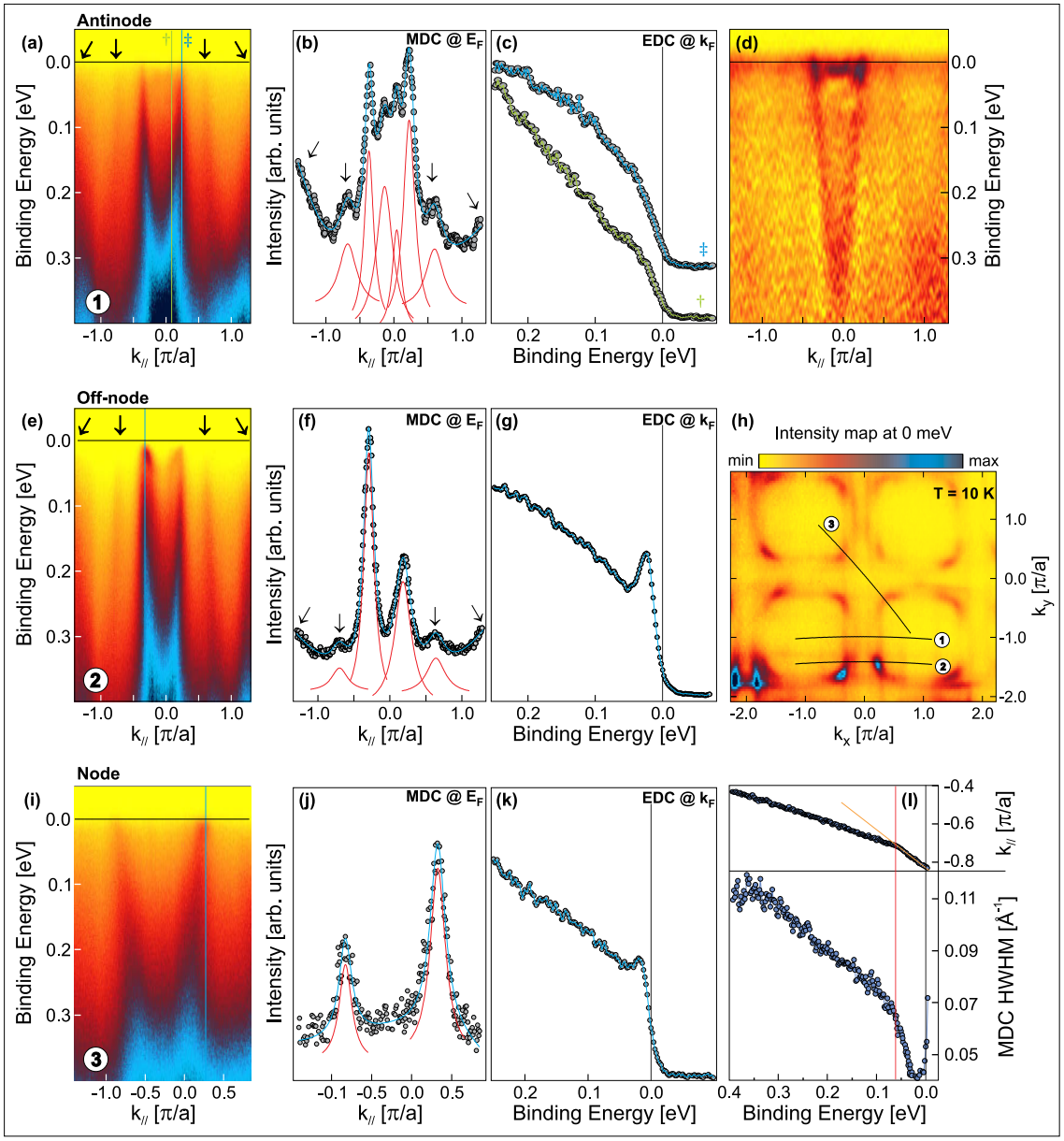

Figure 5.7: (a,e,i) ARPES spectra acquired at cut ①, ②, ③ in **k**-space as indicated by the lines in (h). (b,f,j) Momentum distribution curves (MDC) at the Fermi level (E_F) and a Lorentzian fit (solid blue and dashed red lines) corresponding to (a,e,i), respectively. (c,g,k) Energy distribution curves (EDC) at $\mathbf{k}_F$ and $T = 10$ K for the cuts indicated in the spectra (dashed blue and green lines) (a,e,i). (d) First derivative of the antinode spectrum in (a). Two dispersive bands can be observed having the bottom around 300 and 10 meV, respectively. (h) Near-Fermi level E_F, spectral intensity map acquired at a photon energy of 70 eV with energy integration of ARPES spectra over a ± 5 meV window about E_F. The black cuts represent the spectra shown in (a,e,i). (l) Position of the MDC's maxima (top) and their widths (bottom) as function of binding energy. Dashed orange curve shows the deviation of the dispersion and the solid red line the position of the low-energy kink $E_0 \approx 60$ meV.

trum, one can see four weaker features, which are even more clear in the MDC at E_F and fitted with four Lorentzians (red dashed curves and blue solid line in Fig. 5.7(f). Contrary to the antinodal spectrum, the EDC displays a sharp QP peak [Fig. 5.7(g)]. Such peak only appears in the superconducting state and is associated with the establishment of superconducting phase coherence. Moreover, considering the off-nodal spectrum [Fig. 5.7(e)], one can clearly observe that the bands do not cross the Fermi level, which indicates the presence of a superconducting gap. The off-nodal cut is interesting since it is placed at the end of the so-called Fermi arc. This will be developed later when describing the temperature dependent measurements (section 5.2.4).

Nodal cut ③: Figure 5.7(i) shows the nodal spectrum where two dispersive features are clearly visible. In the nodal direction, previous ARPES experiments on single crystals reported a clear observation of the so-called bilayer splitting, which is not the case here. As mentioned before, the bilayer splitting is highly sensitive to the photon energy [183]. One can consider that the photon energy used in this work is not the most suitable one to study this effect. Figure 5.7(j,k) shows the MDC and EDC obtained at E_F and $\mathbf{k}_F$, respectively. Two sharp and single peaks are clearly distinguishable. The MDC peaks are fitted using a double Lorentzian function and by plotting the positions of the MDC's maxima as function of binding energy, the dispersion can be extracted [Fig. 5.7(l) top]. A clear deviation in the dispersion is observed corresponding to the presence of the so-called low-energy kink $E_0 \approx 60$ meV. To confirm the presence of E_0, the half-width at half-maximum (HWHM) of the MDC is plotted as function of the binding energy [Fig. 5.7(l) bottom]. Since the MDC width is directly proportional to the imaginary part of the self-energy (scattering-rate), a change is expected. From Figure 5.7(l), the kink energy $E_0 = 60$ meV and the quadratic low energy behavior is also observed (curvature at low binding energy), which clearly indicates the presence of quasiparticles [186]. Figure 5.7(k) shows an EDC acquired at $\mathbf{k}_F$, where a small and sharp QP peak is clearly visible.

By comparing the nodal and antinodal EDCs [Fig. 5.7(c) and (k)] with previous ARPES experiments [199, 200], one can presume that the surface of the current YBCO film is underdoped. Indeed, the small and sharp nodal QP peak and its absence at the antinode is considered a common feature for lightly hole-doped cuprates. This could be expected on YBCO films since creation of oxygen vacancies on the top-most layer is necessary to cancel the surface polarity. This results in an underdoped surface even through the bulk is optimally doped. Further support is found when comparing the value of E_0 [Fig. 5.7(l)] with previous data obtained from other HTSC families [159, 185], which also points toward an underdoped YBCO surface. To approximate the hole-concentration of the surface, one can assume the validity of the Luttinger theorem in the underdoped region of the phase diagram and estimate the hole number from the FS area [201, 202]. Other

estimations of the hole doping can also be deduced via T_c of the surface, *e.g.* by performing temperature dependent measurements of the off-nodal cut and observe at which temperature the SC gap closes. Further, the existence of a pseudogap would also be a strong argument for an underdoped scenario. These points will be developed in the following subsections (5.2.4 and 5.2.5).

5.2.2 Fermi surface and energy maps

By acquiring ARPES spectra for multiple momentum cuts, we have successfully mapped out the FS of the YBCO film. Figure 5.7(h) and the upper left corner of Fig. 5.8 show the FS measured at $h\nu = 70$ eV and integrated $\pm$ 5 meV around E_F. The FS clearly displays four hole-like barrels corresponding to the CuO_2 planes while the CuO chains are only noticeable in the third Brillouin zone (2π, -2π). In addition, centered around each barrels, slightly weaker pocket-like features (square) are visible. These can be directly connected to the folded bands seen in the antinodal/off-nodal spectra [Fig. 5.7(a,e)] and the unit cell doubling mentioned earlier (Chapter 3). To make things easier, the reconstruction is put aside in the initial discussion.

From local-density approximation (LDA) the expected YBCO FS is composed of three components corresponding of the one-dimensional CuO chains, and the bonding and antibonding CuO_2 plane bands [182, 203]. When looking at the FS of the YBCO film, it is obvious that the bilayer splitting reported in previous measurements [177, 183, 188, 191, 192] is missing. However, for optimally doped cuprates the existence of the bilayer splitting remains unclear [204]. In fact, from a recent ARPES experiment based on a wide doping range of YBCO single crystals, Fournier *et al.* [205] demonstrated that the bilayer splitting is progressively reduced upon underdoping. In fact, below $p \approx 0.15$, only the bonding CuO_2 band remains and the antibonding, detected in the overdoped regime, vanishes. The underdoped FS of YBCO is, hence, composed of CuO chains and square-like barrels bonding CuO_2 plane. In addition, the authors observed a clear loss of spectral weight of the nodal quasiparticle when going from the overdoped to underdoped regime, which confirmed prior results obtained on other cuprate families [199, 200]. Taking into account the weak presence of the bilayer splitting with the small or absence of spectral weight in the nodal and antinodal QP peaks, the surface of the present YBCO films should be underdoped. Finally, presuming the validity of the Fermi liquid theory in the underdoped region of the phase diagram, the surface hole doping (p_{surf}) extracted from the FS area $p_{surf} = 0.1 \pm 0.02$, which corresponds to an oxygen content $n = 7 - \delta \approx 6.5$, i.e. $YBCO_{6.5}$. Further support is also found when comparing the FS volume of the YBCO film with the one of Hossain *et al.* for a surface hole doping corresponding to $p \approx 0.1$ [192] [Fig. 5.5(c)].

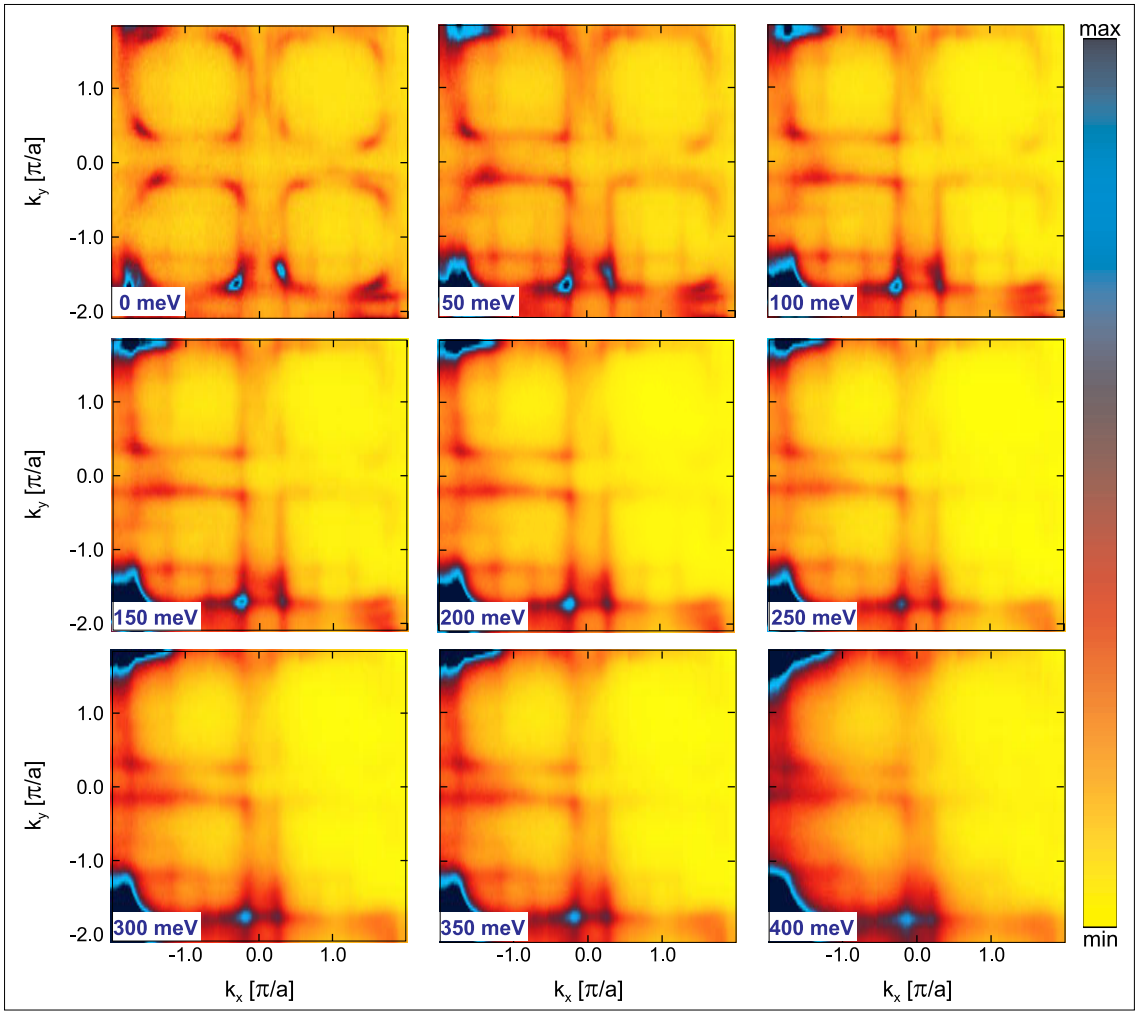

Figure 5.8: Spectral intensity maps of the YBCO film at different binding energies E_B. The maps are obtained by energy integration of ARPES spectra ± 5 meV around E_B. At higher energy, the band folding is more visible and the one-dimensional character of the FS becomes predominant.

Since the hole concentration of the YBCO film has been determined, let us now consider the extra bands centered around (π, π). Theoretically, a folding of the FS related to the CuO_2 planes has been suggested for the ortho-II ordered bulk phase of $YBCO_{6.5}$ [193–195]. Indeed, the highly ordered ortho-II phase, with an average hole doping $p \approx 0.1$ and $T_c \approx 60$ K, is characterized by a periodic alternation of filled and empty CuO chains along the *b*-axis. This causes an unit cell doubling along the *a* direction and a reduction of the Brillouin zone with a folding of the bands. For YBCO films, this scenario is plausible since the oxygen vacancies created to neutralize the polarity tend to order themselves to minimize its surface energy [24, 25]. In this respect, oxygen vacancy ordering within every second/alternating CuO chain would affect at least the top-most

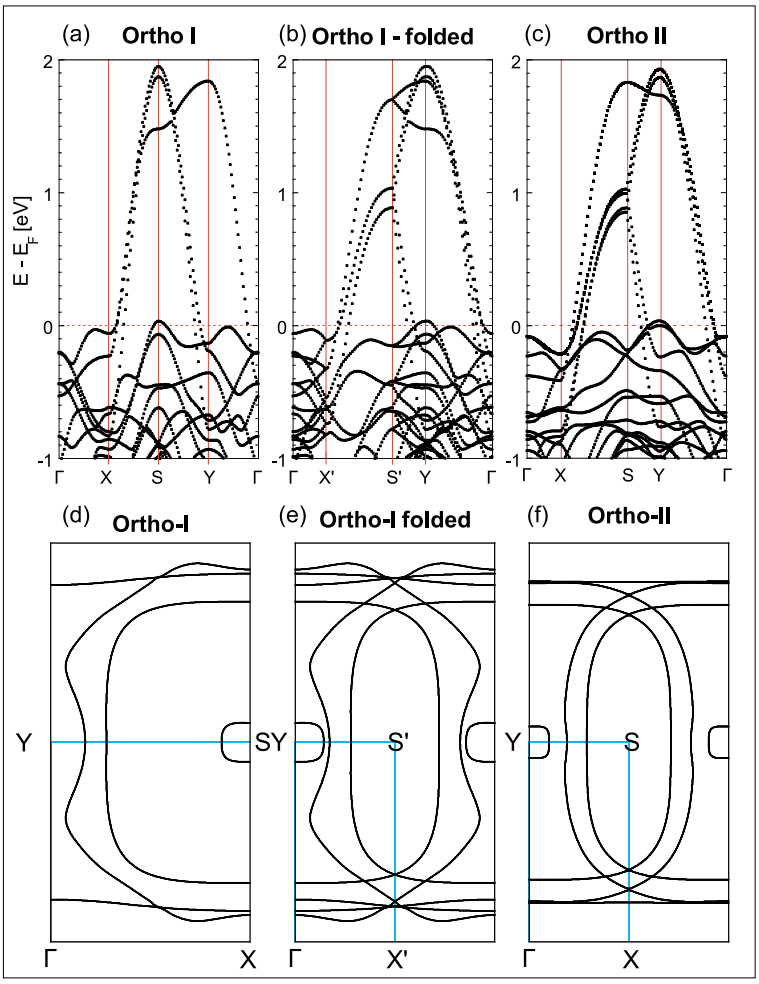

Figure 5.9: (a-c) Band structure of YBCO for the fully oxygenated Ortho-I, the folded Ortho-I and the Ortho-II. (d-f) Fermi surfaces corresponding to the band calculations (a-c). The FS were integrated around the Fermi level within an energy window of ± 20 meV. (Adapted from [194])

underlying CuO_2 plane resulting in a (2×1) surface reconstruction as indicated by RHEED/LEED (Chapter 3). Such an effect would be clearly discernible in surface sensitive measurement like ARPES, which has a probe-depth of approximately 5 Å at hν = 70 eV. Figure 5.8 shows the energy maps integrated around different binding energies E_B within a ± 5 meV window. The FS reconstruction, slightly visible at 0 mev, becomes even more pronounce when increasing E_B and the CuO_2 planes turns to be less 2D (square-like shape which looks more 1D). To consider the effect of the ortho-II order on the electronic structure as only a simple band folding along the *a*-axis, is a *highly* simplified picture. For instance, it has been shown by nuclear magnetic resonance (NMR) that the vacancy order causes a charge imbalance between the Cu atoms sitting below filled/empty chains [206]. Further, the 2*a* periodicity has a direct influence on the band structure [193, 194].

Figure 5.9(a) and (c) display the band calculation of the fully oxygenated YBCO ortho-I (filled chain) and the ortho-II, respectively. To compare both ortho-I and ortho-II, the ortho-I band calculation is folded in the reduced ortho-II BZ created by the unit cell doubling along the a-axis [Fig. 5.9(b)]. When evaluating Fig. 5.9(b) and (c), it is easy to notice that some of the features of the ortho-II are not reproduced. For instance, along the *Gamma-Y* line [Fig. 5.9(c)], the first band crossing E_F corresponds to the CuO chain following by the AB and B bands. By tracking the bands along the same Γ-Y line for the folded ortho-I [Fig. 5.9(b)], the bands crossing E_F corresponds to first the AB band, the double chain bands resulting from the folding and the B band. Moreover, the CuO chain seems more 1D in the ortho-II and has less dispersion compared to the ortho-I. Table 5.1 summarized the band crossing at E_F for Γ-Y, Y-S, S-X and Γ-X lines. Figure 5.9(d-f) shows the Fermi surface expected for the ortho-I, folded ortho-I and ortho-II, respectively. As seen for the ortho-I, the splitting of the bonding and antibonding band is clearly visible and due to the $2a$ periodicity, these two bands are further split into two in the folded ortho-I. In view of the FS obtained for the folded ortho-I [Fig. 5.9(e)] and the ortho-II [Fig. 5.9(f)], the dissimilarities are obvious. Nevertheless, one common feature can be noticed: the small hole pocket centered around the S point in the ortho-I which does not seem to be perturbed by the band folding. A simple shift to the Y point can be observed both in the folded ortho-I and ortho-II Fermi surfaces [Fig. 5.9(e,f)]. From the band calculation, this pocket should be due to a fairly flat CuO-BaO band arising mainly from hopping between the chain oxygen sites via the apical oxygen site in the BaO layer [182]. However, experimentally, no hole pocket centered around S has been reported.

Phase	Γ-Y	Y-S	S-X^*	Γ-X
Ortho-I	Ch	AB, B, P	P, B, Ch, AB	Ø
Ortho-I Folded	AB, Ch, Ch, B, P	P, AB, B	B, AB, Ch	Ø
Ortho-II	Ch, AB, B, P	P, AB, B	B, AB, Ch	Ø

Table 5.1: Bands crossing E_F for the ortho-I, folded ortho-I and ortho-II phases along the Γ-Y, Y-S, S-X and Γ-X lines [Fig. 5.9]. The bands are symbolized by Ch = chain, AB = antibonding, B = bonding and P = pocket arising from CuO-BaO bands centered around the S and Y points for the ortho-I and ortho-II, respectively. The Ø symbol means that no bands are crossing E_F and * is for the folded ortho-I where X-S is X'-S' in Fig. 5.9(b,e).

Let us now focus on the influence of the $2a$ periodicity of the ortho-II band folding. Bascones *et al.* theoretically demonstrated that for the ortho-II phase, the bonding (B) and antibonding (AB) bands of $YBCO_{6.5}$ are each split into two bands [193]: the intra- and inter- pair splitting, α and β, essentially due to the interlayer coherence and oxygen ordering. From LDA calculations, this results in

four planar bands appearing in two pairs with a **k**-dependency of the α and β bands. In addition, a quasi-1D character of the β bands is expected. Without the unit cell doubling and the ordered YBCO phase, these bands are normally degenerated and consequently neglected.

To describe the low-energy excitations in HTSC, a tight-binding model of the dispersion $\epsilon_{\mathbf{k}}$ is widely used. The planar dispersion is then defined by:

$$\begin{aligned} \epsilon(\mathbf{k}) &= -2t(\cos k_x + \cos k_y) + 4t' \cos k_x \ \cos k_y \\ &- 2t"(\cos 2k_x + \cos 2k_y) - \mu, \end{aligned} \tag{5.1}$$

where μ is the chemical potential, t is the nearest neighbor hopping integral, t' and $t"$ the second and third nearest-neighbor intraplane hopping integrals, respectively. However, the dispersion described in equation (5.1) does not take into account the unit cell doubling along the a-axis and thus, the band folding is not reproduced. In order to fit the FS of the YBCO films, the reduction of the Brillouin zone with the corresponding splitting of the bands and the ortho-II potential V induced by the alternation of filled and empty chains should be considered [193]. The ortho-II planar dispersion is characterized by:

$$\begin{aligned} \epsilon^{AB,B}_{\alpha,\beta}(\mathbf{k}) &= -2t\cos k_y - 2t"(\cos 2k_x + \cos 2k_y) \\ &- \mu \pm t_\perp(\mathbf{k}) \pm \left[4\cos^2 k_x (t - 2t'\cos k_y)^2 + \frac{V^2}{4}\right]^{\frac{1}{2}}, \end{aligned} \tag{5.2}$$

where $t_\perp$ is the interlayer hopping integral (bilayer splitting). The first and second plus/minus signs set the AB/B bands and the α/β bands, respectively. Here, V is set constant since in LDA calculations the ortho-II potential is only slightly **k**-dependent near the nodes. Further, $t_\perp$ is neglected ($t_\perp = 0$ meV) since the splitting of the planar B and AB bands cannot be distinguished in the data and since the existence of the bilayer splitting remains unclear for underdoped YBCO [205]. The hopping integrals t, t' and $t"$ are set free as fitting parameters. Considering equation (5.2) and above mentioned approximation, we fit the FS of the film and obtained the following parameters: t = 558 ± 0.05 meV, t'/t = 0.49 ± 0.03, $t"/t'$ = 0.5 ± 0.03, μ/t = -0.842 ± 0.09, and V = 75 meV.

Figure 5.10(a) shows the calculated FS of ortho-II sample considering the tight-binding parameters mentioned above. In the reduced Brillouin zone $k_x \in$(-π/2, π/2), $k_y \in$(-π, π), the ortho-II FS is composed of the 2D α bands with the 1D β band running along the k_x direction. The 2a periodicity induces a drastic change of the electronic structure resulting in a different FS. Considering that the film is twinned, the FS is folded along both (π/2, 0)-(π/2, π) as well as (0, π/2)-(π, π/2)

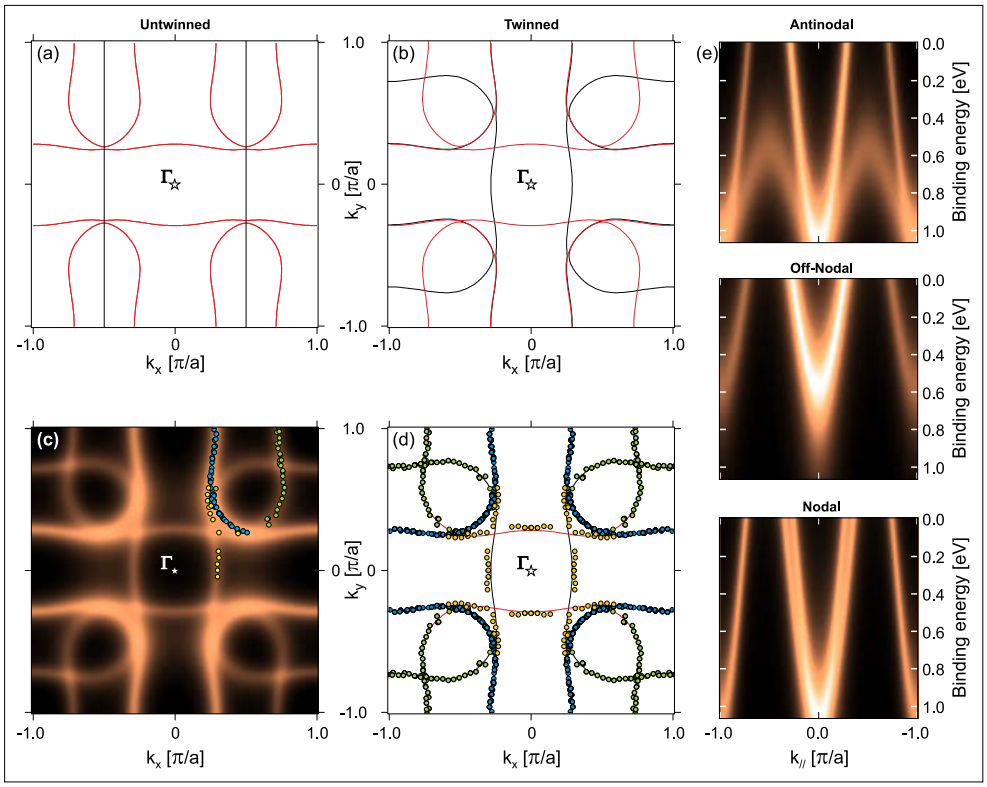

Figure 5.10: Tight-binding Fermi surface (FS) for ortho-II YBCO6.5 calculated using Eq. (5.2). (b) Same as (a) but after the addition of a second, 90° rotated, domain caused by the twinning (black lines). (c) Simulated spectral intensity map at E_F. The upper right quadrant shows the experimental data and the filled circles represent k_F as determined from a Lorenztian fits of the MDCs at E_F. (d) Overlay of experimentally determined k_F (filled circles) and calculated ortho-II FS from (b). (e) Simulated antinodal, off-nodal and nodal dispersions of the three cuts taken at the same location than in Fig. 5.7(h).

lines. Fig. 5.10(b) shows the calculated FS for a twinned ortho-II sample (black solid lines represent the twinned FS) and Fig. 5.10(c), the corresponding simulated intensity map at 0 meV with an energy broadening of 25 meV (experimental resolution). The upper-right quadrant represents the experimental data and the filled circles are extracted from a Lorenztian fits of the MDCs at E_F at different **k**-momenta. The simulated intensity map of the twinned ortho-II sample has been established using the fact that the intensity is proportional to the spectral function $[I(\mathbf{k},\omega) \propto A(\mathbf{k},\omega)]$ and for simplicity, the momentum dependence have been neglected. Figure 5.10(d) shows the symmetrized filled circles[1] with the calculated twinned FS. By overlaying the model onto the experimental data we see an excellent agreement at 0 meV but also at higher binding energy[2] [Fig. 5.11].

[1]The symmetrization of the filled circle have been done with respect to the crystal structure.
[2]From the experimental data, above E_B = 250 meV, the energy maps are broadened and the

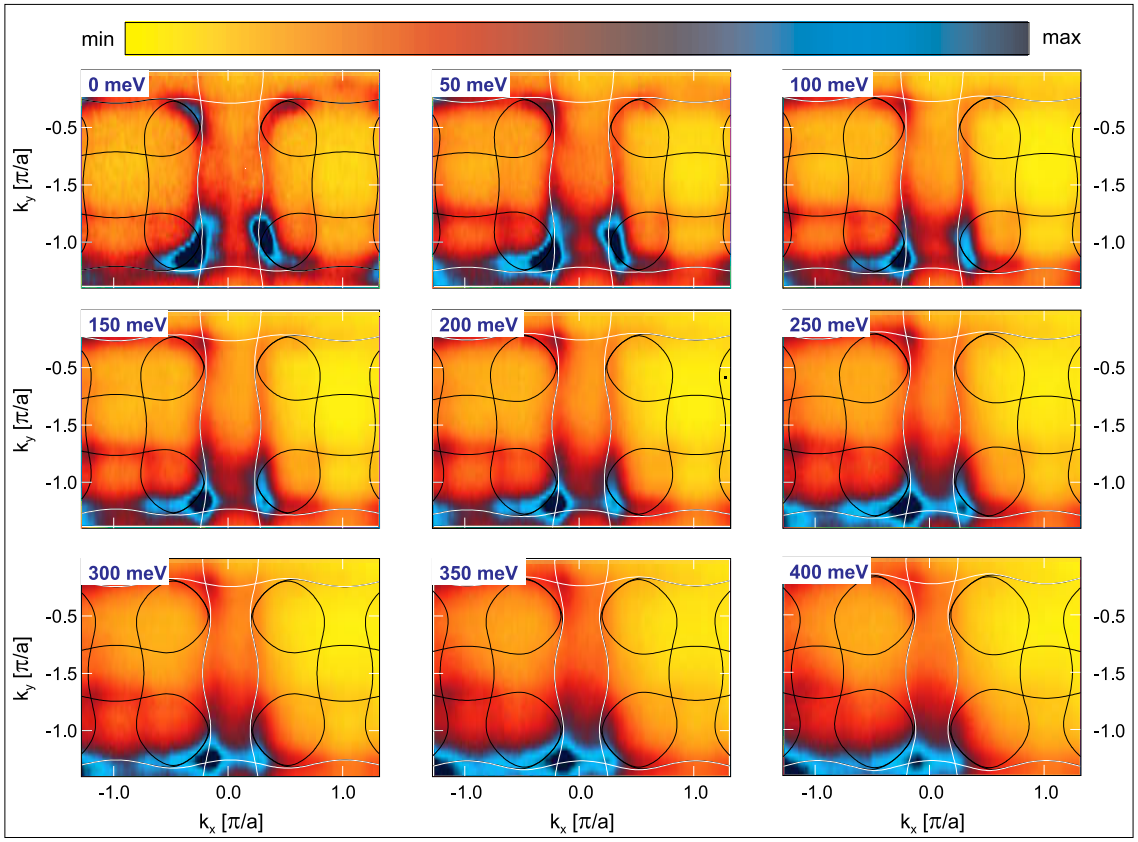

Figure 5.11: Tight-binding fit of the energy maps at different binding energy. The white and black lines represent the β and α bands, respectively.

However, it is important to specify that the tight-binding model used here does not take into account the 1D CuO chains. Considering the chain electronic structure, one could also expect a folding along the $(\pi/2, 0)$-$(\pi/2, \pi)$ line. But, since the dispersion of the chain-related bands are evidently along the b-direction (assuming no dispersion along a), a doubling along the a-direction will only fold the bands on top of themselves, rendering this effect invisible to ARPES measurement.

Compound	T_c [K]	t [eV]	t'/t	$t"/t'$	μ/t
Films YBCO	~ 65	0.558	0.49	0.5	-0.842
Single crystals ortho-II YBCO [193]	~ 60	0.36	0.4	0.5	-0.866

Table 5.2: Comparison of the tight-binding parameters of YBCO ortho-II films and single crystals.

reconstruction is difficult to distinguish. However, at high energy, the 1D feature is visible and the matching between this experimental feature and the calculated bands is considered.

To compare the hopping parameters with the literature, table (5.2) displays the tight-binding parameters derived from the YBCO film presented in this work and the calculated one for $YBCO_{6.5}$ ortho-II bulk phase [193]. Note that the T_c of the film is deduced from temperature dependent experiments done on a specific cut of the FS (see section 5.2.4). Since the surface of the film is underdoped, it is expected that T_c of $YBCO_{6.5}$ surface is lower that the one obtained for the bulk, which was determined from the resistivity measurement (Chapter 3). The t value extracted from the YBCO film is much larger than the one suggested for the ortho-II phase. This implies a large ratio t'/t, which is coherent with the square like FS shape [207, 208]. This large ratio of t'/t could be connected to structural effect due to a change of the Cu-O planar or the Cu-O apical distances [209, 210]. This effect cannot be excluded since it has been confirmed by RHEED/LEED that the YBCO surface of the film displays a clear (2×1) reconstruction. For $t"/t'$ and μ/t ratios, these values are in good agreement with the ortho-II phase but also similar to other cuprates [208, 210–212]. Moreover, considering the doping level measured in other YBCO single crystals [208], the hole concentration corresponding to the ratio μ/t is $p \approx 0.095$, which is consistent with the hole doping p_{surf} deduced from the FS area of the YBCO film.
Finally, to confirm that the hopping parameters extracted from the fitting are robust, we proceeded with a simple test by manually changing μ and t' alternatively. So, the ratio μ/t, t'/t and $t"/t'$ are fixed to other values and we observed how the bands evolve (see Appendix A). From this basic check, we clearly see that for other ratios, the calculated bands do not match the experimental data. Further, Appendix B also presents the simulated intensity maps as function of binding energy for parameters extracted from the YBCO film FS.

The main conclusion of the two last subsections is that since the YBCO films have an optimally doped bulk (p_{bulk}= 0.18 ± 0.004), the hole doping deduced from the Fermi surface area shows that the surface is indeed underdoped (p_{surf} = 0.1 ± 0.02) corresponding to an oxygen content of $n \approx 6.5$. By growing oxygen-ordered YBCO films by PLD, a clear surface representation of underdoped $YBCO_{6.5}$ ortho-II band folding is made evident by ARPES. The results hereby undoubtedly confirm theoretical expectations [193–195]. This can be connected to the (2×1) surface reconstruction caused by ordered oxygen vacancies that help to stabilize the YBCO surface. This clearly highlights the importance of having not only the correct carrier-concentration, but also a very well ordered and clean surface to facilitate ARPES data representative of the compound's true nature. Further, the position of the low-energy E_0 kink, the small and sharp nodal quasiparticle peak and its absence at the antinode are in agreement with previous experiments performed on lightly hole doped cuprates [159, 185, 199, 200]. Finally, the weak presence of the bilayer splitting in our data can also be connected to the underdoped surface of the YBCO film, which supports recent observations [205].

5.2.3 Momentum dependence of the quasiparticle peak and superconducting order parameter

This section is devoted to study the detailed characteristics of the $YBCO_{6.5}$ ortho-II surface. An investigation of the superconducting state such as the evolution of the QP peak as a function of **k**-momentum and the nature of the superconducting gap is presented. All the data were recorded at a photon energy of $h\nu$ = 70 eV with circular polarized light. The sample was permanently in electrical and thermal contact with a polycrystalline copper sample holder used as reference and the experimental resolution was set to 15-18 meV. Figure 5.12(a) shows selected EDCs measured along the FS at different k_F. The position of the EDCs in **k**-space is represented in Fig. 5.12(c) where the solid black line is the tight-binding fit of the intensity map at E_F integrated over a ± 5 meV window and φ corresponds to the Fermi surface angle with $\varphi = 0°$ for (0, -π). The nodal and antinodal cuts correspond to cuts ① and ⑧, respectively. At the antinode, the EDC shows a fairly weak coherence peak with high background level. When moving towards the nodal point, the coherence peak intensity evolves and gets sharp in width (EDC ③, ④, ⑤, ⑥, ⑦). However, in the vicinity of the (0, 0)-(π, π) line, the peak seems to be suppressed and broadened (EDCs ①, ②, ③). This evolution of the QP peak as function of **k**-momentum is atypical from prior observations. Generally,

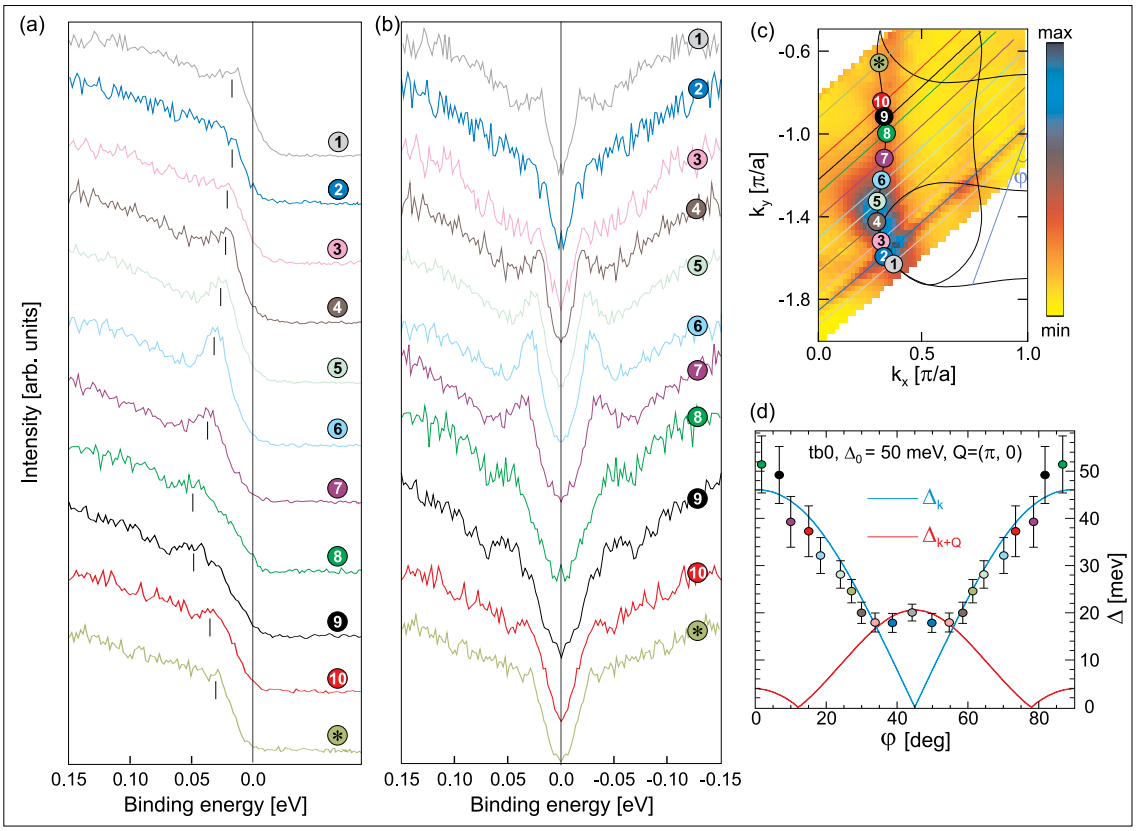

Figure 5.12: (a) Energy distribution curves acquired at different **k**-momentum and their symmetrization curves (b). (c) Location of the EDCs along the Fermi surface. (d) Gap profile as function of the Fermi surface angle φ. The solid blue and red curves represent the angular variation of the SC gap for a *d*-wave order parameter $\Delta_{\mathbf{k}}$ and for a SC gap taking into account the effect of the band folding $\Delta_{(\mathbf{k}+\mathbf{Q})}$, respectively.

in UD cuprates, the spectral weight has a maximum near the node and drops off rapidly when approaching the antinode where it is suppressed and finally vanishes, resulting in a broad line-shape with a weak shoulder near E_F [199, 213]. By investigating the exact **k**-momentum at which the QP emerges (cut ④ in Fig. 5.12(c)), it is noticeable that the increasing of the spectral weight does not coincide with the overlapping of the main and twinned folded bands. Indeed, cut ①, ② and ③ are placed exactly where the bands lie on top of each other and here, a much weaker QP is clearly observed. When moving away from the overlapping bands, the QP emerges and the evolution of the spectral weight behaves as expected for an UD sample that is decreasing of the QP spectral weight when moving towards the antinode and then increasing again towards the other nodal point (EDCs ⑨, ⑩, ✻).

Despite the unexpected evolution of the low-energy spectral weight along the FS, the QP peak maintains a distinct structure in momentum space, which gives the

possibility to determine the peak position. The black thick lines in Fig. 5.12(a) is a guide for the eyes indicating the location of the QP peak for each EDC. Starting from EDC ① to EDC ⑧, we easily see that the peak position tends to move towards higher binding energy indicating an opening of the SC gap with a maximum at the antinode. Then, when crossing the antinode, the peak position again moves closer to E_F, which corresponds a smaller gap (EDC ⑨ to EDC ✻). This clearly demonstrates an evolution of the gap magnitude as function of **k**-momentum, which agrees with an anisotropic gap. However, considering the nodal EDC ①, we can distinguish the presence of a gap, which is unexpected since by definition a node represents a point on the FS, where the gap is zero.
In order to evaluate the magnitude of the superconducting gap, the EDCs are symmetrized with respect to the Fermi level (procedure described in Chapter 4). Figure 5.12(b) displays the symmetrized EDCs where the evolution of the gap becomes even more obvious. Indeed, by extracting the energy position of the coherence peak in the symmetrized EDCs at k_F, the gap magnitude is evaluated. The maximum amplitude is detected at the antinode with $\Delta_{\text{Antinode}} = 52 \pm 4$ meV (EDC ⑧) and then, decreases progressively to reach a minimum value of Δ_{Node} = 20 ± 2 meV at the node (EDC ①). This evolution of the SC gap confirms the anisotropy and can be considered as a $d_{x^2-y^2}$-wave like gap symmetry even if a "nodeless" character is perceived. Figure 5.12(d) represents the gap magnitude as function of φ. The blue Δ_k and red Δ_{k+Q} curves[3] represent the angular variation of the SC gap Δ_k expected from a *d*-wave order parameter with a $[\cos(k_x) - \cos(k_y)]$ form around a conventional hole-like pocket. Considering the ortho-II band folding, the SC gap $\Delta_{(k+Q)}$ should be translated by a wavevector $Q = (\pi, 0)$. The colored circles correspond to the gap value extracted from each symmetrized EDC shown in Fig. 5.12(b) as function of φ. For commodity, all the cuts have been transposed into the (0, 0)-(π, -π) quadrant of the FS and then, symmetrized around $\varphi = 45°$. Within the error bars, the extracted gap magnitude follows quite well the simulated curves and the nodeless feature detected in the measurement is reproduced.
The nodeless behavior presented in this work can have several different origins. The most simple and obvious explanation would be the overlapping of bands around the (π, π) line. Due to the lack of resolution, the distinction between the main and twinned folded bands around this region is delicate and thus, it is not unlikely that we strayed onto the folding band when measuring the gap. Prior ARPES experiment on BiSCO reported a similar case. Here, early measurements on Bi2212 revealed a gap along the (π, π) line [68,69,214], which was later demonstrated to be an artifact created by the superlattice band [165]. The main and superlattice bands are very close around the nodal point and can be distinguished experimentally, resulting in a finite gap along the (π, π) line. However, recent

[3]The simulation shown in Fig. 5.12(d) (blue and red curves) was done by Dr. Michael R. Norman.

laser ARPES experiment[4] on optimally doped untwinned YBCO single crystal reported the existence of a gap along the (π, π) line direction and a similar behavior of the QP peak along the FS [215]. In this measurement, no FS reconstruction was detected and the authors attributed the nodeless feature to a $d + is$-wave parameter, which implies a time reversal symmetry broken state [61, 216].
Another possible effect that can create a nodeless behavior in both YBCO film and single crystal, is a significant microscopic roughness of the surface arising from the thickness of the film (Chapter 3) or cleavage. Such roughness may disturb the conservation law of the photoelectron momentum at the zone boundary, resulting in an averaged gap value around the nodal point. However, this would also imply a broader off-nodal than the nodal peak, which is inconsistent with our data [Fig. 5.12(a), EDCs ③, ④, ⑤]. Another alternative is the presence of a pseudogap in under and optimally doped YBCO [217, 218] where recent studies insist that a hidden order phase, such as charge/spin density waves [219] or time reversal symmetry broken staggered current flux states [77, 220], coexists with the SC phase below T^*. The nodeless behavior could then be associated with the pseudogap phase where a novel unconventional state is realized. However, this connection cannot be clarified at present time and supplementary experimental and theoretical studies are necessary.
An interesting factor, which is usually not taken into account, is the three-dimensional (3D) electronic structure of YBCO that can play a relevant issue when considering an electron pairing along the k_z direction. From (110) oriented YBCO film, planar tunneling conductance have revealed spontaneous surface-induced broken time-reversal symmetry, implying an s-wave contribution to the gap symmetry [221]. Moreover, muon spin rotation (μ^+SR) studies have also put forward the possible existence of an s-wave component along the c-axis [222]. At current time, to the best of our knowledge, the $\mathbf{k}_z$-dependent superconducting component has not yet been detected and more development of experimental technique, *e.g* soft X-ray ARPES, is needed. Finally, an important difference between YBCO and other cuprates is the existence of the CuO chains structure, which could influence the gap symmetry. In this work, we clearly see that the order within the chains has a major influence on the CuO_2 planes and a degeneration of the order parameter due to the ortho-II band folding cannot be ruled out. In fact, it is likely that the presence of the $2a$ periodic potential breaks the four-fold rotational symmetry of the d-wave gap, which would create a shift of the nodal point. In this case, what is usually considered as the node in typical HTSC is not anymore valid. More theoretical and experimental investigations are evidently required.

[4] A laser ARPES experiment is considered to be more bulk sensitive. The typical photon energy is ∼7 eV resulting in an escape depth for the electron of ∼ 100 Å [121].

To summarize, the k-dependence of the superconducting gap was investigated for the $YBCO_{6.5}$ ortho-II surface. The maximum amplitude of the gap is found at the antinodal point ($\Delta_{\text{Antinode}} = 52 \pm 4$ meV) and then decreases progressively to reach its minimum value at the node ($\Delta_{node} = 20 \pm 2$ meV). The momentum dependence of the superconducting gap obtained for the ortho-II surface is in line with an anisotropic gap. However, the origin of a nodeless feature is unclear even though the breaking of the rotation symmetry of the d-wave gap due to the presence of the $2a$ periodic potential and the overlapping of the bands around the node seem the two most reasonable scenarios. More precise measurements with better resolution should be carried out to make any definite conclusion about the origin/presence of a gap along the (π, π) line.

5.2.4 Temperature dependence of the Superconducting gap

In this section, we focus on the evolution of the superconducting gap as function of temperature. Three cuts corresponding to the off-node, antinode and node have been selected (same cuts as in Fig. 5.7). The measurement was performed with hν = 70 eV and circular polarized light. The sample was permanently in electrical and thermal contact with a polycrystalline copper sample holder used as reference. For each temperature, a copper spectrum was acquired before and after the YBCO data to determine the chemical potential and to check any drifts in the photon energy. For convenience, the measurement was performed on cooling. However, to ensure the validity of the experiment, for some temperature the data were re-checked by warming up the sample again. No noticeable differences were detected, and the data were hence considered reproducible.

Figure 5.13(a) displays the off-nodal spectrum measured at T =10 K. The black dashed line represents the position of the EDC shown in Fig. 5.13(b) taken at $\mathbf{k}_F$. Starting from $T = 90$ K and decreasing progressively the temperature to $T = 10$ K, one can clearly see the emergence of a QP peak. At high temperature T = 90-60 K, a fairly weak coherence peak is observed. Below T = 60 K, the spectral weight of the QP peak evolves and gradually becomes sharper as the temperature decreases. The progressive loss of coherence QP peak with increasing temperature is a common feature in underdoped cuprates associated with the temperature transition between the superconducting and pseudogap states[5]. Further, when

[5]The increase of temperature also plays an important factor in the broadening of the QP peak and can not be negligible since I($\mathbf{k}$,ω) $\propto$ f(ω)A($\mathbf{k}$,ω), where f is the Fermi function and A the spectral function.

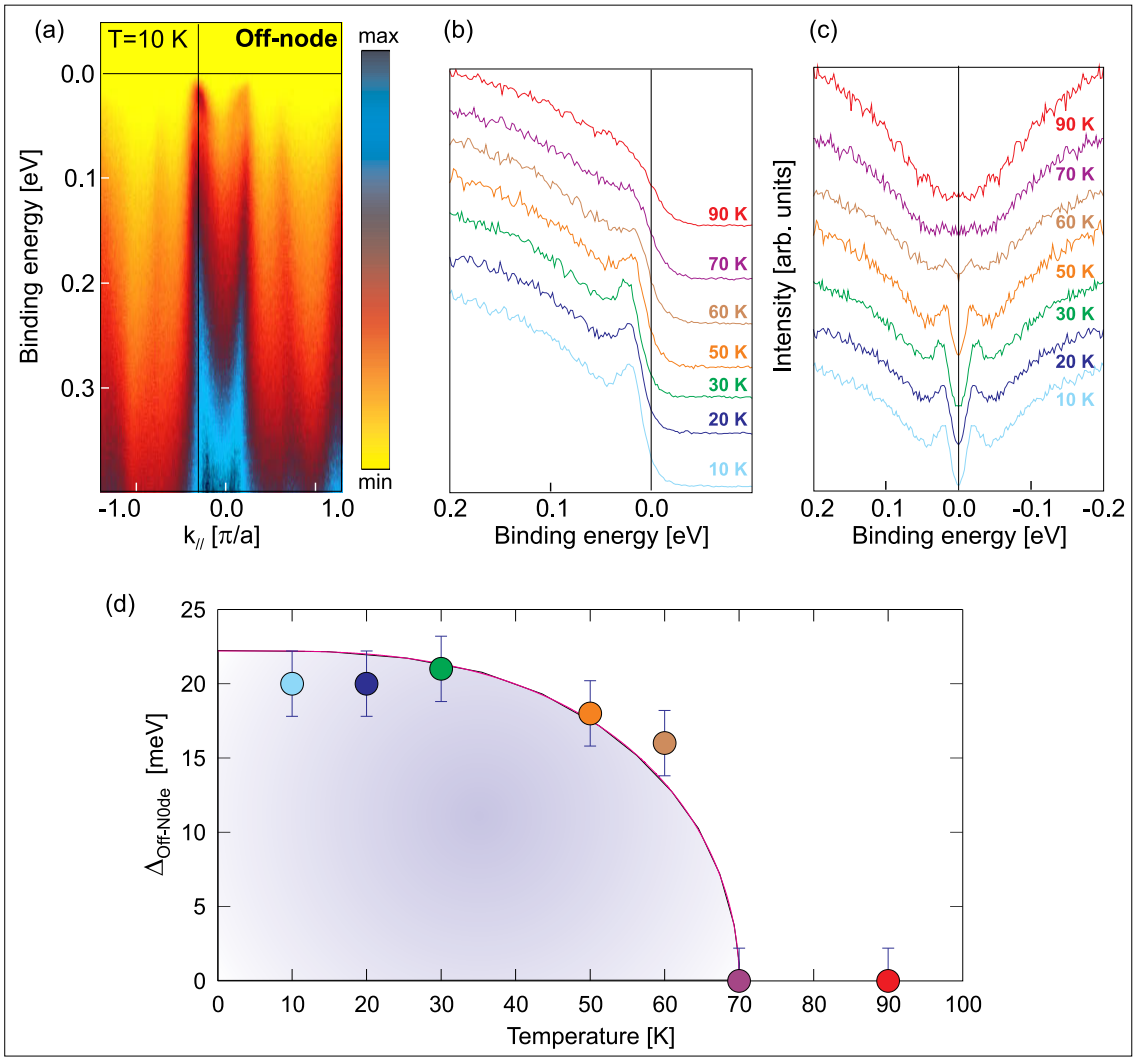

Figure 5.13: (a) Off-node spectrum corresponding to a Fermi surface angle $\varphi = 32°$. (b) EDC's obtained at $\mathbf{k}_F$ as function of the temperature. (c) Symmetrized EDC's to estimated the gap size. At $T = 70$ K the gap is closed indicating that the T_c of the surface is underdoped compared to the bulk. (d) Magnitude of the off-nodal gap $\Delta_{\mathrm{off-Node}}$ as function of the temperature.

taking into account the position of the QP peak, it is noticeable that the EDC peak approaches E_F when increasing the temperature, which suggests a closing of the superconducting gap. In order to estimate the gap value and to observe the evolution, all the EDC are symmetrized with respect to E_F. Figure 5.13(c) displays the symmetrized EDCs for T =10-90 K. For T =10-60 K a clear SC gap is observed, which decreases in amplitude when the temperature is increased. Indeed, for $T = 10$ K and $T = 60$ K the gap magnitude is estimated as $\Delta_{10K} = 22 \pm 3$ meV and $\Delta_{60K} = 16 \pm 2$ meV, respectively. At $T = 70$ K, the gap obviously disappears

indicating a critical temperature $T_c \approx 65$ K of the YBCO film surface. This is in good agreement with the hole doping deduced earlier from the FS area. To ensure that the gap is closing, a supplementary temperature above T_c ($T = 90$ K) is measured where no superconducting gap is detected. We can also see that the loss of spectral weight observed in Fig 5.13(b) is directly related to the closing of the SC gap. Figure 5.13(d) summarized the temperature dependence of the gap $\Delta_{\text{off-Node}}$. By extracting the amplitude of the gap from the symmetrized EDC [Fig. 5.13(c)], it is seen that $\Delta_{\text{off-Node}}$(T) decreases with T and vanishes when passing T_c. The thick magenta line is a fit of the data using a d-wave gap function defined by [223]:

$$\Delta_0(T) \quad = \quad \Delta_0(0) \cdot g(\bar{k}) \cdot tanh\left(\frac{\pi}{\beta}\sqrt{\alpha\left(\frac{T_c}{T}-1\right)}\right) \tag{5.3}$$

where $g(\bar{k})$ is a dimensional function of maximum unit amplitude describing the angular variation of the gap on the Fermi surface and α and β are constants that depend on the pairing state. For a two-dimensional d-wave, $g(\bar{k}) = cos(2\phi)$, with $\phi = 32°$ corresponding to the FS angle of the off-nodal cut, $\alpha = 4/3$ and $\beta = 2.14$ [224].

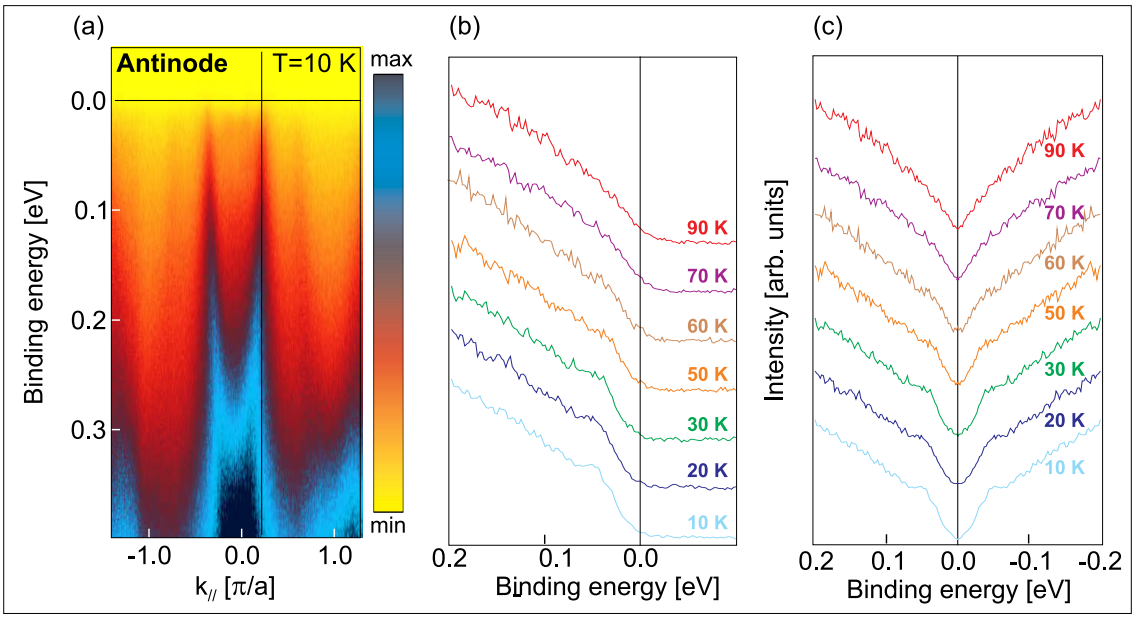

Figure 5.14: (a) Antinodal spectrum corresponding to a Fermi surface angle $\varphi = 0°$. (b) EDC's obtained at k_F as function of the temperature. (c) Symmetrized EDC's to estimated the gap size. The (pseudo-)gap remains open even at $T > 70$ K.

As for the off-nodal cut, the temperature dependence of the antinodal cut was also performed. Figure 5.14(a) displays the antinodal spectrum at $T = 10$ K.

The black line indicates the position of the EDC [Fig. 5.14(b)] acquired at the maximum of the MDC. As mentioned previously, the coherent QP peak is weak even in the superconducting state at low temperature (T = 10 K), which is a common feature of underdoped cuprates. When increasing the temperature, it is clear that the QP peak becomes broader and above T = 50 K, the coherent peak is lost making the localization of the EDC peak delicate. However, considering the position of the leading edge from E_F for each EDCs, no clear shift can be observed as function of temperature. To ensure this statement, the EDCs are symmetrized [Fig. 5.14(c)]. Contrary to the off-nodal symmetrized spectra, the gap magnitude does not seems to change ($\Delta_{\text{Antinode}} = 52 \pm 4$ meV) and does not vanish even at T = 90 K. As we demonstrated earlier, the surface of the YBCO film is underdoped, which implies the existence of a pseudogap state. The two principal characteristics of the pseudogap is the presence of a persistent gap above T_c around the antinodal region with a gapless region towards the node, *i.e.* Fermi arcs. The closing of the gap for the off-nodal cut, which is near the nodal point [Fig. 5.7(h)], and its perseverance for the antinodal one strongly suggest the presence of the pseudogap state. A detail study of the pseudogap state will be presented in the next section.

Figure 5.15(a) shows the nodal spectrum at T = 10 K with the black line indicating the position of the EDC acquired at $\mathbf{k}_F$ [Fig. 5.15(b)]. As for the off-nodal cut, one can clearly see the evolution of the coherent peak as function of temperature. When moving into the SC state ($T < 60$ K), a clear and sharp QP develops. Moreover, following the peak position of each EDC, it is obvious that the peak shifts towards E_F with increasing temperature, *i.e* closing of the gap along the (π, π) direction. To evaluate the magnitude of the gap, the EDCs are symmetrized [Fig. 5.15(c)]. Here, an unexpected feature can be observed: the gap detected at T = 10 K with $\Delta_{\text{Node}} = 18 \pm 2$ meV seems to vanish at T = 22 K. From T_c estimated from the off-nodal cut, one should expect the gap along the (π, π) line to disappear at the same temperature ($\sim$ 65 K) and not at a much lower temperature. To ensure the validity of the gap and its closing along the nodal direction, this measurement was verified in three different YBCO films, at two different nodal points, as well as on both heating and cooling. All samples displayed the same behavior. Fig. 5.15(d) shows the variation of the gap magnitude as function of temperature. The magenta line is a fit of the data using equation (5.3). From this plot, it is evident that the gap amplitude decreases from T = 10 K to T = 15 K and then vanishes at T = 22 K, showing a clear evolution of the gap. The discrepancy in T_c between the nodal and off-nodal cuts could possibly be connected to a lack of experimental resolution. Indeed, if the gap along the nodal direction becomes too small and the resolution too broad with the temperature, we will see a closed gap even though it is still open. This possibility should be considered when observing the evolution of the coherent QP peak of the EDC as function of temperature. Here, we notice that the spectral weight is still persistent even above

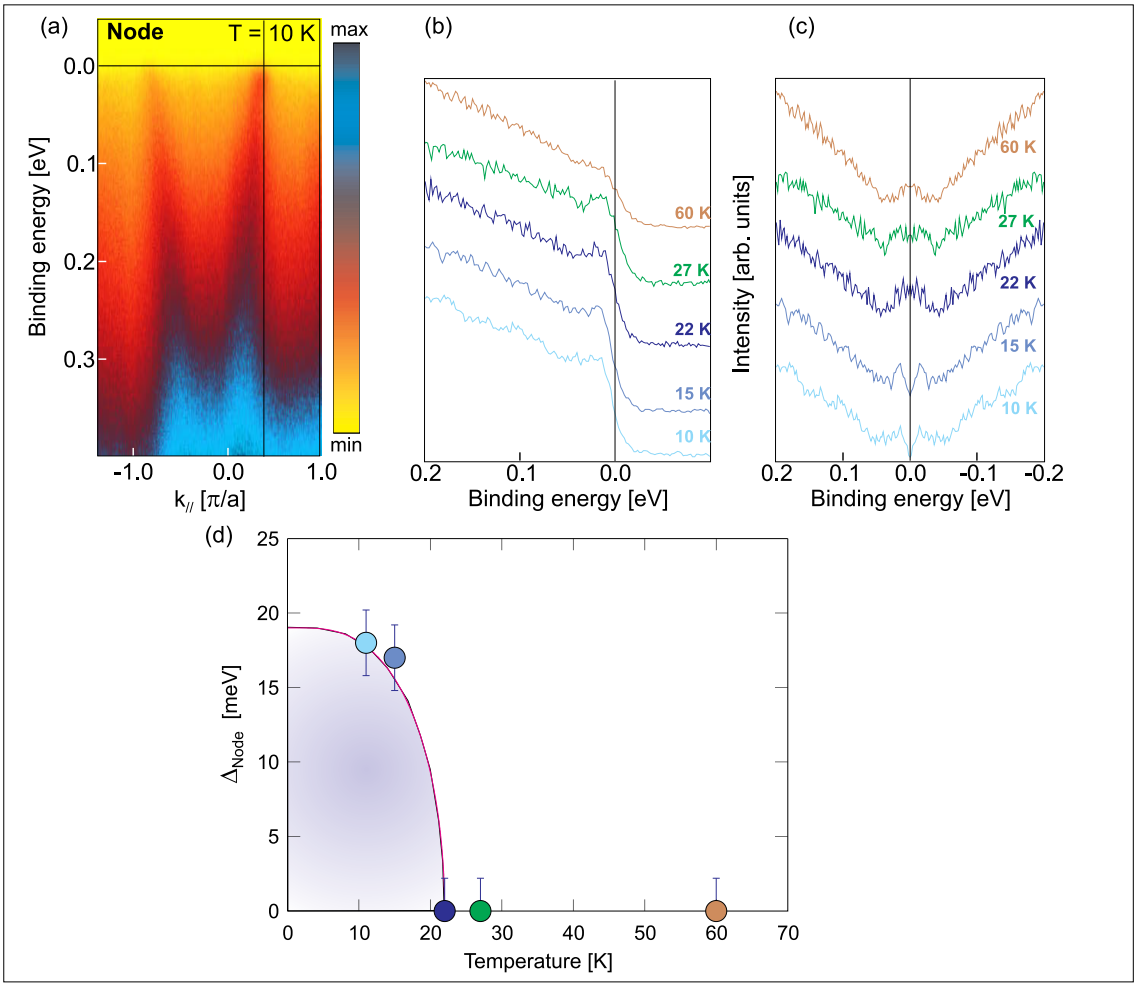

Figure 5.15: (a) Nodal spectrum corresponding to a Fermi surface angle $\varphi = 45°$. (b) EDC's obtained at k_F as function of the temperature. (c) Symmetrized EDC's to estimated the gap size. (d) Magnitude of the gap Δ_{Node} as function of the temperature.

the extinction of the gap. It is at $T = 60$ K that the coherent peak is lost, which is in line with the temperature dependence of the off-nodal spectrum. However, it is worth noting that the temperature range at which the gap closes is comparable to the so-called low-temperature kink (LTK) of the London penetration depth λ_{ab}(T) curve found in low-energy μ^+SR investigation was performed on YBCO films and single crystals [222]. Such deviation of the d-wave parameter was interpreted as a mixture of $(s + d)$-wave symmetry where the s-wave contribution prevails at very low temperatures ($T < T_{LTK}$). When $T > T_{LTK}$, the main symmetry observed is d-wave. For the YBCO films studied in this work, an initial low-energy μ^+SR experiment were performed and the results are described in Appendix C. The LTK at $T \approx 20$ K is found, which agrees well with previous μ^+SR data of YBCO single crystals and films [222, 225]. Nevertheless, at present time, no solid con-

clusion/connection between the two techniques can be made since the low-energy μ^+SR measurement performed on our YBCO films need to be reproduced and improved. Indeed, to obtain significant results with this technique, it is essential that all the films are very well oriented and that the contribution of the substrate is minimal.

To summarize, by extracting the temperature dependence of the off-nodal, antinodal and nodal spectra, we managed to estimate the T_c of the $YBCO_{6.5}$ film, which is in agreement with the ortho-II phase ($T_c \approx 65$ K). The magnitude of the SC gap as function of temperature is in line with a d-wave order parameter. Moreover, the persisting antinodal gap above T_c and the closing of the off-nodal cut, strongly suggest the existence of a pseudogap state. Surprisingly, the gap along the (π, π) direction seems to display a different temperature dependence and closes at a much lower temperature. However, more investigations are needed before drawing any definite conclusion.

5.2.5 Pseudogap state

As observed for many HTSC, in the underdoped regime above the transition temperature, a strange phase with unusual physical properties exists. As previously mentioned, this so-called pseudogap state is characterized by a persistent energy gap around the (π, 0) region [43,150,151]. In addition, the so-called Fermi arc [136] is present, centered around the (0,0)-(π, π) line. The relation between the pseudogap and the superconducting states remains a central question in the HTSC community [167]: Does the pseudogap derive from superconductivity itself or is it a result from a competing order parameter? From this issue, two main scenarios are developed. The so-called *single gap scenario*, which suggests that the pseudogap is a form of precursor pairing that evolves into the phase-coherent SC state at T_c [226]. The pseudogap is then a disordered pairing state with strong phase fluctuations. The other picture is the *two-gap scenario*, which states that only the Fermi arcs reflect the superconducting order whereas the energy gap set around the antinodal region is from the pseudogap state. Recently, a quantitative analysis of ARPES data have suggested that the PSG region is composed of the two coexistence states [227]. The first one consists to pair formation, which persists up to an intermediate temperature called T_{pair} where $T_{pair} < T^*$. The second is the PSG state itself defined by the loss of spectral weight and anomalies in transport measurements, which persists up to T^*. At present time, experimental investigations could not furnish a final word [227–232] and thus, leaves the pseudogap state far from being understood. However, further experiments on both superconducting and pseudogap states on a series of HTSC samples is the best approach to make a distinction between these theories. Most of the ARPES investigations made in the pseudogap state were done on BiSCO and LSCO compounds [139, 229, 231, 233]. To the best of our knowledge, due to the overdoped surface in cleaved YBCO samples, very few investigations of the pseudogap state were reported [205]. From this point of view, the underdoped surface of the YBCO film studied in this thesis, gives a great opportunity to explore this mysterious phase. In what follows, a quantitative study of the pseudogap state for $YBCO_{6.5}$ surface is presented. A **k**-momentum investigation is made and all data were obtained at $T = 120$ K in the pseudogap state with a photon energy $h\nu = 70$ eV using circularly polarized light. The sample was permanently in electrical and thermal contact with a polycrystalline copper sample holder used as reference and a copper spectrum was regularly acquired to verify the stability of the photon energy.

To assure that the ortho-II order remains in the pseudogap state, we have acquired spectra for multiple momentum cuts and mapped out the FS of the $YBCO_{6.5}$ surface at $T = 120$ K. Figure 5.16(a) displays the energy map at E_F integrated over a $\pm$ 5 meV window. The band folding causes by the reduced Brillouin zone of the ortho-II is even more visible at high temperature, above the SC transition T_c of the film. By following the highest intensity on the FS, one can easily see that

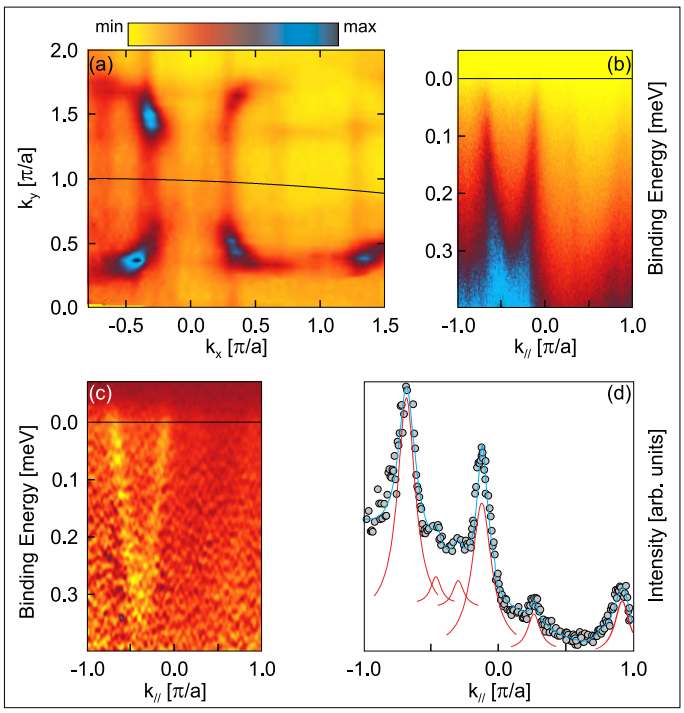

Figure 5.16: (a) Spectral intensity map of the YBCO film integrated around the Fermi level with an energy window of ± 5 meV. Data were acquired at T = 120 K with a photon energy hν = 70 eV and circular polarized light. The black solid line represents the cut of the antinodal spectrum displayed in (b). (c) First derivative of the antinodal spectrum where two dispersive bands can be observed having their bottom around 300 and 10 meV . (d) Momentum distribution curve (MDC) at the Fermi level and a Lorentzian fit (solid blue and red dashed lines).

it corresponds to the nodal region where a gapless region (Fermi arcs) is found. Figure 5.16(b-c) represents the antinodal spectrum and its first derivative. As for the antinodal spectrum acquired at T = 10 K [Fig. 5.7(a-d)], the dispersive parabolic bonding band is clearly visible having its bottom at $E_B \approx 300$ meV. On the contrary, the intensity of the antibonding band is not as noticeable at T = 120 K. As previously mentioned, the parabolic-like antibonding band is very close to E_F and due to the thermal broadening at high temperature, we can suppose that the intensity of the band is simply blurred out making its distinction delicate. However, by fitting the MDC at E_F with Lorentzians [Fig. 5.16(d)], two extra peaks are clearly discernable leaving no doubt about the presence of also the antibonding band.

Figure 5.17(a,c) displays the EDCs obtained at different k_F along the FS from the nodal ① to the antinodal ⑦ points [Fig. 5.17(e)]. A weak coherent peak is noticeable for all cuts in **k**-space. From the temperature dependent measurement

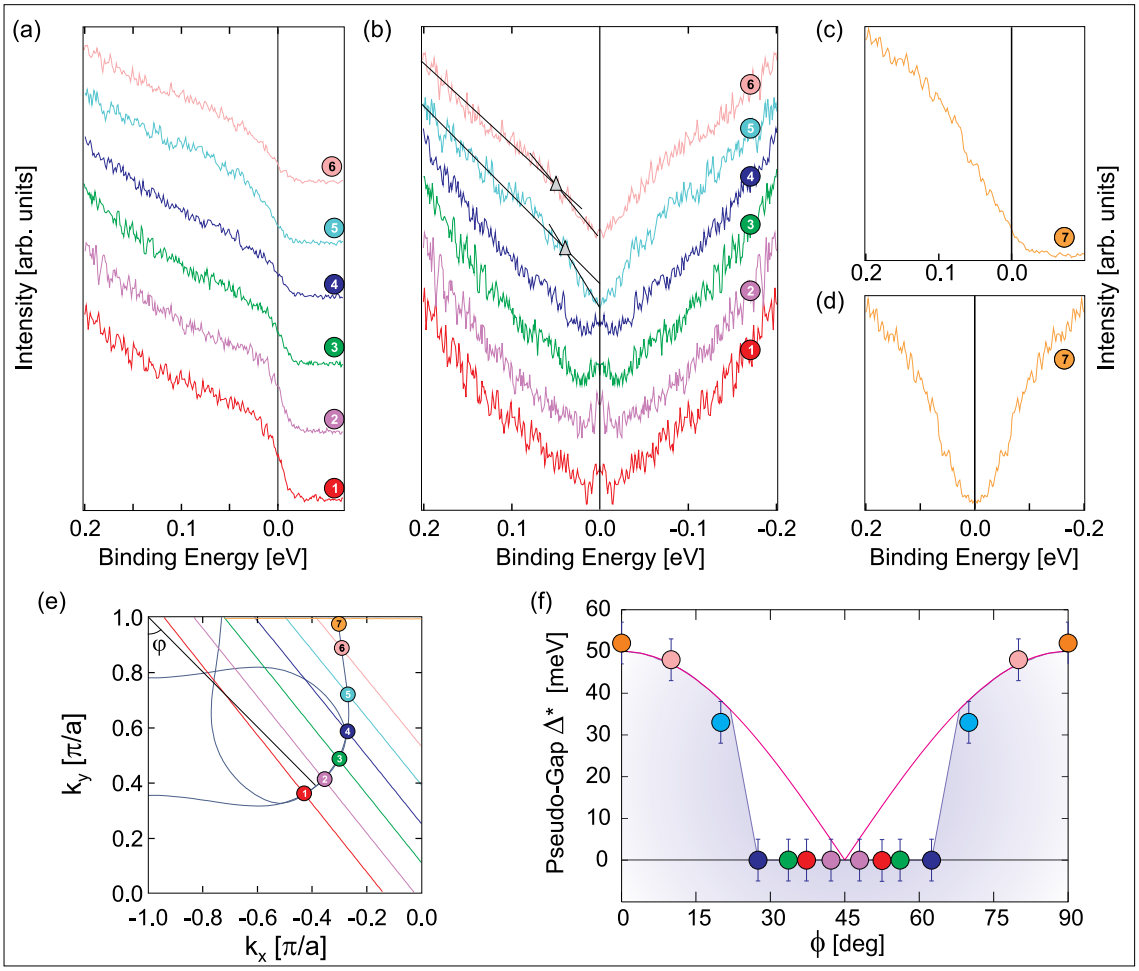

Figure 5.17: (a,c) Energy distribution curves obtained at different **k**-momentum and their symmetrization curves in (b,d). (e) Location of the EDCs in **k**-space. (f) Gap profile Δ^* as function of the Fermi surface angle. The dashed curve is the simple d-wave form $\Delta_{max}\cos(2\phi)$ with $\Delta_{max} = 50$ meV. The solid line is a guide for the eyes. The pseudogap exists around the antinodal region and vanishes on the Fermi arc around the node.

presented in the previous section, the QP lost its spectral weight in the pseudogap state above the transition temperature ($T_c = 60$ K) of the $YBCO_{6.5}$ surface. The loss of coherence in the pseudogap state makes it difficult to follow the evolution of the EDC peaks as a function of **k**-momentum. However, taking into account the leading edge of the EDCs, one can observe that EDC ⑤, EDC ⑥ and EDC ⑦ are shifted from E_F implying the opening of a larger gap. Figure 5.17(b,d) shows the symmetrized EDC where a closed gap is observed for EDCs ①, ②, ③, ④ and an open one for EDCs ⑤, ⑥ and ⑦. To achieve a better understanding, Fig. 5.17(f) displays the angular dependence of the pseudogap deduced from the change of slope in the symmetrized EDC as function of the FS angle φ. For commodity,

all the cuts have been transposed in the (0, 0)-(-π, π) quadrant of the FS and then symmetrized around $\varphi = 45°$. From this plot, the pseudogap seems to exist around the (π, 0) region and vanishes on the Fermi arc where a gapless excitation is seen. Within the error bars, the amplitude of the antinodal gap both in the pseudogap and the superconducting states are similar[6]. The observation of a pseudogap with an amplitude $\Delta_{\text{Antinode}} = 52 \pm 4$ meV and the existence of Fermi arcs are in good agreement with what has been reported in recent measurements for YBCO with $p = 0.06$ hole doping [205].

To summarize, the k-dependence of the pseudogap state were investigated for the ortho-II $YBCO_{6.5}$ surface. The amplitude of the antinodal gap $\Delta_{\text{Antinode}} \approx 52 \pm 4$ meV with the existence of Fermi arcs were found to be consistent with a recent report made on underdoped YBCO single crystals [205]. No evidence for a much larger gap in the antinodal region was detected and more significantly, the magnitude of the pseudogap is comparable with the superconducting gap. The band-folding connected to the reduced Brillouin zone of the ortho-II detected in the superconducting state is clearly visible also in the pseudogap state. With the presented data it is delicate to give any conclusive answer about the nature of the pseudogap state. Indeed, the Fermi arcs detected around the node can be interpreted as both competing order parameters and precursor of superconductivity. Further, high resolution measurements are necessary to clarify this issue.

[6]The amplitude of the gap both in the pseudogap and superconducting states was verified in many sample and all showed the same behavior and magnitude.

6 Summary and Conclusions

The electronic properties of $YBa_2Cu_3O_{7-\delta}$ (YBCO) thin-films *in situ* grown by pulsed laser deposition (PLD) have been investigated by angle-resolved photoelectron spectroscopy (ARPES). The samples were grown on TiO_2 terminated $SrTiO_3$ (STO) substrates, resulting in a CuO chain termination on the surface [94]. The films were *c*-axis oriented with a hole doping corresponding to an optimally doped sample ($p_{\text{bulk}} \approx 0.18$). In addition, high- and low-energy electron diffraction measurements (RHEED/LEED) were performed to examine the surface of the films. The measurement showed a good crystalline surface with a unit-cell doubling corresponding to a (2×1) surface reconstruction caused by ordered oxygen vacancies within the CuO chains that help to stabilize the polar surface of the film.

By a direct *in situ* transfer between the PLD and ARPES set-up, the YBCO films were measured without cleaving, a task previously thought impossible due to oxygen deficiency causing an insulating surface. The ARPES data show electronic properties and a Fermi surface (FS) volume corresponding to a lightly hole doped surface ($p_{\text{surf}} \approx 0.10$). Further, in line with the (2×1) surface reconstruction observed by RHEED/LEED, the FS also display clear evidence of an ortho-II ordered $YBa_2Cu_3O_{6.5}$ ($YBCO_{6.5}$) band folding. These findings confirm theoretical predictions [193–195] and point out how the order within the CuO chains affects the electronic properties of the CuO_2 planes. Further, this demonstrates the importance of having not only the correct surface carrier concentration, but also a very well ordered clean surface in order to obtain photoemission data representative of the compound's true nature.

The investigation of the superconducting state reveal a series of interesting result. Even though the **k**-dependence of the superconducting gap is anisotropic with a maximum amplitude at the antinode ($\Delta_{\text{Antinode}} \approx 52$ meV), the Fermi surface is found to be nodeless with the presence of a gap ($\Delta_{\text{Node}} \approx 20$ meV). Moreover, when increasing the temperature, the gap along the (π, π) direction closes at $T \approx 22$ K. This is much lower than the transition temperature of the surface (Tc ≈ 65 K) extracted from both the hole doping and the temperature dependence of the off-nodal gap. The origin of the gap along the nodal direction is not clear but several scenarios can be considered. One of the most simple explanations would be that when measuring the amplitude of the gap, the folded band was followed instead of the main band. Such error is very easy to imagine since these two bands strongly overlap in the nodal region. However, this suggestion does not explain

the premature closing of the gap. Another scenario is to consider an *s*-wave contribution of the gap symmetry at low temperature as already suggested by muons spin rotation measurements. Currently, the origin of the nodeless behavior remains unclear and further theoretical as well as experimental investigations are needed.

Given that the surface of the YBCO film is underdoped, also the pseudogap state has been studied. The **k**-dependence of the pseudogap state reveal clear Fermi arcs centered around the node and the magnitude of the antinodal (maximum) pseudogap is comparable to the superconducting gap. Both observations are in good agreement with recent measurement done on underdoped YBCO single crystals [205]. Further, the band folding detected in the superconducting state remains clearly visible also in the pseudogap state.

Independently of the band folding, a low-energy kink ($E_0 = 60$ eV) and a weak bilayer splitting were observed. The E_0 value agrees well with previous report on lightly hole doped cuprate. Concerning the weak bilayer splitting, two suggestions can be considered. The first one is that the photon energy chosen for the measurement ($h\nu = 70$ eV) more strongly emphasizes the intensity of the bonding band than the antibonding band. The second one is connected to the recent report made by Fournier *et al.*, which observes that the bilayer splitting is progressively reduced upon underdoping and vanishes when the hole doping $p < 0.15$ [205]. At present time, none of these suggestions can be excluded since the influence of the photon energy on the bilayer splitting was not investigated in the YBCO films. Nevertheless, this experiment can easily be performed in a near future.

In conclusion, we believe that it has been clearly shown that the approach to grow YBCO films *in situ* and measure them by ARPES is a successful concept. Our data evidently show that in order to gain access to information regarding the bulk electronic properties by ARPES it is of crucial importance to have a careful control of the surface properties. At present, the combination of the PLD and ARPES technique has allowed us to reveal the existence of a band folding in the previously unaccessible underdoped ortho-II ordered $YBCO_{6.5}$ compound. Our results have not only opened the door to study the details of the superconducting properties in this system, but also given the opportunity to more accurately connect a bulk-like electronic structure with results from other experimental techniques as well as theoretical models.

A Change of the t'/t and t''/t' parameters

To perform the hopping parameter test, we have changed the chemical potential μ and the second nearest hopping integral t' terms alternatively. Changing μ and t' change the ratios μ/t and both t'/t and t''/t'. The others parameters t, t'' and V kept the same values as the one defined in Chapter 5. Table (A.1) shows the initial value of the tight-binding parameters.

Compound	T_c [K]	t [eV]	t'/t	t''/t'	μ/t
Films YBCO	~ 65	0.558	0.49	0.5	-0.842
Single crystals ortho-II YBCO [193]	~ 60	0.36	0.4	0.5	-0.866

Table A.1: Comparison of the tight-binding parameters of YBCO ortho-II compound.

Figure. A.1 and Fig. A.2 shows the resulting band calculation when the ratio $\mu/t = -1.204$ and $t'/t = 0.855$ ($t''/t' = 0.289$). The yellow and black solid lines represents the β and α bands, respectively. With the calculated bands, the experimental energy maps of the YBCO film as function of the binding energy (E_B). Each map was integrated within $\pm$ 5 meV window around (E_B). In both figures, it is clear that the band calculation do not fit the experimental data. Even though at low-energy the bands seem to follow the measurement, at high binding energy a very strong discrepancy is observed.

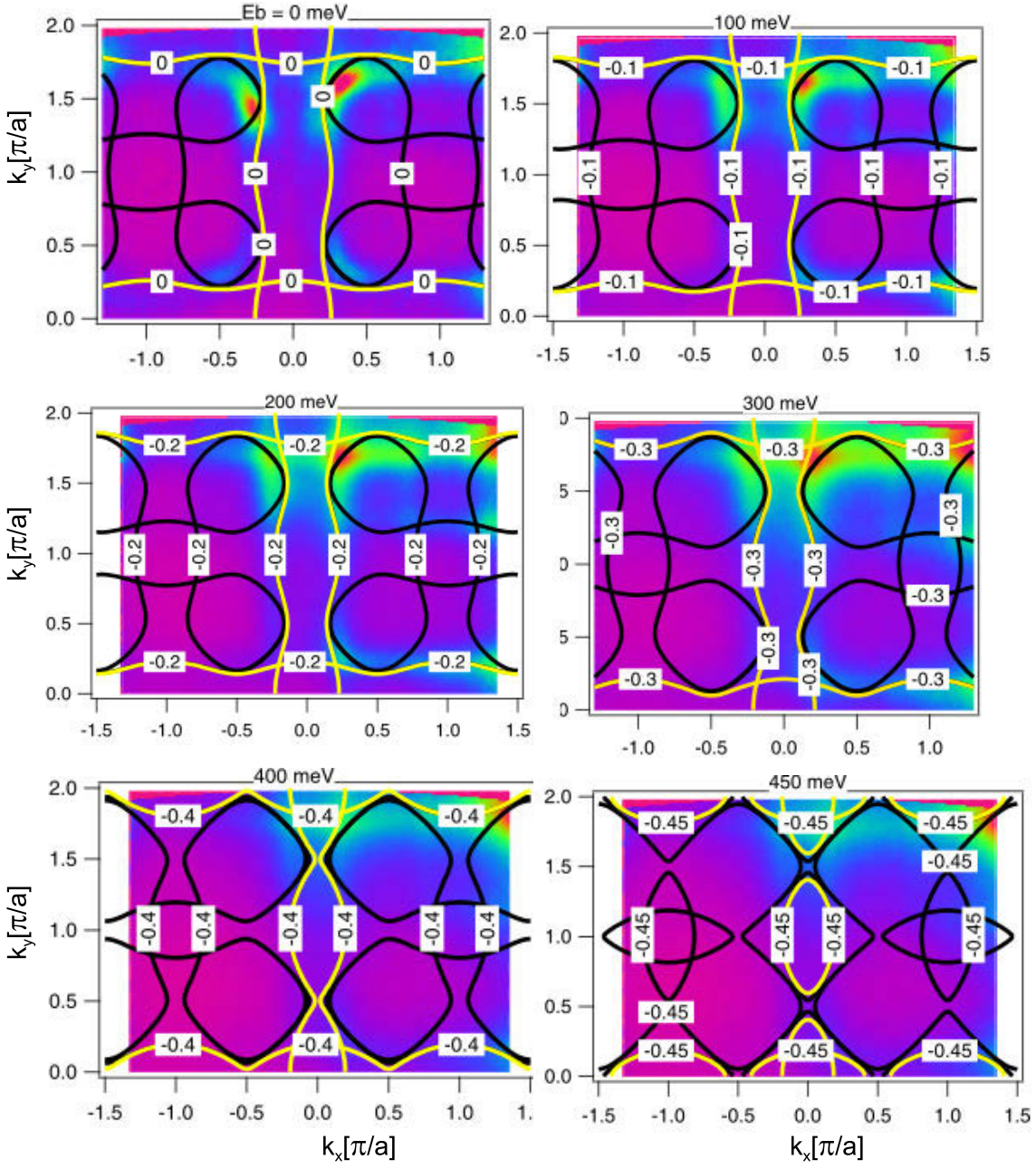

Figure A.1: Calculated band structure with μ/t = -1.204.

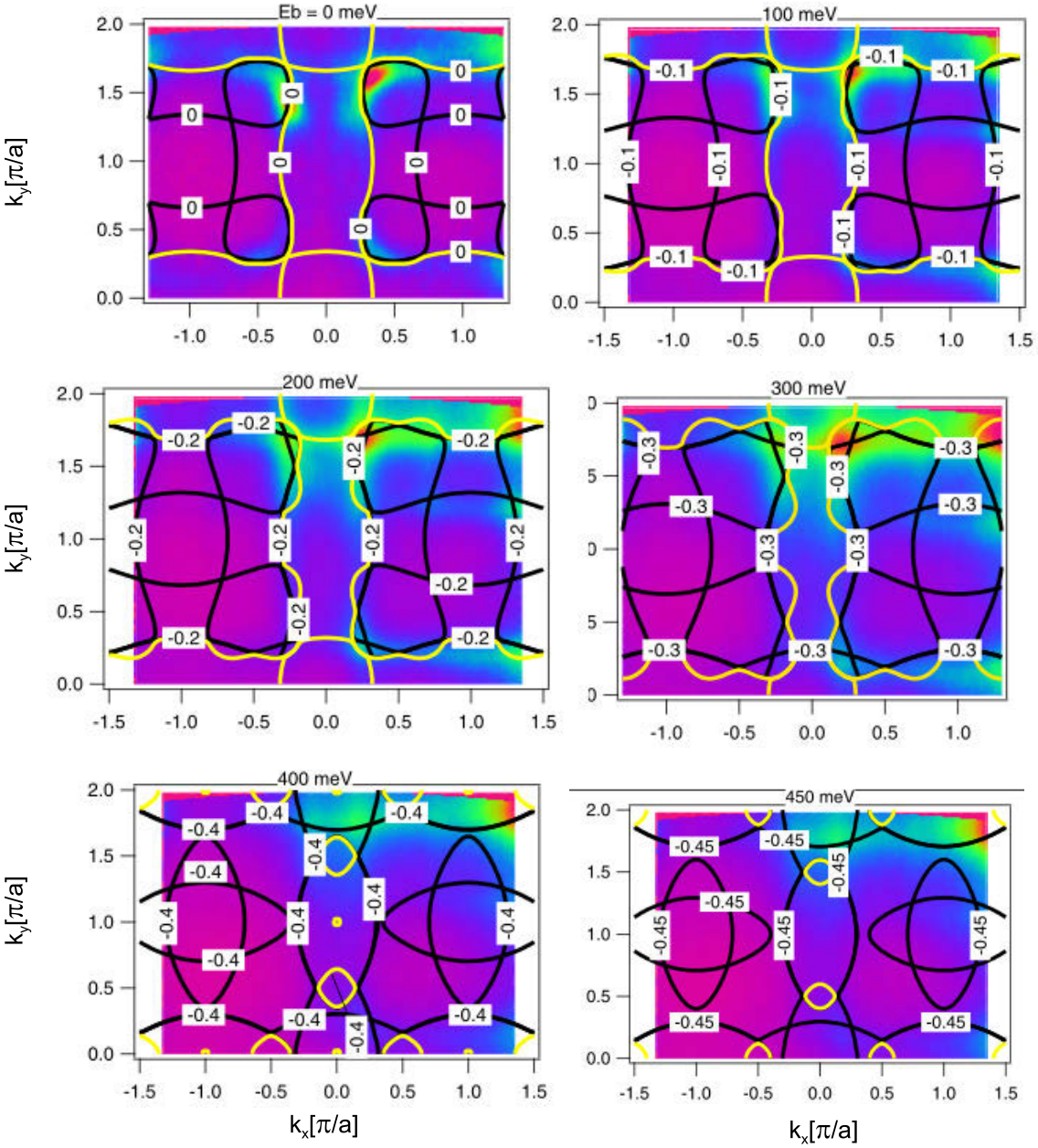

Figure A.2: Calculated band structure with $t'/t = 0.855$ and $t''/t' = 0.289$.

B Simulated intensity maps

To evaluate the evolution of the energy maps using the hopping parameters extracted from the YBCO film studied in this work, we have simulated the intensity maps of a twinned ortho-II sample as function of binding energy using the planar dispersion, herein defined by:

$$\begin{aligned} \epsilon_{\alpha,\beta}^{AB,B}(\mathbf{k}) &= -2t\cos k_y - 2t''(\cos 2k_x + \cos 2k_y) \\ &- \mu \pm t_\perp(\mathbf{k}) \pm \left[4\cos^2 k_x (t - 2t'\cos k_y)^2 + \frac{V^2}{4}\right]^{\frac{1}{2}}, \end{aligned} \tag{B.1}$$

and the fact that $I(\mathbf{k},\omega) \propto A(\mathbf{k},\omega)$. The k-dependency of the bands has not been take into account and a constant energy broadening of 25 meV was chosen for all the maps. Figure B.1 shows the simulated intensity maps as function of binding energy for the following fitting parameters: $t = 558$ meV, $t'/t = 0.49$, $t''/t' = 0.5$, $\mu/t = -0.842$ meV, and $V = 75$ meV. The interlayer hopping $t_\perp = 0$ meV and the ortho-II potential V = 75 meV. One can see that the quasi-1D character of the β bands is predominant and the "bottom" of the bands is at 1200 meV.

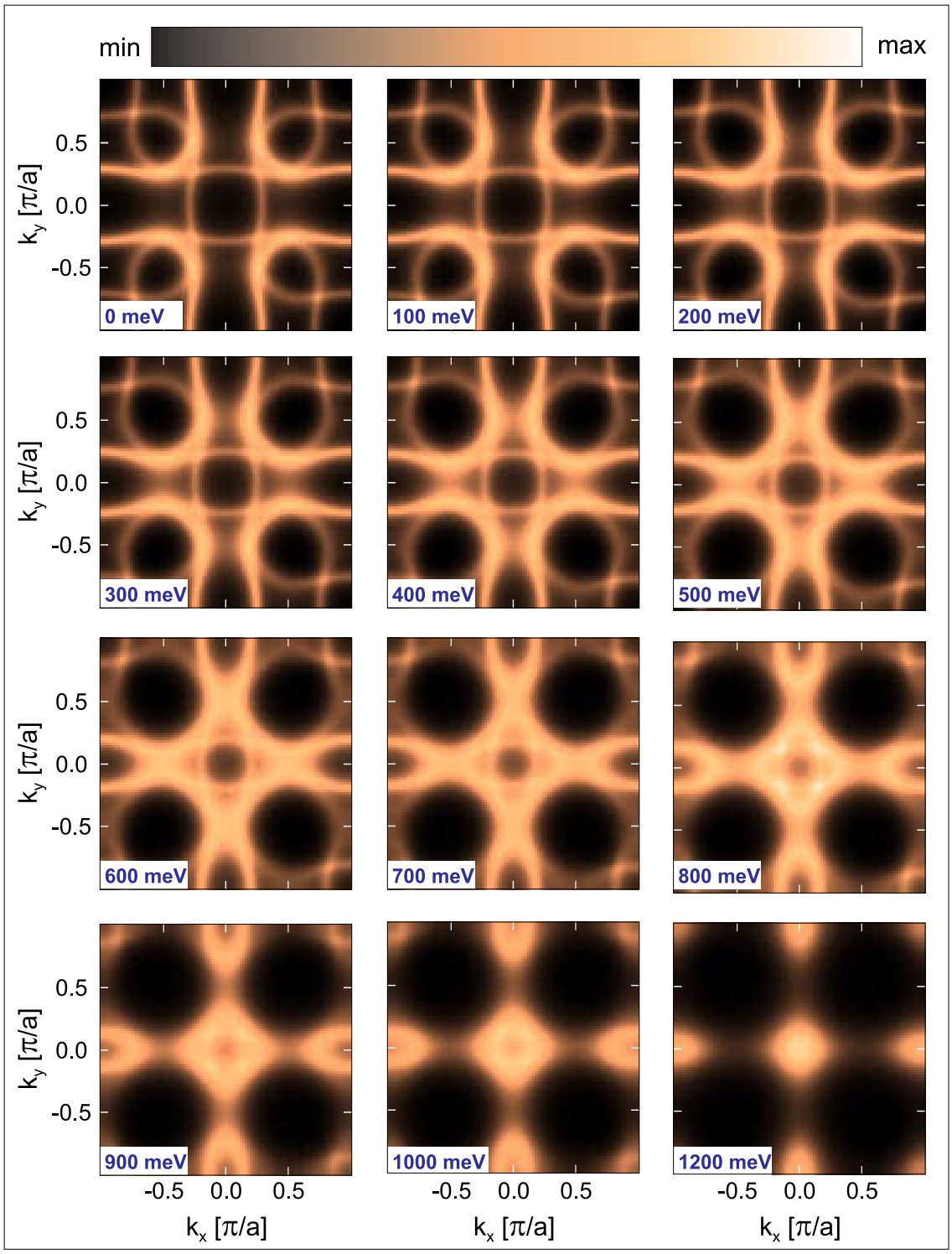

Figure B.1: Simulations of the intensity maps for the ortho-II FS with the TB parameters issue the YBCO film: t = 558 meV, t'/t = 0.49, t''/t' = 0.5, μ/t = -0.842 meV, and V = 75 meV.

C Initial Low-Energy Muon Investigation of the YBCO film studied by ARPES

Here, we present an investigation of the magnetic properties of high-temperature superconducting (HTCS) $YBa_2Cu_3O_{7-\delta}$ (YBCO) films using low-energy muon spin spectroscopy (LEM). The YBCO films are grown using pulsed laser deposition (PLD) and were previously investigated by ARPES. The films are grown on $SrTiO_3$ (STO) substrate and have a thickness of $\sim$ 150 nm. To perform the LEM experiment, we have grown eight (5 $\times$ 10 mm) YBCO films under the same conditions and have glued them on a nickel plate with silver paint [Fig. C.1(a)]. The white borders of each films are the STO substrate. Fig. C.1(b) shows one of the bulk resistivity measurement made on these samples where the transition temperature is T_c = 86.5 K and ΔT_c = 1 K.

By taking into account the muons stopping distribution in YBCO, our initial measurements allowed us to extract the London penetration-depth (λ_{ab}) of the samples at 5 K in the Meissner state with an external magnetic field of 100 G applied parallel to the *ab*-plane. From this we obtained $\lambda_{ab}(5\ K) \approx 160$ nm, which agrees well with previous μSR data of YBCO single crystals and films [222, 225]. We also managed to extract the superconducting (SC) range of our samples, which corresponds to $\sim$130 nm and the top-deadlayer is estimated to be $\sim$15 nm. The deadlayer on the surface is due that the films were transferred *ex situ*, which is not the case for the ARPES experiment.

Our second test allowed us to acquire λ_{ab} as a function of temperature (T = 5-120 K) for an implantation depth of 70 nm and with a magnetic field of 100 G. For each data point, the counting statistics were $\sim$ 6 million muon decays. Fig. C.1(c) shows $1/\lambda_{ab}^2$ as a function of T. A clear transition is visible around T = 85 K, which is in agreement with the bulk resistivity measurement showed in Fig. C.1(b). Further, at low-temperature, a clear upturning of $1/\lambda_{ab}^2$ curve is seen for T below 20 K. This low-temperature "kink"(LTK) [234] has already been reported for YBCO single crystals [222] and interpreted as a mixture of $(s+d)$-wave symmetry.

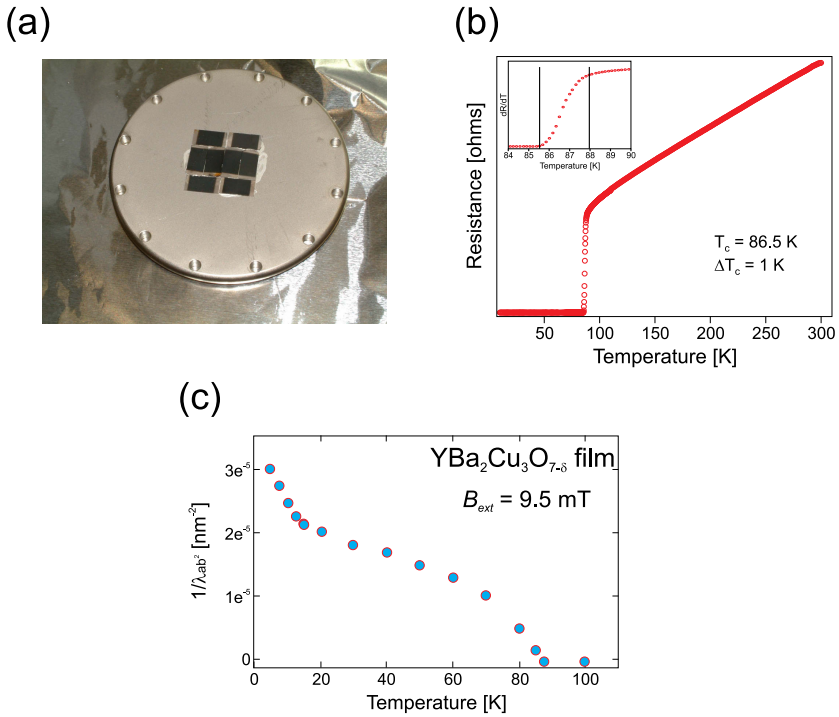

Figure C.1: (a) YBCO films glued on the low-energy μSR sample holder (Nickel plate). After fixing the samples, the plate is mounted inside a low-temperature cryostat with a minimum temperature of 2 K. (b) Resistivity curve of the YBCO sample. The measurement were done with a classical four points probe. Note that the resistivity extracted from the curve corresponds to the bulk. (c) Temperature dependence of the inverse square London penetration depth $1/\lambda_{ab}^2$ is observed. At $T \approx 20$ K, the low-temperature "kink" (LTK) and the superconducting transition temperature is extracted as $T_c = 85$ K, which is in good agreement with the resistivity measurement.

Such unusual behavior is difficult to explain but can possibly be connected to future ARPES investigation.

Bibliography

[1] F. Bloch, Z. Phys. **57** (1929), 545. 3

[2] A. H. Wilson, Proc. Roy. Soc. of London Series A **133** (1931), 458. 3

[3] H. J. De Boer and E. J. W. Verwey, Proc. Phys. Soc. of London Series A **49** (1937), 59. 3

[4] N. F. Mott and R. Peierls, Proc. Phys. Soc. of London **49** (1937), 72. 3

[5] N. F. Mott, Proc. Phys. Soc. of London Series A **62** (1949), 416. 3, 8

[6] J. Hubbard, Proc. Phys. Soc. of London Series A **277** (1964), 237. 3

[7] P. W. Anderson, Phys. Rev. **115** (1959), 2. 3, 8, 13

[8] H. Kamerlingh Onnes, Commun. Phys. Lab.Univ. Leiden **120b, 122b** (1911), 124c. 4

[9] K. Shimizu, T. Kimura, S. Furomoto, K. Takeda, K. Kontani, Y. Onuki and K. Amay, Nature **412** (2001), 316. 4

[10] W. Meissner, R. Ochsenfeld, Naturwissenschaften **21** (1933), 787. 4

[11] E. Maxwell, Phys. Rev. B **78** (1950), 477. 4

[12] V.L. Ginzburg and L.D. Landau, Zh.Eksp. Teor. Fiz. **20** (1960), 1064. 4

[13] J. Bardeen, L.N. Cooper and J.R. Schrieffer, Phys. Rev. **108** (1957), 1175. 4, 12

[14] L. N. Cooper, Phys. Rev. **104** (1956), 1189. 4

[15] J. G. Bednorz and K. A. Müller, Z. Phys. B **64** (1986), 189. 4

[16] M. K. Wu, J. R. Ashburn, C. J. Torng, P. H. Hor, R. L. Meng, L. Gao, Z. J. Huang, Y. Q. Wang, and C. W. Chu, Phys. Rev. Lett. **58** (1987), 908. 4, 29

[17] H. Maeda, Y. Tanaka, M. Fukutomi and T. Asano, Jpn. J. Appl. Phys. **27** (1988), 209. 4

[18] A. Schilling, M. Cantoni, J. D. Guo and H. R. Ott, Nature **363** (1993), 56. 4

[19] L. Gao, Z. J. Huang, R. L. Meng, J. G. Lin, F. Chen, L. Beauvais, Y. Y. Shen, Y. Y. Xue and C. W. Chu, Physica C **213** (1993), 261. 4

[20] L. Gao, Y. Y. Xue, F. Chen, Q. Xiong, R. L. Meng, D. Ramirez, and C. W. Chu, Phys. Rev. B **50** (1994), 4260. 4

[21] H. Takahashi, K. Igawa, K. Arii, Y. Kamihara, M. Hirano, and H. Hosono, Nature **453** (2008), 376. 5

[22] Y. Tokura and T. Arima, Jpn. J. Appl. Phys. **29** (1990), 2388. 5

[23] R.J. Cava, A.W. Hewat, E.A. Hewat, B. Batlogg, M. Mareziod, K.M. Rabe, J.J. Krajewski, W.F. Peck and L.W. Rupp, Physica C **165** (1990), 419. 7

[24] R. Beyers and T. M. Shawn, *Solids State Physics*, vol. 42, ed. H. Ehrenreich and D. Turn bull, New-York, 1989. 7, 33, 77

[25] D. de Fontaine, G. Ceder and M. Asta, Nature **343** (1990), 544. 7, 33, 77

[26] Q. Wang, H. Rushan, D. L. Yin and Z. Z. Gan, Phys. Rev. B **45** (1992), 10834. 7

[27] H. Behner, W. Rauch, E. Gornik, Appl. Phys. Lett. **61** (1992), 1465. 7

[28] R. Liang, D. A. Bonn and W. N. Hardy, Physica C **336** (2000), 57. 8

[29] R. Liang, D.A. Bonn, W.N. Hardy, J.C. Wynn, K.A. Moler, L. Lu, S. Larochelle, L. Zhou, M. Greven, L. Lurio and S.G.J. Mochrie, Physica C **383** (2002), 1. 8

[30] N. Doiron-Leyraud, C. Proust, D. LeBoeuf, J. Levallois, J-B. Bonnemaison, R. Liang, D. A. Bonn, W. N. Hardy and L. Taillefer, Nature **447** (2007), 565. 8, 11, 65, 70

[31] D. LeBoeuf, N. Doiron-Leyraud, J. Levallois, R. Daou, J-B. Bonnemaison, N. E. Hussey, L. Balicas, B. J. Ramshaw, R. Liang, D. A. Bonn, W. N. Hardy, S. Adachi, C. Proust and L. Taillefer, Nature **450** (2007), 533–536. 8, 70

[32] C. Jaudet, D. Vignolles, A. Audouard, J. Levallois, D. LeBoeuf, N. Doiron-Leyraud, B. Vignolle, M. Nardone, A. Zitouni, R. Liang, D. A. Bonn, W. N. Hardy, L. Taillefer and C. Proust, Phys. Rev. Lett. **100** (2008), 187005. 8, 70

[33] A. Audouard, C. Jaudet, D. Vignolles, R. Liang, D. A. Bonn, W. N. Hardy, L. Taillefer and C. Proust, Phys. Rev. Lett. **103** (2009), 157003. 8, 70

[34] S. E. Sebastian, N. Harrison, E. Palm, T. P. Murphy, C. H. Mielke, R. Liang, D. A. Bonn, W. N. Hardy and G. G. Lonzarich, Nature **454** (2008), 200. 8, 70

[35] M. Imada, A. Fujimori and Y. Tokura, Rev. Mod. Phys. **70** (1998), 1039. 8, 9, 13

[36] J. Zannen, G. A. Sawatzky and J. W. Allen, Phys. Rev. Lett. **55** (1985), 418. 8

[37] F. C. Zhang and T. M. Rice, Phys. Rev. B **37** (1988), 3759. 9

[38] J. Fink, N. Nücker, H. Romberg and J. C. Fuggle, IBM J. Res. Dev. **33** (1989), 372. 9

[39] Y. Yanase, T. Jujo, T. Nomura, H. Ikeda, T. Hotta, K. Yamada, Phys. Reports **387** (2003), 1–149. 10, 13

[40] C. M. Varma, P. B. Littlewood, S. Schmitt-Rink, E. Abrahams and A. E. Ruckenstein, Phys. Rev. Lett. **63** (1989), 1996. 10

[41] C. M. Varma, P. B. Littlewood, S. Schmitt-Rink, E. Abrahams and A. E. Ruckenstein, Phys. Rev. Lett. **64** (1990), 497. 10

[42] T. Timusk and B. Statt, Rep. Prog. Phys. **62** (1999), 61. 11, 62

[43] H. Ding, T. Yokoya, J. C. Campuzano, T.Takahashi, M. Randeria, M. R. Norman, T. Mochiku, K. Kadowaki, and J. Giapintzakis, Nature **382** (1996), 51. 11, 94

[44] J. C. Campuzano, H. Ding, M. R. Norman, H. M. Fretwell, M. Randeria, A. Kaminski, J. Mesot, T. Takeuchi, T. Sato, T. Yokoya, T. Takahashi, T. Mochiku, K. Kadowaki, P. Guptasarma, D. G. Hinks, Z. Konstantinovic, Z. Z. Li, and H. Raffy, Phys. rev. Lett **83** (1999), 3709. 11

[45] M. Shi, A. Bendounan, E. Razzoli, S. Rosenkranz, M. R. Norman, J. C. Campuzano, J. Chang, M. Månsson, Y. Sassa, T. Claesson, O. Tjernberg, L. Patthey, N. Momono, M. Oda, M. Ido, S. Guerrero, C. Mudry and J. Mesot, Euro Phys. Lett. **88** (2009), 27008. 11, 58, 62, 63

[46] M. R. Norman, H. Ding, J. C. Campuzano, T. Takeuchi, M. Randeria, T. Yokoya, T. Takahashi, T. Mochiku and K. Kadowaki, Phys. Rev. Lett. **79** (1997), 3506. 11, 61

[47] Z. A. Xu, N. P. Ong, Y. Wang, T. Kakeshita, and S. Uchida, Nature **406** (2000), 486. 11

[48] Y. Wang, N. P. Ong, Z. A. Xu, T. Kakeshita, S. Uchida, D. A. Bonn, R. Liang, and W. N. Hardy, Phys. Rev. Lett. **88** (2002), 257003. 11

[49] H. V. Löhneysen, A. Rosch, M. Vojta, and Peter Wölfle, Rev. Mod. Phys. **79** (2007), 1015. 11, 34

[50] J. M. Tranquada, D. E. Cox, W. Kunnmann, H. Moudden, G. Shirane, M. Suenaga, P. Zolliker, D. Vaknin, S. K. Sinha, M. S. Alvarez, A. J. Jacobson and D. C. Johnston, Phys. Rev. Lett. **60** (1988), 156. 11

[51] K. Segawa and Y. Ando, Phys. Rev. Lett. **86** (2001), 4907. 12

[52] T. A. Zaleski and T. K. Kopeć, Phys. Rev. B **74** (2006), 014504. 12

[53] B. W. Veal and A. P. Paulikas, Physica C **184** (1991), 321, and references therein. 12

[54] J. L. Tallon, G. V. M. Williams, N. E. Flower, and C. Bernhard, Physica C **282** (1997), 236. 12

[55] J. M. Tranquada, B. J. Sternlieb, J. D. Axe, Y. Nakamura, Nature **375** (1995), 561. 12

[56] N. E. Bickers, D. J. Scalapino and R. T. Scalettar, Int. J. Mod. Phys. B **1** (1987), 684. 12

[57] H. J. Schulz, Europhys. Lett. **4** (1987), 609. 12

[58] H. Yokoyama and H. Shiba, J. Phys. Soc. Japan **57** (1988), 2482. 12

[59] S. R. White, D. J. Scalapino, R. L. Sugar, N. E. Bickers and R. T. Scalettar, Phys. Rev. B **39** (1989), 839. 12

[60] M. Imada and Y. Hatsugai, J. Phys. Soc. Japan **58** (1989), 3752. 12

[61] D. J. Van Harlingen, Rev. Mod. Phys. **67** (1995), 515. 12, 87

[62] S. Kashiwaya and Y. Tanaka, Rep. Prog. Phys. **63** (2000), 1641. 12

[63] D. A. Wollmann, D. J. Van Harlingen, W. C. Lee, D. M. Ginsberg and A. J. Leggett, Phys. Rev. Lett. **71** (1993), 2134. 12

[64] C. C. Tsuei, J. R. Kirtley, C. C. Chi, L. S. Yu-Jahnes, A. Gupta, T. Shaw, J. Z. Sun and M. B. Ketchen, Phys. Rev. Lett. **73** (1994), 593. 12

[65] J. Mesot, M. R. Norman, H. Ding, M. Randeria, J. C. Campuzano, A. Paramekanti, H. M. Fretwell, A. Kaminski, T. Takeuchi, T. Yokoya, T. Sato, T. Takahashi, T. Mochiku and K. Kadowaki, Phys. Rev. Lett. **83** (1999), 840. 12, 62

[66] Z. X. Shen, D. S. Dessau, B. O. Wells, D. M. King, W. E. Spicer, A. J. Arko, D. Marshall, L. W. Lombardo, A. Kapitulnik, P. Dickinson, S. Doniach, J. DiCarlo, T. Loeser and C. H. Park, Phys. Rev. Lett. **70** (1993), 1553. 12, 43

[67] Z. X. Shen and D. S. Dessau, Phys. Rep. **253** (1995), 1. 12

[68] H. Ding, J. C. Campuzano, A. F. Bellman, T. Yokoya, M. R. Norman, M. Randeria, T. Takahashi, H. Katayama-Yoshida, T. Mochiku, K. Kadowaki and G. Jennings, Phys. Rev. Lett. **74** (1995), 2784. 12, 86

[69] M. R. Norman, M. Randeria, H. Ding, J. C. Campuzano and A. F. Bellman, Phys. Rev. B **52** (1995), 15107. 12, 86

[70] H. Ding, M. R. Norman, J. C. Campuzano, M. Randeria, A. F. Bellman, T. Yokoya, T. Takahashi, T. Mochiku and K. Kadowaki, Phys. Rev. B **54** (1996), R9678. 12

[71] J. Zaanen, S. Chakravarty, T. Senthil, P. Anderson, P. Lee, J. Schmalian, M. Imada, D. Pines, M. Randeria, C.M Varma, M. Vojta and M. Rice, *Towards a complete theory of High-T_c*, Nat. Phys. **2** (2006), 138. 13

[72] J. Lee, K. Fujita, K. McElroy, J. A. Slezak, M. Wang, Y. Aiura, H. Bando, M. Ishikado, T. Masui, J.-X. Zhu, A. V. Balatsky, H. Eisaki, S. Uchida and J. C. Davis, Nature **442** (2006), 546. 13

[73] N. Gedik, D-S. Yang, G. Logvenov, I. Bozovic, and A. H. Zewail, Science **316** (2007), 425. 13

[74] Y. Suzumura, Y. Hasegawa and H. Fukuyama, J. Phys. Soc. Japan **57** (1988), 401. 13

[75] H. Fukuyama, Prog. Theor. Phys. Suppl. **108** (1992), 287. 13

[76] C. M. Varma, Phys. Rev. B **73** (2006), 155113. 13

[77] S. Chakravarty, R. B. Laughlin, D. K. Morr and C. Nayak, Phys. Rev. B **63** (2001), 094503. 13, 87

[78] S. A. Kivelson, E. Fradkin, and V. J. Emery, Nature **393** (1998), 550. 13

[79] M. Vojta, Y. Zhang, and S. Sachdev, Phys. Rev. Lett. **85** (2000), 4940. 13

[80] A. V. Chubukov and D.K. Morr, Phys. Rep. **288** (1997), 355. 13, 59

[81] D. Dijkkamp, T. Venkatesan, X. D. Wu, S. A. Shaheen, N. Jisrawi, Y. H. Min-Lee, W. L. McLean, and M. Croft, Appl. Phys. Lett. **51** (1987), 619. 15

[82] D. B. Chrisey and G. K. Hubler, *Pulsed Laser Deposition of Thin Films*, Wiley Interscience, 1992. 15

[83] J. C. Miller, *Laser ablation: principles and applications*, 1994. 15

[84] R. Eason, *Pulsed Laser Deposition of Thin Films. Applications led growth of functional materials*, Wiley Interscience, 2007. 15

[85] M. Von Allmen and A. Blatter, *Laser Beam Interaction with Materials, 2^{nd} edition*, Springer-Verlag, 1995. 16

[86] K. Oura, V. G. Lifshits, A. A. Saranin, A. V. Zotov, and M. Katayama, *Surface Science: An Introduction*, Springer, 2003. 19

[87] A. Pimpenelli and J. Villain, *Physics of Crystal Growth*, Cambridge University Press, 1998. 19

[88] P. R. Willmott and J. R. Huber, Rev. Mod. Phys. **72** (2000), 315. 20

[89] `http://www.quantel.fr/`. 21

[90] J.S. Resh, K.D. Jamison, J. Strozier, A. Bensaoula and A. Ignatiev, Phys. Rev. B **40** (1989), 1179. 25

[91] J. Griesche, N. Hoffmann, M. Rabe and K. Jacobs, Progress in Crystal Growth and Characterization of Materials **37** (1998), 103. 25

[92] A. F. Dégardin and A. J. Kreisler, Crystal Growth in Thin Solid Films: Control of Epitaxy, Research Signpost, Trivandrum, India, 2002, pp. 1–41. 28, 29

[93] J. Kunert, M. Bäcker, M. Falter and D. Schroeder-Obst, Journal of Physics: Conference Series **97** (2008), 012148. 28, 29

[94] J. M. Huijbregtse, J. H. Rector and B. Dam, Physica C **351** (2001), 183. 29, 99

[95] P. B. Mozhaev, I. M. Kotelyanskii, V. A. Luzanov, J. E. Mozhaeva, T. Donchev, E. Mateev, T. Nurgaliev, I. K. Bdikin, B. Zh. Narymbetov, Physica C. 29

[96] R. Sum, H. P. Lang, and H.-J. Güntherodt, Physica C **242** (1995), 174. 29

[97] G. Koster, B. L. Kropman, G. J. H. M. Rijnders, D. H. A. Blank, and H. Rogalla, Mater. Sci Eng. B **56** (1998), 209. 29, 30

[98] M. Kawasaki, A. Ohtomo, T. Arakane, K. Takahashi, M. Yoshimoto and H. Koinuma, Appl. Surf. Sci. **107** (1996), 102. 30

[99] G. Koster, B. L. Kropman, G. J. H. M. Rijnders, D. H. A. Blank, and H. Rogalla, Appl. Phys. Lett. **73** (1998), 2920. 30

[100] M. Kareev,S. Prosandeev, J. Liu, C. Gan, A. Kareev, J. W. Freeland, Min Xiao and J. Chakhalian, Appl. Phys. Lett. **93** (2008), 061909. 30

[101] D. J. Werder, C. H. Chen, R. J. Cava and B. Batlogg, Phys. Rev. B **37** (1998), 2317. 33

[102] J. L. Tallon, C. Bernhard, H. Shaked, R. L. Hitterman, and J. D. Jorgensen, Phys. Rev. B **51** (1995), 12911. 34

[103] R. Liang, D. A. Bonn, and W. N. Hardy, Phys. Rev. B **73** (2006), 180505(R). 34

[104] H. Hertz, Ann. Phys. **17** (1887), 983. 37

[105] J. J. Thomson, Phil. Mag. **48** (1899), 547. 37

[106] P. Lenard, Wien. Ber. **108** (1899), 649. 37

[107] P. Lenard, Ann. Phys. **2** (1900), 359. 37

[108] P. Lenard, Ann. Phys. **8** (1902), 149. 37

[109] M. Planck, Ann. Phys. **4** (1901), 553. 37

[110] A. Einstein, Ann. Phys. **31** (1905), 132. 37

[111] G. F. Derbenwick, D. T. Pierce, and W. E. Spicer, Phys. Rev. **11** (1945), 67. 37

[112] C. Caroli , D. Lederer-Rosenblatt, B. Roulett, and D. Saint James, Phys. Rev. **8** (1973), 4552. 37

[113] P. J. Feibelman and D. E. Eastman, Phys. Rev. **10** (1974), 4932. 37

[114] G. Jezequel and I. Pollini, Phys. Rev. B **41** (1990), 1327. 37

[115] H. Y. Fan, Z. Phys. **68** (1945), 43. 38

[116] H. Mayer and H. Thomas, Z. Phys. **147** (1957), 419. 38

[117] H. Puff, Phys. Stat. Sol. **1** (1961), 636. 38

[118] C. N. Berglund and W. E. Spicer, Phys. Rev. **136** (1964), A1030. 38

[119] S. Hüfner, *Photoelectron spectroscopy: Principles and applications (third edition)*, Springer-Verlag, 2003. 38

[120] N. W. Ashcroft and N. D. Mermin, *Solid state physics*, Brooks Cole, 1976. 39

[121] M. P. Seah and W. A. Dench, Surf. Interf. Anal. **1** (1979), 2. 39, 87

[122] `http://www.psi.ch/sls/adress/adress`. 40

[123] M. Månsson, *Adatoms, quasiparticles & photons: The multifaceted world of photoelectron spectroscopy*, KTH Thesis, Stockholm, 2007. 41, 42, 43, 50

[124] T. Claesson, M. Månsson, A. Önsten, M. Shi, Y. Sassa, S. Pailhès, J. Chang, A. Bendounan, L. Patthey, J. Mesot, T. Muro, T. Matsushita, T. Kinoshita, T. Nakamura, N. Momono, M. Oda, M. Ido, and O. Tjernberg , Physic Review B **80** (2009), 094503. 43

[125] A. C. Thompson & D. Vaughan, *X-ray data booklet*, Lawrence Berkeley National laboratory, 2nd Edition, 2001. 44

[126] D. H. Tomboulian & D. E. Hartman , Phys. Rev. **102** (1956), 1423. 45, 46

[127] E. E. Koch, D. E. Eastman and Y. Farges, *Handbook on Synchrotron Radiation, Vol. 1A*, North-Holland Publishing Company, 1983. 45, 46

[128] D. T. Attwood, *Soft x-rays and extreme ultraviolet radiation: Principles and applications*, Cambridge University Press, 2007. 47

[129] SLS web site, `http://sls.web.psi.ch`. 48

[130] G. Beamson et al., Surf. Interf. Anal. **15** (1990), 541. 49

[131] N. Martensson et al., J. Electr. Spectr. Rel. Phen. **70** (1994), 117. 49, 50

[132] Gammadata web site, `http://vgscienta.com`. 50

[133] J. Chang, *Magnetic and Electronic Properties of The High-Temperature Superconductor* $La_{2-x}Sr_xCuO_4$, ETHZ Thesis, Zürich, 2008. 54

[134] J. C. Campuzano, M. R. Norman and M. Randeria, arXiv:cond-mat/0209476 V1, 2002. 55, 59

[135] D. W. Lynch and C. G. Olson, *Photoemission Studies of High-Temperature Superconductors*, Cambridge University Press, 1999. 55, 59, 62

[136] M. R Norman, H. Ding, M. Randeria, J. C. Campuzano, T. Yokoya, T. Takeuchi, T. Takahashi, T. Mochiku, K, Kadowaki, P. Guptasarma and D. G Hinks, Nature **392** (1998), 157. 56, 94

[137] M. Månsson, T. Claesson, U. O. Karlsson, O. Tjernberg, S. Pailhès, J. Chang, J. Mesot, M. Shi, L. Patthey, N. Momono, M. Oda, and M. Ido, Review Of Scientific Instruments **78** (2007), 076103. 58

[138] M. Shi, J. Chang, S. Pailhès, M. R. Norman, J. C. Campuzano, M. Månsson, T. Claesson, O. Tjernberg, A. Bendounan, L. Patthey, N. Momono, M. Oda, M. Ido, C. Mudry, and J. Mesot, Phys. Rev. Lett. **101** (2008), 047002. 58, 62

[139] J. Chang, Y. Sassa, S. Guerrero, M. Månsson, M. Shi, S. Pailhès, A. Bendounan, R. Mottl, T. Claesson, O. Tjernberg, L. Patthey, M. Ido, M. Oda, N. Momono, C. Mudry and J. Mesot, New Journal of Physics **10** (2008), 103016. 58, 59, 62, 63, 94

[140] J. Chang, S. Pailhés, M. Shi, M. Månsson, T. Claesson, O. Tjernberg, J. Voigt, V. Perez-Dieste, L. Patthey, N. Momono, M. Oda, M. Ido, A. Schnyder, C. Mudry and J. Mesot, Phys. Rev. B **75** (2007), 224508. 58, 61, 69

[141] E. Razzoli, Y. Sassa, G. Drachuck, M. Månsson, A. Keren, M. Shay, M. H. Berntsen, O. Tjernberg, M. Radovic, J. Chang, S. Pailhès, N. Momono, M. Oda, M. Ido, O. J. Lipscombe, S. M Hayden, L. Patthey, J. Mesot and M. Shi, New Journal of Physics **12** (2010), 125003. 58, 59

[142] A. Damascelli, Z. Hussain and Z. X. Shen, Rev. Mod. Phys. **75** (2003), 474. 59

[143] P. Aebi, J. Osterwalder, P. Schwaller, L. Schlapbach, M. Shimoda, T. Mochiku, and K. Kadowaki, Phys. Rev. Lett. **72** (1994), 2757. 59

[144] H. Ding, A.F. Bellman, J.C. Campuzano, M. Randeria, M.R. Norman, T. Yokoya, T. Takahashi, H. Katayama-Yoshida, T. Mochiku, K. Kadowaki, G. Jennings and G. P. Brivio, Phys. Rev. Lett. **76** (1996), 1533. 59

[145] J. Ma, P. Alméras, R. J. Kelley, H. Berger, G. Margaritondo, X. Y. Cai, Y. Feng and M. Onellion, Phys. Rev. B **51** (1995), 9271. 59

[146] S. Borisenko, M. S. Golden, S. Legner, T. Pichlr, C. Dürr, M. Knupfer, J. Fink, G. Yang, S. Abell and H. Berger, Phys. Rev. Lett. **84** (2000), 4453. 59

[147] P. V. Bogdanov, A. Lanzara, X. J Zhou, W. L. Yang, H. Eisaki, Z. Hussain and Z. X. Shen, Phys. Rev. Lett. **89** (2002), 167002. 59, 60

[148] M. Platé, J. D. F. Mottershead, I. S. Elfimov, D. C. Peets, R. Liang, D. A. Bonn, W. N. Hardy, S. Chiuzbaian, M. Falub, M. Shi, L. Patthey and A. Damascelli, Phys. Rev. Lett. **95** (2005), 077001. 59

[149] K. M. Shen, F. Ronning, D. H. Lu, F. Baumberger, N. J. C. Ingle, W. S. Lee, W. Meevasana, Y. Kohsaka, M. Azuma, M. Takano, H. Takagi, and Z.-X. Shen, Sciences **307** (2005), 901. 59, 60

[150] D. S. Marshall, D. S. Dessau, A. G. Loeser, C. H. Park, A. Y. Matsuura, J. Eckstein, I. Bozovic, P. Fournier, A. Kapitulnik, W. E. Spicer and Z. X. Shen, Phys. Rev. Lett. **76** (1996), 4841. 59, 94

[151] A. G. Loeser, Z. X. Shen, D. S. Dessau, D. S. Marshall, C. H. Park, P. Fournier and A. Kapitulnik, Sciences **273** (1996), 325. 59, 94

[152] S. Chakravarty, C. Nayak and S. Tewari, Phys. Rev. B **68** (2003), 100504. 59

[153] J. Meng, G. Liu, W. Zhang, L. Zhao, H. Liu, X. Jia, D. Mu, S. Liu, X. Dong, J. Zhang, W. Lu, G. Wang, Y. Zhou, Y. Zhu, X. Wang, Z. Xu, C. Chen and X. J. Zhou , Nature **462** (2009), 335. 59

[154] W. E. Picket, Rev. Mod. Phys. **61** (1989), 443. 59

[155] T. Senthil, Phys. Rev. B **78** (2008), 035103. 59

[156] P. A. Lee, Rep. Prog. Phys. **71** (2008), 012501. 59

[157] A. J. Millis and M. R. Norman, Phys. Rev. B **76** (2007), 220503. 59

[158] S. Chakravarty and H. Y. Kee, Proc. Natl Acad. Sci. **105** (2008), 8835. 59

[159] A. Lanzara, P. V. Bogdanov, X. J. Zhou, S. A. Kellar, D. L. Feng, E. D. Lu, T. Yoshida, H. Eisaki, A. Fujimori, K. Kishio, J.-I. Shimoyama, T. Noda, S. Uchida, Z. Hussain and Z.-X. Shen, Nature **412** (2001), 510. 60, 69, 75, 84

[160] P. V. Bogdanov, A. Lanzara, S. A. Kellar, X. J. Zhou, E. D. Lu, W. J. Zheng, G. Gu, J-I. Shimoyama, K. Kishio, H. Ikeda, R. Yoshizaki, Z. Hussain and Z-X. Shen, Phys. Rev. Lett. **85** (2000), 2581. 60

[161] X. J. Zhou, T. Yoshida, A. Lanzara, P. V. Bogdanov, S. A. Kellar, K. M. Shen, W. L. Yang, F. Ronning, T. Sasagawa, T. Kakeshita, T. Noda, H. Eisaki, S. Uchida, C. T. Lin, F. Zhou, J. W. Xiong, W. X. Ti, Z. X. Zhao, A. Fujimori, Z. Hussain and Z.-X. Shen, Nature **423** (2003), 398. 60, 61, 69

[162] J. Graf, G.-H. Gweon, K. McElroy, S. Y. Zhou, C. Jozwiak, E. Rotenberg, A. Bill, T. Sasagawa, H. Eisaki, S. Uchida, H. Takagi, D.-H. Lee, and A. Lanzara, Phys. Rev. Lett. **98** (2007), 067004. 61

[163] B. P. Xie, K. Yang, D. W. Shen, J. F. Zhao, H. W. Ou, J. Wei, S. Y. Gu, M. Arita, S. Qiao, H. Namatame, M. Taniguchi, N. Kaneko, H. Eisaki, Z. Q. Yang, and D. L. Feng, Phys. Rev. Lett. **98** (2007), 147001. 61

[164] Z.-X. Shen, D. S. Dessau, B. O. Wells, D. M. King, W. E. Spicer, A. J. Arko, D. Marshall, L. W. Lombardo, A. Kapitulnik, P. Dickinson, S. Doniach, J. DiCarlo, T. Loeser and C. H. Park, Phys. Rev. Lett. **70** (1993), 1553. 61, 62, 63

[165] H. Ding, M.R. Norman, J.C. Campuzano, M. Randeria, A.F. Bellman, T. Yokoya, T. Takahashi, T. Mochiku and K. Kadowaki, Phys. Rev. B **54** (1996), R9678. 62, 63, 86

[166] B. O. Wells, Z. X. Shen, D. S. Dessau, W. E. Spicer, D. B. Mitzi, L. Lombardo, A. Kapitulnik and A. J. Arko, Phys. Rev. B **46** (1992), 11830. 62

[167] M. R Norman, D. Pines and C. Kallin, Adv. Phys. **54** (2007), 715. 62, 94

[168] X. J. Zhou, P. Bogdanov, S. A. Kellar, T. Noda, H. Eisaki, S. Uchida, Z. Hussain, and Z.-X. Shen, Science **286** (1999), 268. 62

[169] X. J. Zhou, T. Yoshida, S. A. Kellar, P. V. Bogdanov, E. D. Lu, A. Lanzara, M. Nakamura, T. Noda, T. Kakeshita, H. Eisaki, and Z.-X. Shen, Phys. Rev. Lett. **86** (2001), 5578. 62

[170] T. Kondo, R. Khasanov, J. Karpinski, S. M. Kazakov, N. D. Zhigadlo, T. Ohta, H. M. Fretwell, A. D. Palczewski, J. D. Koll, J. Mesot, E. Rotenberg, H. Keller, A. Kaminski, Phys. Rev. Lett. **98** (2007), 157002. 65

[171] T. Kondo, R. Khasanov, Y. Sassa, A. Bendounan, S. Pailhès, J. Chang, J. Mesot, H. Keller, N. D. Zhigadlo, M. Shi, Z. Bukowski, J. Karpinski, A. Kaminski, Phys. Rev. B **80** (2009), 100505. 65

[172] T. Kondo, R. Khasanov, J. Karpinski, S. M. Kazakov, N. D. Zhigadlo, Z. Bukowski, M. Shi, A. Bendounan, Y. Sassa, J. Chang, S. Pailhés, J. Mesot, J. Schmalian, H. Keller, A. Kaminski, Phys. Rev. Lett. **105** (2010), 267003. 65

[173] C. Berthod, T. Giamarchi, S. Biermann, A. Georges, Phys. Rev. Lett. **97** (2006), 136401. 65, 66

[174] E. A. Yelland, J. Singleton, C. Mielke, N. Harrison, F. F. Balakirev, B. Dabrowski, J. R. Cooper, Phys. Rev. Lett. **100** (2008), 047003. 65

[175] M. Abrecht, D. Ariosa, D. Cloetta, D. Vobornik, G. Margaritondo and D. Pavuna, J. Phys. Chem. Solids **65** (2004), 1391. 66

[176] J. C. Campuzano, G. Jennings, M. Faiz, L. Beaulaigue, B. W. Veal, J. Z. Liu, A. P. Paulikas, K. Vandervoort, H. Claus, R. List, A. J. Arko and R. J. Bartlett, Phys. Rev. Lett. **64** (1990), 2308. 67

[177] D. H. Lu, D. L. Feng, N. P. Armitage, K. M. Shen, A. Damascelli, C. Kim, F. Ronning, Z. X. Shen, D. A. Bonn, R. Liang, W. N. Hardy, A.I. Rykov, S. Tajima, Phys. Rev. Lett. **86** (2001), 4370. 67, 68, 76

[178] R. Liu, B. W. Veal, A. P. Paulikas, J. W. and Downey, P. J. Kostić, S. Fleshler, U. Welp, C. G. Olson, X. Wu, A. J. Arko and J. J. Joyce, Phys. Rev. B **46** (1992), 11056. 67

[179] M. C. Schabel, C.-H. Park, A. Matsuura, Z.-X. Shen, D. A. Bonn, R. Liang, and W. N. Hardy, Phys. Rev. B **57** (1998), 6090. 67, 68

[180] M. C. Schabel, C.-H. Park, A. Matsuura, Z.-X. Shen, D. A. Bonn, R. Liang, and W. N. Hardy, Phys. Rev. B **57** (1998), 6107. 67

[181] J. D. Jorgensen, M. A. Beno, D. G. Hinks, L. Soderholm, K. J. Volin, R. L. Hitterman, J. D. Grace and I. K. Schuller, Phys. Rev. B **36** (1987), 3608. 67

[182] O. K. Andersen, A. I. Liechtenstein, O. Jepsen, and F. Paulsen, J. Phys. Chem. Solids **56** (1995), 1573. 67, 76, 79

[183] S. V. Borisenko, A. A. Kordyuk, V. Zabolotnyy, J. Geck, D. Inosov, A. Koitzsch, J. Fink, M. Knupfer, B. Büchner, V. Hinkov, C. T. Lin, B. Keimer, T. Wolf, S. G. Chiuzbăian, L. Patthey, R. Follath, Phys. Rev. Lett. **96** (2006), 117004. 68, 75, 76

[184] S. V. Borisenko, A. A. Kordyuk, T. K. Kim, A. Koitzsch, M. Knupfer, J. Fink, M. S. Golden, M. Eschrig, H. Berger and R. Follath, Phys. Rev. Lett. **90** (2003), 207001. 69

[185] A. A. Kordyuk, S. V. Borisenko, A. Koitzsch, J. Fink, M. Knupfer and H. Berger, Phys. Rev. B **71** (2005), 214513. 69, 75, 84

[186] A. A. Kordyuk, S. V. Borisenko, V. B. Zabolotnyy, J. Geck, M. Knupfer, J. Fink, B. Büchner, C. T. Lin, B. Keimer, H. Berger, A. V. Pan, S. Komiya and Y. Ando, Phys. Rev. Lett. **97** (2006), 017002. 69, 75

[187] P. D. Johnson, T. Valla, A. V. Fedorov, Z. Yusof, B. O. Wells, Q. Li, A. R. Moodenbaugh, G. D. Gu, N. Koshizuka, C. Kendziora, S. Jian, and D. G. Hinks, Phys. Rev. Lett. **87** (2001), 177007. 69

[188] V. B. Zabolotnyy, S. V. Borisenko, A. A. Kordyuk, J. Geck, D. S. Inosov, A. Koitzsch, J. Fink, M. Knupfer, B. Büchner, S.-L. Drechsler, H. Berger, A. Erb, M. Lambacher, L. Patthey, V. Hinkov, B. Keimer, Phys. Rev. B **76** (2007), 064519. 69, 70, 76

[189] H. L. Edwards, J. T. Markert, and A. L. de Lozanne, Phys. Rev. Lett. **69** (1992), 2967. 69

[190] D. J. Derro, E. W. Hudson, K. M. Lang, S. H. Pan, J. C. Davis, J. T. Markert and A. L. de Lozanne, Phys. Rev. Lett. **88** (2002), 097002. 69

[191] K. Nakayama, T. Sato, K. Terashima, H. Matsui, T. Takahashi, M. Kubota, K. Ono, T. Nishizaki, Y. Takahashi, and M. Kobayashi, Phys. Rev. B **75** (2007), 014513. 70, 76

[192] M. A. Hossain, J. D. F. Mottershead, D. Fournier, A. Bostwick, J. L. Mcchesney, E. Rotenberg, R. Liang, W. N. Hardy, G. A. Sawatzky, I. S. Elfimov, D. A. Bonn and A. Damascelli, Nature Phys. **4** (2008), 527. 70, 71, 76

[193] E. Bascones, T. M. Rice, A. O. Shorikov, A. V. Lukoyanov and V. I. Anisimov, Phys. Rev. B **71** (2005), 012505. 70, 77, 78, 79, 80, 82, 83, 84, 99, 101

[194] A. Carrington and E. A. Yelland, Phys. Rev. B **76** (2007), 140508(R). 70, 77, 78, 84, 99

[195] I. S. Elfimov, G. A. Sawatzky and A. Damascelli, Phys. Rev. B **77** (2008), 060504(R). 70, 77, 84, 99

[196] G Koster, A. Brinkman, H. Hilgenkamp, A. J. H. M. Rijnders and D. H. A. Blank, J. Phys. Condens. Matter **20** (2008), 264007. 71

[197] A. Ohtomo and H. Y. Hwang, Nature **427** (2004), 423. 71

[198] N. Nakagawa, H. .Y. Hwang and D. A. Muller, Nature Mat. **5** (2006), 204. 71

[199] T. Yoshida, X. J. Zhou, T. Sasagawa, W. L. Yang, P. V. Bogdanov, A. Lanzara, Z. Hussain, T. Mizokawa, A. Fujimori, H. Eisaki, Z.-X. Shen, T. Kakeshita, S. Uchida, Phys. Rev. Lett. **91** (2003), 027001. 75, 76, 84, 85

[200] F. Ronning, T. Sasagawa, Y. Kohsaka, K. M. Shen, A. Damascelli, C. Kim, T. Yoshida, N. P. Armitage, D. H. Lu, D. L. Feng, L.L. Miller, H. Takagi, Z.-X. Shen, Phys. Rev. B **67** (2003), 165101. 75, 76, 84

[201] J. M. Luttinger, Phys. Rev. **119** (1960), 1153. 75

[202] M. Oshikawa, Phys. Rev. Lett. **84** (2000), 3370. 75

[203] O. K. Andersen, A. I. Liechtenstein, O. Rodriguez, I. I. Mazin, O. Jepsen, V. P. Aantropov, O. Gunnarsson, and S. Gopalan, Physica C **147** (1991), 185. 76

[204] A. Kaminski, S. Rosenkranz, H. M. Fretwell, Z. Z. Li, H. Raffy, M. Randeria, M. R. Norman, and J. C. Campuzano, Phys. Rev. Lett. **90** (2003), 207003. 76

[205] D. Fournier, G. Levy, Y. Pennec, J. L. McChesney, A. Bostwick, E. Rotenberg, R. Liang, W. N. Hardy, D. A. Bonn, I. S. Elfimov and A. Damascelli, Nature Phys. **6** (2010), 905. 76, 80, 84, 94, 97, 100

[206] Z. Yamani, W. A. MacFarlane, B. W. Statt, D. Bonn, R. Liang, W. N. Hardy, Physica C **405** (2004), 227. 78

[207] T. Tohyama and S. Maekawa, Supercond. Sci. Technol. **13** (2000), 17. 83

[208] H. Yagi, T. Yoshida, A. Fujimori, K. Tanaka, N. Mannella, W. L. Yang, X. J. Zhou, D. H. Lu, Z.-X. Shen, Z. Hussain, M. Kubota, K. Ono, K. Segawa, Y. Ando, D. Iijima, M. Goto, K. M. Kojima, S. Uchida, arXiv:1002.0655v1, (2010). 83

[209] A. Bianconi, G. Bianconi, S. Caprara, D. Di Castro, H. Oyanagi, and N. L. Saini, J. Phys.: Condens. Matter **12** (2000), 10655. 83

[210] M. Hashimoto, T. Yoshida, H. Yagi, M. Takizawa, A. Fujimori, M. Kubota, K. Ono, K. Tanaka, D. H. Lu, Z.-X. Shen, S. Ono, Y. Ando, Phys. Rev. B **77** (2008), 094516. 83

[211] T. Tohyama and S. Maekawa, Phys. Rev. B **67** (2003), 092509. 83

[212] T. Yoshida, X. J. Zhou, K. Tanaka, W. L. Yang, Z. Hussain, Z.-X. Shen, A. Fujimori, S. Sahrakorpi, M. Lindroos, R. S. Markiewicz, A. Bansil, S. Komiya, Y. Ando, H. Eisaki, T. Kakeshita and S. Uchida, Phys. Rev. B **74** (2006), 224510. 83

[213] X.J Zhou, T. Yoshida, D.-H. Lee, W. L. Yang, V. Brouet, F. Zhou, W. X. Ti, J. W. Xiong, Z. X. Zhao, T. Sasagawa, T. Kakeshita, H. Eisaki, S. Uchida, A. Fujimori, Z. Hussain, Z.-X. Shen, Phys. Rev. Lett. **92** (2004), 187001. 85

[214] M. R. Norman, M. Randeria, H. Ding, J. C. Campuzano, Phys. Rev. B **52** (1995). 86

[215] M. Okawa, K. Ishizaka, H. Uchiyama, H. Tadatomo, T. Masui, S. Tajima, X.-Y. Wang, C.-T. Chen, S. Watanabe, A. Chainani, T. Saitoh, and A. Shin, Phys. Rev. B **79** (2009), 144528. 87

[216] C. C. Tsuei and J. R. Kirtley, Rev. Mod. Phys. **72** (2000), 969. 87

[217] J. E. Sonier, J. H. Brewer, R. F. Kiefl, R. I. Miller, G. D. Morris, C. E. Stronach, J. S. Gardner, S. R. Dunsiger, D. A. Bonn, W. N. Hardy, R. Liang, and R. H. Heffner, Science **292** (2001), 1692. 87

[218] J. Xia, E. Schemm, G. Deutscher, S. A. Kivelson, D. A. Bonn, W. N. Hardy, R. Liang, W. Siemons, G. Koster, M. M. Fejer, and A. Kapitulnik, Phys. Rev. Lett. **100** (2008), 127002. 87

[219] S. A. Kivelson, I. P. Bindloss, E. Fradkin, V. Oganesyan, J. M. Tranquada, A. Kapitulnik, and C. Howald, Rev. Mod. Phys. **75** (2003), 1201. 87

[220] C. M. Varma, Phys. Rev. B **55** (1997), 14554. 87

[221] M. Covington, M. Aprili, E. Paraoanu, L. H. Greene, F. Xu, J. Zhu and C. A. Mirkin, Phys. Rev. Lett. **79** (1997), 277. 87

[222] R. Khasanov, S. Strässle, D. Di Castro, T. Masui, S. Miyasaka, S. Tajima, A. Bussmann-Holder, H. Keller, Phys. Rev. Lett. **99** (2007), 237601. 87, 92, 107

[223] F. Gross, B. S. Chandrasekhar, D. Einzel, K. Andres, P. J. Hirschfeld, H. R. Ott, J. Beuers, Z. Fisk and J. L. Smith, Z. Phys. B **64** (1986), 175. 90

[224] R. Prozorov and R. W. Giannetta, Supercond. Sci. Technol. **19** (2006), R41. 90

[225] T.J. Jackson, T. M. Riseman, E. M. Forgan, H. Glückler, T. Prokscha, E. Morenzoni, M. Pleines, Ch. Niedermayer, G. Schatz, H. Luetkens, J. Litterst, Phys. Rev. Lett. **84** (2000), 4958. 92, 107

[226] V. J. Emery and S. A. Kivelson, Nature **374** (1995), 434. 94

[227] T. Kondo, Y. Hamaya, A. D. Palczewski, T. Takeuchi, J. S. Wen, Z. J. Xu, G. Gu, J. Schmalian, A. Kaminski, Nature Phys. **7** (2010), 21. 94

[228] J. L. Tallon and J. W. Loram, Physica C **349** (2001), 53. 94

[229] A. Kaminski, S. Rosenkranz, H. M. Fretwell, J. C. Campuzano, Z. Li, H. Raffy, W. G. Cullen, H. You, C. G. Olson, C. M. Varma and H. Höchst, Nature **416** (2002), 610. 94

[230] S. V. Borisenko, A. A. Kordyuk, A. Koitzsch, T. K. Kim, K. A. Nenkov, M. Knupfer, J. Fink, C. Grazioli, S. Turchini, and H. Berger, Phys. Rev. Lett. **92** (2004), 207001. 94

[231] A. Kanigel, U. Chatterjee, M. Randeria, M. R. Norman, G. Koren, K. Kadowaki, and J. C. Campuzano, Phys. Rev. Lett. **101** (2008), 137002. 94

[232] U. Chatterjee, M. Shi, D. Ai, J. Zhao, A. Kanigel, S. Rosenkranz, H. Raffy, Z. Z. Li, K. Kadowaki, D. G. Hinks, Z. J. Xu, J. S. Wen, G. Gu, C. T. Lin, H. Claus, M. R. Norman, M. Randeria and J. C. Campuzano, Nature Phys. **6** (2009), 99. 94

[233] K. Terashima, H. Matsui, T. Sato, T. Takahashi, M. Kofu, K. Hirota, Phys. Rev. Lett. **99** (2007), 017003. 94

[234] M. Månsson, Y. Sassa, B. M. Wojek, M. Radović, A. Suter, To be published (2011). 107

Acknowledgements

Naturally, this thesis is not a "one-woman-show", and there are many people that have contributed directly or indirectly to it. Even if I think that the best "thanks" are the one that you say face to face, I will give a try in writing it.

First, I would like to express my sincere gratitude to Joël Mesot for giving me the opportunity to do this PhD and for enthusiastic discussions of various kinds, physics related or not, and for simply being there whenever it was needed.

I thanks Philipp Aebi for accepting me as PhD student in Neuchâtel University.

I am grateful to Luc Patthey for supervising with always a positive attitude and for his trust when I was doing experiments on the SIS beamline.

Also I would like to thanks:

- Ming Shi for his help, advices and discussions on ARPES data analysis and for learning me how to use IGOR.
- Bertram Batlogg for his trust, enthusiasm and long discussions about the weird but nonetheless interesting Na_xCoO_2. I am looking forward to work in his group.
- Martin Månsson for...a lot of things. If I have to list how Martin helped me during these years, it would be too long. I can just say that I am really grateful for his support (in work and out of work) and never-ending encouragement, whenever my self-confidence was failing.
- Milan Radović for his help on the PLD machine, advices and explanations about film preparations. When talking about PLD, I should thanks Philip R. Willmott for letting Milan and I use his laboratory for preparing substrates and for his advices about the PLD technique. Christian Schlepütz, Christof Schneider and Stephan Pauli should not be forgotten for valuable discussions.
- Johan Chang for his help during beamtimes, discussions and advices.

- Elia Razzoli for the optimization of the IGOR macros which makes data analysis faster during beamtimes but also discussions about HTSC and about TV series... I wish him good luck for his PhD which I am sure will be a success.

- Xiaoyu Cui for his support at the beamline and funny comments such as "Never trust your eyes".

- Jakob Kanter for his patience when I was choosing the Na_xCoO_2 single crystals.

- Fritz Dubi, Christof Hess and Markus Kropf for their technical supports and keeping in shape all the instruments in the beamline.

- Ekaterina Pomjakushina for letting me use the gloves box when I needed to prepare my samples.

- Stéphane Pailhès for his advices. It was a real pleasure to work under his supervision during my Master thesis and to have him as collaborator during my PhD.

- Some of users of the SIS beamline with who I have had many interesting discussions and hope to keep as collaborators: Oscar Tjernberg, Adam Kaminski, Takeshi Kondo, Marco Grioni, Stéphane Pons, Tomasz Durakiewicz, Amit Kanigel, J.C. Campuzano, and many others.

- Michael R. Norman for his help on theoretical matters and very nice discussions.

- Of course, I should mentioned the people of SIS, COPHEE and ADRESS: Yaobo Huang, Hugo Dil, Fabien Meier, Bartosz Slomski, Thorsten Schmitt, Vladimir Strocov, Kejin Zhou, Justina Schlappa and Claude Monney.

- The LNS group: even if I did not perform any neutrons experiments, all the LNS members were always ready to explain me their technique and were always very nice to me.

- The ex- and actual PhD students and postdocs with who I spent good moments: Krunoslav Prša, Nikolay Tsyrulin, Gelu Rotaru, Mohamed Zayed, Nikola Egetenmeyer, Julia Rasch, Verena Staedele, Gwendolyne Pascua, Jorge Lobo-Checa, Sorin Chiuzbaian, Virginia Perez-Dieste and many others...

- Bastian M. Wojek for who he is. During the wrtting of our respective thesis, we supported each other and also complain a lot. I really enjoyed our coffee break discussions (god knows how long our coffee breaks were sometimes...) and villigen pizza. I can just say that I am happy to have him as a friend and hope that we will keep in touch wherever you are.

- Cécile Garcia pour sa bonne humeur naturelle et son joli accent toulousain qui vous remonte toujours le moral.
- Daniela Jahns for her good mood and our lunches that I really appreciate.
- Ursula Schmid for taking the time to listen to me during my "black"period.

Last but not least... Merci, Maman, Papa, Adil, Kitana et Yoda pour votre soutien!

MERCI A TOUS!

Publications

Revealing the Ortho-II Band Folding in $YBa_2Cu_3O_{7-\delta}$
Y. Sassa, M. Radović, M. Månsson, E. Razzoli, X. Cui, S. Pailhès, S. Guerrero, M. Shi, P. R. Willmott, F. Miletto Granozio, J. Mesot, M. R. Norman, and L. Patthey
Phys. Rev. B **83**, 140511 (2011)

Insensitivity of the superconducting gap to variation in T_c in Zn-substituted Bi2212
Y. Lubashevsky, A. Garg, Y. Sassa, M. Shi, and A. Kanigel
Phys. Rev. Lett. **106**, 047002 (2011)

The Fermi surface and band folding in $La_{2-x}Sr_xCuO_4$, probed by angle-resolved photoemission
E. Razzoli, Y. Sassa, G. Drachuck, M. Månsson, A. Keren, M. Shay, M. H. Berntsen, O. Tjernberg, M. Radović, J. Chang, S. Pailhès, N. Momono, M. Oda, M. Ido, O. J. Lipscombe, S. M. Hayden, L. Patthey, J. Mesot, and M. Shi
New J. Phys. **12**, 125003 (2010)

Anomalies in the Fermi Surface and Band Dispersion of Quasi-One-Dimensional CuO Chains in the High-Temperature Superconductor $YBa_2Cu_4O_8$
T. Kondo, R. Khasanov, J. Karpinski, S. M. Kazakov, N. D. Zhigadlo, Z. Bukowski, M. Shi, A. Bendounan, Y. Sassa, J. Chang, S. Pailhès, J. Mesot, J. Schmalian, H. Keller, and A. Kaminski
Phys. Rev. Lett. **105**, 267003 (2010)

Anomalous asymmetry in the Fermi surface of the high-temperature superconductor $YBa_2Cu_4O_8$ revealed by angle-resolved photoemission spectroscopy
T. Kondo, R. Khasanov, Y. Sassa, A. Bendounan, S. Pailhès, J. Chang, J. Mesot, H. Keller, N. D. Zhigadlo, M. Shi, Z. Bukowski, J. Karpinski, and A. Kaminski
Phys. Rev. B **80**, 100505(R) (2009)

Electronic structure of $La_{1.48}Nd_{0.4}Sr_{0.12}CuO_4$ probed by high- and low-energy angle-resolved photoelectron spectroscopy
T. Claesson, M. Månsson, A. Önsten, M. Shi, Y. Sassa, S. Pailhès, J. Chang, A. Bendounan, L. Patthey, J. Mesot, T. Muro, T. Matsushita, T. Kinoshita, T. Nakamura, N. Momono, M. Oda, M. Ido, and O. Tjernberg
Phys. Rev. B **80**, 094503 (2009)

Spectroscopic evidence for preformed Cooper pairs in the pseudogap phase of cuprates
M. Shi, A. Bendounan, E. Razzoli, S. Rosenkranz, M. R. Norman, J. C. Campuzano, J. Chang, M. Månsson, Y. Sassa, T. Claesson, O. Tjernberg, L. Patthey, N. Momono, M. Oda, M. Ido, S. Guerrero, C. Mudry, and J. Mesot
Europhys. Lett. **88**, 27008 (2009)

Electronic structure near the 1/8-anomaly in La-based cuprates
J. Chang, Y. Sassa, S. Guerrero, M. Månsson, M. Shi, S. Pailhès, A. Bendounan, R. Mottl, T. Claesson, O. Tjernberg, L. Patthey, M. Ido, M. Oda, N. Momono, C. Mudry, and J. Mesot
New J. Phys. **10**, 103016 (2008)

Anisotropic quasiparticle scattering rates in slightly underdoped to optimally doped high-temperature $La_{2-x}Sr_xCuO_4$ superconductors
J. Chang, M. Shi, S. Pailhès, M. Månsson, T. Claesson, O. Tjernberg, A. Bendounan, Y. Sassa, L. Patthey, N. Momono, M. Oda, M. Ido, S. Guerrero, C. Mudry, and J. Mesot
Phys. Rev. B **78**, 205103 (2008)

Origins of large critical temperature variations in single-layer cuprates
A. D. Palczewski, T. Kondo, R. Khasanov, N. N. Kolesnikov, A. V. Timonina, E. Rotenberg, T. Ohta, A. Bendounan, Y. Sassa, A. Fedorov, S. Pailhès, A. F. Santander-Syro, J. Chang, M. Shi, J. Mesot, H. M. Fretwell, and A. Kaminski
Phys. Rev. B **78**, 054523 (2008)